Solid State Nuclear Magnetic Resonance Investigations of Advanced Energy Materials

by

George D Bennett

A dissertation submitted to the Graduate Faculty in Physics in partial fulfillment of the requirements for the degree of Doctor of Philosophy,
The City University of New York

2009

This manuscript has been read and accepted for the
Graduate Faculty in Physics in satisfaction of the
dissertation requirement for the degree of Doctor of Philosophy.

Steve G Greenbaum

Date — Chair of Examining Committee

Steve G Greenbaum

Date — Executive Officer

Sultan Catto

Ying-Chih Chen

Gregory S. Boutis

Glenn G. Amatucci

Supervisory Committee

THE CITY UNIVERSITY OF NEW YORK

Abstract

Solid State Nuclear Magnetic Resonance Investigations of Advanced Energy Materials

by

George D Bennett

Advisor: Professor Steve G Greenbaum

In order to better understand the physical electrochemical changes that take place in lithium ion batteries and asymmetric hybrid supercapacitors solid state nuclear magnetic resonance (NMR) spectroscopy has been useful to probe and identify changes on the atomic and molecular level. NMR is used to characterize the local environment and investigate the dynamical properties of materials used in electrochemical storage devices (ESD). NMR investigations was used to better understand the chemical composition of the solid electrolyte interphase which form on the negative and positive electrodes of lithium batteries as well as identify the breakdown products that occur in the operation of the asymmetric hybrid supercapacitors. The use of nano-structured particles in the development of new materials causes changes in the electrical, structural and other material properties. NMR was used to investigate the affects of fluorinated and non fluorinated single wall nanotubes (SWNT). In this thesis three experiments were performed using solid state NMR samples to better characterize them.

The electrochemical reactions of a lithium ion battery determine its operational profile. Numerous means have been employed to enhance battery cycle life and operating temperature range. One primary means is the choice and makeup of the electrolyte. This study focuses on the

characteristics of the solid electrolyte interphase (SEI) that is formed on the electrodes surface during the charge discharge cycle. The electrolyte in this study was altered with several additives in order to determine the influence of the additives on SEI formation as well as the intercalation and de-intercalation of lithium ions in the electrodes. ^{7}Li NMR studies where used to characterize the SEI and its composition.

Solid state NMR studies of the carbon enriched acetonitrile electrolyte in a nonaqueous asymmetric hybrid supercapacitor were performed. Magic angle spinning (MAS) coupled with cross polarization NMR techniques were used to determine what effects 200 ppm of intentionally added water would have on the decomposition of the acetonitrile. The resultant NMR spectra yielded several prominent peaks which were assigned to acetamide, glycolonitrile, formaldehyde and other lithium carbon derivatives. The aforementioned decomposition products are a believed to be a result of the acetonitrile being hydrolyzed as well as its interaction with the lithium salt. The decomposition products are deposited on electrode surface leading to operation changes in the life of the supercapacitors. The information gained from the NMR studies may be beneficial understanding the supercapacitor operation and aid in future design.

Carbon nanotubes are used to enhance structural stability and performance. In this experiment NMR is used to determine if the addition of nanotubes to two types of polymer matrix changes the structural stiffness and motional dynamics. The polymers studied by direct ^{1}H NMR observations are Polybutadiene (PB) and Polyisobutylene (PIB). PB and PIB with single walled carbon nanotubes (SWNT) as well as functionalized with fluorine (F) produce significantly stronger composites as compared to composites without SWNT.

Dedication

This work and effort is dedicated to my parents George Bennett Sr. and Mansie May Bennett. They through love, thoughtfulness, selflessness, kindness and endless dedication to their seven children provided an environment where I could survive, grow and develop. They at every opportunity, without regard, put my happiness and chance for betterment before their own. In addition I would like to give my profound thanks to Professor Frederick Rudolf Wills who at every turn in my young intellectual and academic life gave me a chance and an opportunity to view and understand the world and reality as it was meant to be. Last but not least, this is for my children Christopher, Everton, Mansie May, and Shani who are all bright, inquisitive, engaging, and loving. They have been a constant source of inspiration and endless ocean of love. To all the persons named above I offer my sincerest and most heartfelt gratitude.

Acknowledgements

I would like to thank Professor Steve G. Greenbaum who as my mentor was patient and essential in the completion of my work. I must thank Allida Gupton, former Physics Graduate Center program officer, whose tireless effort, compassion and communication over the years facilitated my return and progression through the physics PhD program. There are four persons at Hunter College and City University of New York whose support, encouragement and endless help made attaining my PhD that much more possible. They are Professor Glendon D. McLachlan. Dr. Phil Stallworth, Dr. Tibab NcNish and Dr. Amish Khalfan. The aforementioned persons gave me valuable insight, explanations and support in the understanding and mastery of NMR.

To my wonderful and always encouraging and supportive six (older) brothers and sisters who never failed to make me feel special I give an never ending thanks. Specifically to my sister Carmen L Bennett MD whose academic and intellectual light lit the path for us all. To my big brother Errol, who should have his name next to mine on all my diplomas, I am forever grateful for your nurturing, guidance, love and protection throughout my life. I want to specially thank Etwilla, Leanora Bennett JD, Audrey and Earliss who made hundreds of phone calls, trips, inspirational and supportive suggestions, as well as their endless glowing love for me without which I would not be who I am.

To my two best friends, Anthony Eldridge, and Beresford “Barry” Smith, whose unrestrained support and unquantifiable friendship for over twenty years have helped me through intellectual cross fertilization to mature, prosper and survive a variety of circumstance with grace and dignity. Additionally I would like to thank Julian Lockhart for his kindness and many hours of assistance which immensely benefitted me and my family

And finally to my friend, life partner and wife, Karen R Stephenson MD I want you to know it has and always will be us, we, and you and I forever with love.

Outline

Table of Contents

List of Tables and Figures

Chapter 4

Chapter 5

Chapter 1 – A General Introduction

1.1 Introduction

The demand for clean, renewable sources of energy has become an issue of paramount importance. The escalating cost of fossil fuels as well as their negative impact on the environment has made the search for environmentally friendly alternatives all the more critical. Electrical energy that is generated by solar, wind, bio-mass, geo-thermal and other renewable forms offer many advantages over fossil fuel based sources. In order to maximize usage of these renewable sources more efficient forms of electrical energy storage devices (ESD) are needed [1], [2], [3]. ESDs are electrochemical devices, and the two primary types are batteries and capacitors. The difference in these two kinds is that batteries store energy in chemical reactants capable of generating charge whereas the electrochemical capacitor stores energy directly as charge [1]. Even though the ESDs in today's market show a great deal of promise, they are limited. ESDs must possess high energy and high power densities as well as an improved charge/discharge profile if they are to continue to be viable options for portable devices and hybrid electric vehicles.

To improve the characteristics of ESDs, there must be further advancement in the scientific understanding underlying the physics and chemistry of these devices at the atomic and molecular levels. Such understanding can shed light into processes occurring during extreme temperature variation, the causes for reduced performance over time, and the materials required for better ESD design and operation. Limitations in the performance of ESDs can often be attributed to a breakdown at the interface of the electrolyte and the electrode. Much research has been centered on the choice of electrode material and its performance over the cycle life of the

ESD as well as the solvents used in the electrolyte [4], [5], [6]. The choice of new materials is highly dependent upon how well they increase energy capacity and control volume and structural changes under charge and discharge cycling. Nanostructured materials in ESDs have shown great potential in allowing for a high energy capacity and high power density. Unfortunately, nanoscale science and research in reference to ESD development is not yet well understood [1], [7], [8]. One type of ESD that has emerged as the primary choice for rechargeable batteries is the lithium ion (Li-Ion) cell. Capacitors, the other type of ESDs, have been evolving. They have moved from simple dielectric devices to electrochemical double layer cells and presently to asymmetric hybrid supercapacitors. These two devices will be further discussed in this document.

1.2 Lithium-Ion Battery

Lithium-Ion (Li-ion) batteries have become an essential part of today's emerging technology. Without a sufficient source of portable power many of today's technologies would not be as readily embraced by the general public [1], [4], [9]. Electronic devices such as laptops, media players, calculators and cellular telephones now function primarily on lithium ion batteries. These types of batteries have an advantage over nickel cadmium (Ni-Cd) batteries because they do not suffer from the same charging memory effects. Li-Ion batteries do not need to be fully discharged before they are recharged, therefore a higher energy density and a better environmental toxicity profile can be achieved. In addition, Li-Ion batteries are slow to self-discharge. The self-discharge rate is approximately five percent per month and in contrast it is twenty percent for Ni-Cd and thirty percent for nickel hydride batteries.

Li-Ion batteries are made with a liquid electrolyte between the anode and the cathode. The Li-Ions flow from the anode to the cathode via the liquid lithium salt electrolyte. This type of design led to limitations in physical design, leakage and volatility concerns. A solid electrolyte may eliminate some of these issues. There is an acute need for a solid electrolyte that allows adequate ion diffusion while preventing potential short circuit effects. The advancement of battery and fuel cell technology depends on the creation of new materials. These new materials need to allow for the better ion mobility, transport and greater mechanical stability. The aforementioned properties should be effective over a wide range of operational temperatures as to be useful in a wide range of applications. These new solid electrolyte materials will allow for greater charge capacity for a smaller total volume and more flexible battery design [9].

Battery development is contingent on engineering and selecting the best materials for the anode, cathode, and the separator electrolyte. A lithium transition metal oxide is generally chosen for the cathode and a graphitic carbon material for the anode. The cathode and the anode should allow for good ion and electron exchange, good chemical and mechanical stability during battery operation. Characterization for these materials is performed by using Nuclear Magnetic Resonance (NMR) and the various techniques associated with this investigative methodology.

NMR analysis allows for structure and dynamic characterization of material properties. This form of spectroscopy aids the investigator in determining ion mobility, chemical structure, and reaction dynamics. In addition NMR spectroscopy enables one to examine individual ions within the context of their chemical environment. This ability to isolate by ion gives more specific information than electrical conductivity and X- ray diffraction. The type of NMR spectroscopy used on polymer electrolytes and various membranes for Li-Ion batteries is solid state NMR. There are several pulse sequence techniques that probe the local environment of the

nucleus. These testing formats will reveal information, and give initial characterization that aid in the defining of a spectrum and its time dependence.

1.3 Li-Ion Battery Operation

There are a wide variety of batteries and the basis of their operation is by reduction and oxidation reactions. The batteries consist of a cathode, an anode, and a medium for the reduction/oxidation to take place. The Silver Zinc cell, Carbon Zinc, Alkaline, Zinc Air Button cell, Lead Acid, Edison, NaCd, NiMH, and Lithium Ion are all batteries that employ various means to execute the reduction/oxidation scheme. The aforementioned batteries fall into two important categories. They are rechargeable and non-rechargeable batteries. Other important criteria to compare battery and battery types are efficiency and by specific energy. The specific energy of a battery format gives the storage capacity as a function of its mass. Lithium-Ion has one of the highest specific energy profiles of any battery. Below in figure 1.1 we can see the anatomy of a lithium based battery.

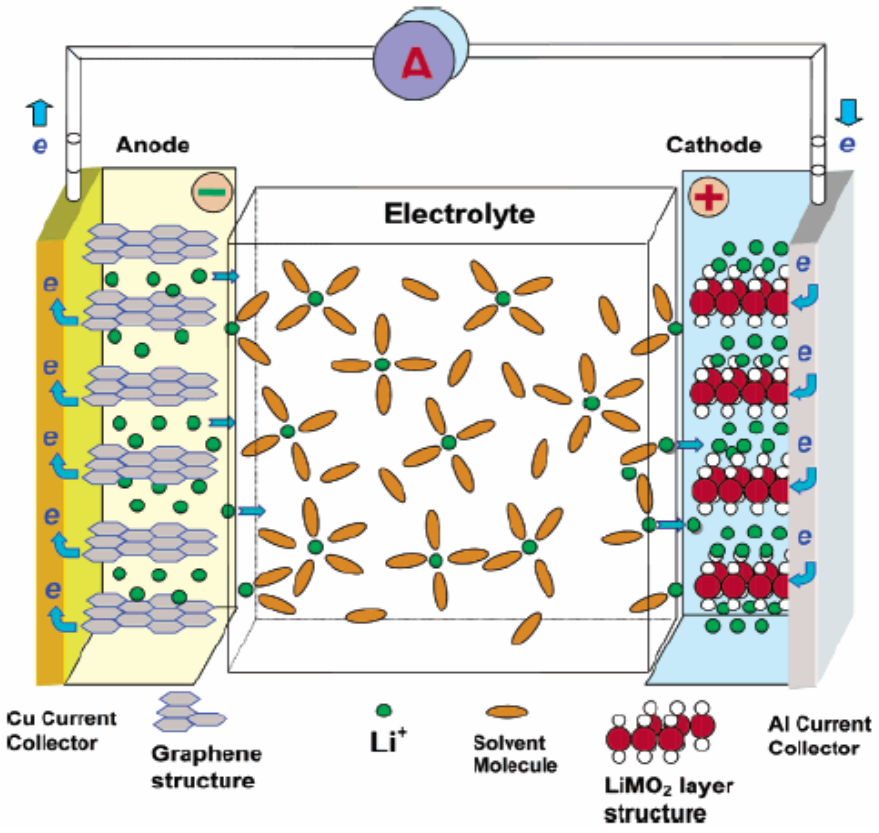

Figure 1.1 A lithium-ion based battery with anode, cathode, electrolyte and the current collectors [1].

Figure 1.1 is an illustration of the charge and discharge cycle of a Li-Ion battery. The cathode is a lithium transition metal oxide. In the above illustrative case the transition metal is manganese. It could be cobalt, another transition metal or combination of transitional metals. The anode is a graphite-based material, which can intercalate or release lithium. When discharge begins the lithiated carbon releases a Li^+ ion and a free electron. The electrolyte, which should readily facilitate ion transport, contains a lithium salt that is dissolved in an organic solvent [1],[17]. The Li^+ ion, which moves towards the electrolyte, replaces another Li^+ ion from the electrolyte, which moves towards the cathode. At the cathode/electrolyte interface, Li^+ ions then become intercalated into the cathode and the associated electron is used by the external device. When charging takes place, the lithium metal oxide is delithiated and the reverse process ensues.

The size of the lithium ion facilitates the charging and discharging of the battery because it can move easily within the cathode, anode, and polymer electrolyte. In addition to its size, lithium is chosen because it is light and has a very high electrochemical potential. The primary purpose of choosing materials for the cathode and anode is to maximize cell voltage. The transition metal chosen should also have a large capacity for oxidation. Cathode material should facilitate insertion and depletion of lithium ions in large quantity. This process should be reversible and should lead to minimal structural changes in the cathode. Another feature of cathode material design is that the cathode should be chemically stable and not react with the selected electrolyte over the entire voltage range.

1.4 Supercapacitors

Supercapacitors are electrochemical devices that have high surface area as compared to conventional capacitors, and the charged electrodes are separated by a thin electrolytic dielectric to enhance capacitance. The separation of charge at the interface is measured on the order of a fraction of a nanometer as opposed to micrometers, which is the case for most polymer film capacitors [10]. The energy in the supercapacitor is stored as static charge at the electrode-electrolyte interface as opposed to a battery where the energy is due to an electro-chemical process. Electrochemical double layer capacitors (EDLC) (supercapacitors) can be described as having a double-layer construction consisting of porous carbon-based electrodes with an electrolyte separator [11], [12], [13]. A more detailed discussion will be given in chapter 7. Attempts to increase the energy and power density have led to a new category called hybrid supercapacitors. Hybrid supercapacitors are identified by their electrode configuration. Hybrids are listed as composite, asymmetric and battery types. A composite hybrid has carbon based

electrodes with a conducting polymer. The asymmetric hybrid has an activated carbon negative electrode with a conducting polymer positive electrode. The battery type hybrid uses a porous carbon electrode with a high density battery electrode. Researchers are now experimenting with a variety of materials, including carbon nanotubes, for electrodes because they may improve ion transport and capacity [14], [15],[16]. The non-aqueous organic electrolytes usually use acetonitrile and allow a nominal voltage of up to

3 V [1].

[1] Annual Energy Review 2007 "www.eia.doe.gov/aer/pdf/aer.pdf"

[2] Coalition for Affordable and Reliable Energy, Energy and America's Economy, "www.careerenergy.com/energy/energy-americas-economy.asp," 2003.

[3] Status of Electrical Energy Storage Systems "www.berr.gov.uk/files/file15189.pdf," 2004.

[4] M. Wakihara, 0. Yamamoto, *Lithium Ion Batteries Fundamentals and Performance*, Wiley-VCH, 1998

[5] P. Poizot, S. Laruelle, S. Grugeon, L. Dupont, and J. M. Tarascon, *Nature*, 407, 2000

[6] J. M. Tarascon and M. Armand, *Nature*, 414, 2001

[7] C.Wanga, Z. X. Guob, S. Fua, W. Wub, and D. Zhub, *Progress in Polymer Science*, 29 2004

[8] M. L. Shofner, V. N. Khabashesku, and E.V. Barrera, *Chemical Material*, 18, 2006

[9] I. Hadjipaschalis, A. Poullikkas and V. Efthimiou, *Renewable and Sustainable Energy*

Reviews, 2008

[10] M. S. Halper and J. C. Ellenbogen, *Supercapacitors: A Brief Overview*, Mitre, 2006

[11] E. Frackowiak, and F. Beguin , *Carbon*, 39(6), 2001

[12] J. Gamby, P. L. Taberna, et al., *Journal of Power Sources*, 101(1), 2001

[13] D.Y. Qu, and H. Shi , *Journal of Power Sources*, 74(1), 1998

[14] K.H. An, W. S. Kim, et al., *Advanced Materials*, 13(7), 2001

[15] K.H An, W. S. Kim, et al, *Advanced Functional Materials*, 11(5), 2001

[16] C.S. Du, J. Yeh, et al., *Nanotechnology*, 16 (4), 2005

[17] P.V. Wright, *Materials Research Society*, Bulletin, (8), 2002

Chapter 2 – Perspectives of NMR

2.1 Quantum Mechanical View

Nuclear Magnetic Resonance, NMR, is a type of spectroscopy that uses electromagnetic radiation to drive transition between energy levels of nuclear spins. The type of radiation that is used is in the radio frequency range.

Modern NMR relies on a quantum mechanical description of the relationship between the nuclear spin and the magnetic field [1], [2], [3]. As previously stated, NMR exploits the intrinsic spin of the nucleus. The spin of the nucleus (or spin of the nucleons) gives rise to the magnetic moment, μ. If the total spin of the protons and neutrons is not zero, the overall spin of the nucleus generates a magnetic dipole moment along the spin axis. The intrinsic magnitude of this dipole is a fundamental nuclear property. The quantum mechanical description of the magnetic dipole moment is given by the equation

$$\vec{\mu} = \gamma \vec{I} \tag{2.1}$$

where I is the spin angular momentum and γ is the gyromagnetic ratio. The ratio is normally described in terms the mass of the proton and its charge, e, (neutrons are included). A simple form of the expression is given by

$$\gamma = \frac{e}{2m} g \tag{2.2}$$

where g is called the nuclear g-factor and is specific to each atomic nucleus. The nuclear gyromagnetic ratio is extremely important in in that NMR spectroscopy relies on the precession

of nuclear spin in a magnetic field. The rate of precession is called the Larmor frequency, ω_0. This rate is the product of the gyromagnetic ratio and the magnetic field strength, $\omega_0 = \gamma B_0$. Angular momentum *I* is quantized along the *z* direction. The range of its quantized component is governed by the magnetic quantum number *m* which denotes orientation. The values of *m* range from *–I, -I+1, ...,...,I-1, I* and *I* is the spin quantum number. The relationship between *m* and the quantized *I* component along z is given by

$$I_z = m\hbar \tag{2.3}$$

In systems with $I = 1/2$ the range of m_I is from $-1/2$ to $+1/2$ and for spins of $I=1$ the range of *m* is three values of *-1, 0, 1*[4]. Below, in figure 2.1, is a vector representation of spin systems of $I= 1/2$ and $I= 1$.

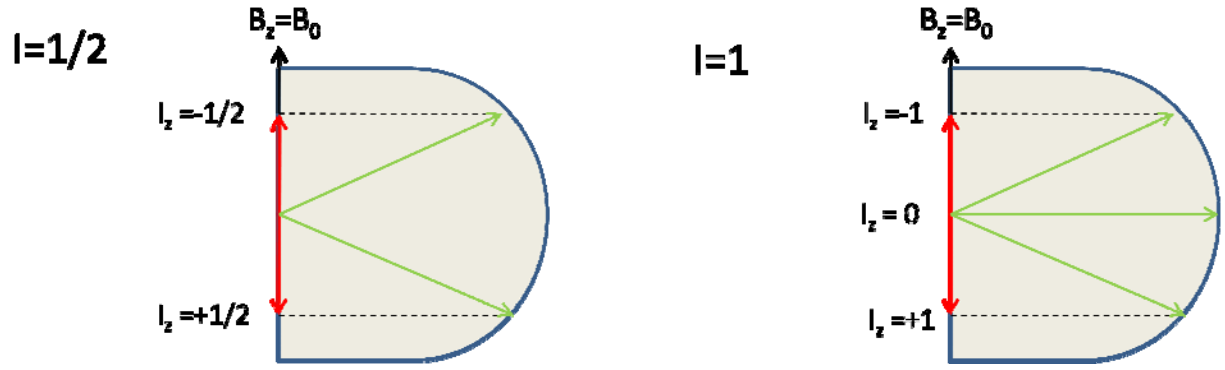

Figure 2.1. Quantized angular momentum of spin 1/2 with m_I ranging from -1/2 to 1/2 and for spin 1 with m_I ranges from -1, 0, to1.

The energy and the orientation of the nuclear spin can be changed by the absorption of a quantum of electromagnetic radiation. The associated Zeemna energy is generally given by the equation

$$E = -\vec{\mu} \cdot \vec{B} \tag{2.4}$$

where E is the energy. The above equation illustrates that the vector dot product depends on orientation. When the sample of nuclei is immersed in an external magnetic field a distribution of spins occurs based on their population orientation. The associated energy difference for the two states is given by the Zeeman relation

$$\Delta E = \hbar\omega \tag{2.5}$$

where $\hbar\omega$ is due to the difference from the α to the β state and B_z is equal to B_0. When the spin is aligned with the magnetic field the system is in the low energy state and when they are antiparallel to one another, the system is in the higher energy state [5]. Figures 2.2 and 2.3 show the parallel and anti-parallel conditions as well as the energy separation due to an external magnetic.

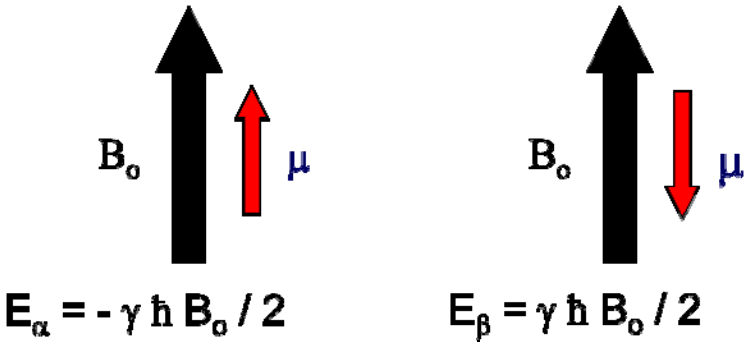

Figure 2.2 Magnetic dipole moments and the associated energy that are aligned with the external magnetic field and anti-parallel to the B_0 field with a spin 1/2 [5].

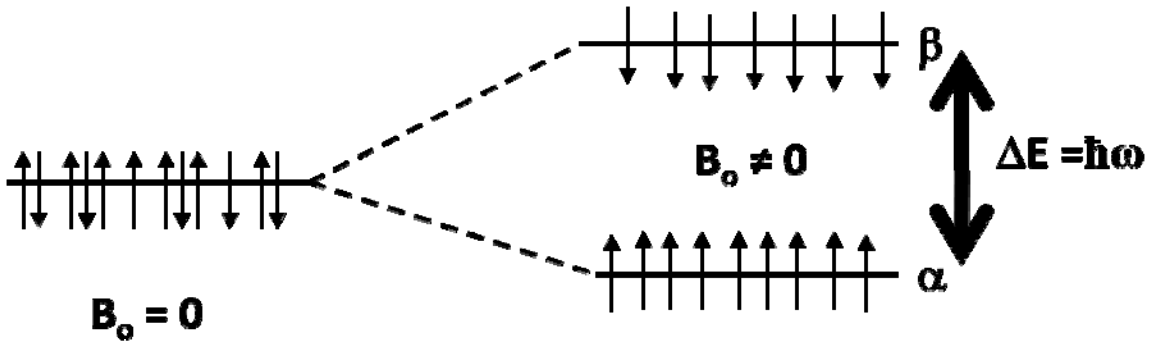

Figure 2.3 Energy level diagram of two spin states.

As seen in the figure 2.3, the two energy states are not equally populated. At thermodynamic equilibrium this population can be described by the Boltzmann distribution. The ratio of distributed spin states can be expressed as

$$\frac{N_\alpha}{N_\beta} = e^{\frac{\Delta E}{kT}} \tag{2.6}$$

where *N* is the number of spins in either the up state, α, or down state, β. The above analysis was done for a single nuclear spin *I=1/2* but can be generally extended to include systems containing large quantities of moments. The relationship between the individual spin and bulk spins is given by the equation

$$\vec{M} = \sum_i \vec{\mu}_i \tag{2.7}$$

where $\vec{M}$ is the bulk magnetization [6], [7],[8], [9].

The strength of this magnetization M_0 ($\vec{M} = M_0\hat{k}$) is determined by the very small size of the magnetic moments of the nuclei in question as well as by the net difference between the

number of nuclear spins aligned with and against B_0. The fractional ratio of population difference is known as the polarization, P. When the spins are at thermal equilibrium with their surroundings the population difference, again, is described by the Boltzmann distribution and it gives the polarization as [10]

$$P = \frac{N_\beta - N_\alpha}{N_\beta + N_\alpha} = tanh\left(\frac{\Delta E}{k_B T}\right) = tanh\left(\frac{\gamma \hbar B_0}{k_B T}\right) \qquad (2.8)$$

[1] C.P. Slichter, *Principles of Magnetic Resonance* 3ed. Springer-Verlag 1990

[2] M. Levitt, *Spin Dynamics: Basics of Nuclear Magnetic Resonance*, John Wiley & Sons, 2001

[3] D. J. Griffiths, *Introduction to Quantum Mechanics* 2ed. Benjamin Cummings, 2004

[4] O. Zerbe , NMR Spectroscopy Lecture Course, "http://www.oci.uzh.ch/group.pages/zerbe/" 2005

[5] G. Moyna, *Background Concepts*

"http://tonga.usip.edu/gmoyna/NMR_lectures/NMR_lectures.html"

[6] C. Kittel, *Introduction to Solid State Physics* 8ed., John Wiley & Sons, 2004

[7] J.W. Emsley, J. Feeney, *Progress in Nuclear Magnetic Resonance Spectroscopy* 50 (2007) 179.

[8] Eds. L. D. Field, S. Sternhell, *Analytical NMR*, 1ed., John Wiley & Sons, New York, 1989.

[9] U. Oehler, "http://www.chembio.uoguelph.ca/DrIguana/NMR/TOC.HTM", 2007

[10] Magnetic Resonance, "http://physchem.ox.ac.uk/~hill/tutorials/index.html" Oxford University, 2008

.

Chapter 3 - Nuclear Magnetic Resonace Interactions

3.1 Basic NMR Hamiltonian

There are several interactions that take place in NMR. They can be divided into two basic types. The two types are external interactions and internal interactions. A partial list of theses interactions is provided in Table 3.1. The external interactions are, as previously implied, that of the external magnetic field B_0 and B_1 the rf-pulse. They are external parameters that affect the target nucleus being investigated. The internal interactions contain all the fundamental information characterizing the nuclear spin system in the solid state. Some of the more important internal processes that affect solid state NMR results are the chemical shift, dipole-dipole interactions, and quadrupolar interactions. These interactions change or perturb the system thus causing the point of resonance to change. We can formulate the problem by using the Hamiltonian to express the total energy of the system [1], [2]. The energy E is related to the Hamiltonian operator by the following equation:

$$\hat{H}\psi = E\psi \tag{3.1}$$

where $\hat{H}$ is the Hamiltonian operator and E is the eigenvalue and ψ describes the wave function associated with the system. In solid state NMR the above operator can be broken into two parts, the external and internal components. Thus $\hat{H}$ is equivalent to $\hat{H}_{ext} + \hat{H}_{int}$ where

$$\hat{H}_{ext}(t) = \hat{H}_Z + \hat{H}_{rf}(t) \quad (3.2)$$

and

$$\hat{H}_{int} = \hat{H}_{cs} + \hat{H}_d + \hat{H}_Q \quad (3.3)$$

The first Hamiltonian operator, $\hat{H}_Z$, is as previously introduced the Zeeman interaction effect [2]. Thus the Zeeman Hamiltonian is

$$\hat{H} = -\hbar\gamma B_0 \hat{I}_Z \quad (3.4)$$

The Zeeman energy levels are

$$E_m = -m\hbar\gamma B_0 \quad (3.5)$$

The value of *m* can vary depending on the spin value. For system where the spin is 1/2, *m* varies from -1/2 to 1/2.

Hamiltonian	**Interaction**	**Magnitude ~**
$\mathbf{H_z}$	Zeeman	10^8 Hz
$\mathbf{H_{cs}}$	Chemical Shift	10-10^4 Hz
$\mathbf{H_d}$	Dipole-dipole	10^2-10^5 Hz
$\mathbf{H_Q}$	Quadrupolar	10^3-10^9 Hz

Table 3.1. A list of the prominent NMR interactions and the magnitude of the interactions given in hertzs.

3.2 Chemical Shift

The first of the internal interactions to be examined is the chemical shift. The chemical shift is governed by interaction between the nuclear spin and the fields generated by surrounding electron current. Fields from electronic currents are induced by the applied external magnetic field. Thus the total magnetic field seen by the target nucleus spin is therefore different from the external applied B_0 field. The chemical shift from the Larmor frequency depends on the total field the spin sees. The total effective magnetic field, B_{eff}, is given by the equation below.

$$\vec{B}_{eff} = \vec{B}_0 + \vec{B}_{in} = \vec{B}_0 - \sigma\vec{B}_0 = (1 - \sigma)\vec{B}_0 \tag{3.6}$$

The Hamiltonian which describes the chemical shift is

$$\hat{H}_{CS} = \gamma\vec{\hat{I}} \cdot \vec{\vec{\sigma}} \cdot \vec{B}_0 \tag{3.7}$$

where σ, the chemical shielding, is a second rank tensor. The tensor has components of direction and conveys the magnitude B_{eff} at the nucleus to B_0 , the external magnetic field. The tensor is

$$\sigma = \begin{pmatrix} \sigma_{xx} & \sigma_{xy} & \sigma_{xz} \\ \sigma_{yx} & \sigma_{yy} & \sigma_{yz} \\ \sigma_{zx} & \sigma_{zy} & \sigma_{zz} \end{pmatrix} = \vec{D}^{-1}\sigma_{PAS}\vec{D} \tag{3.8}$$

Typically, the chemical shift is representred by its principal components via diagnalizing matrix $\vec{D}$

$$\sigma_{PAS} = \begin{pmatrix} \sigma_{11} & 0 & 0 \\ 0 & \sigma_{22} & 0 \\ 0 & 0 & \sigma_{33} \end{pmatrix} \tag{3.9}$$

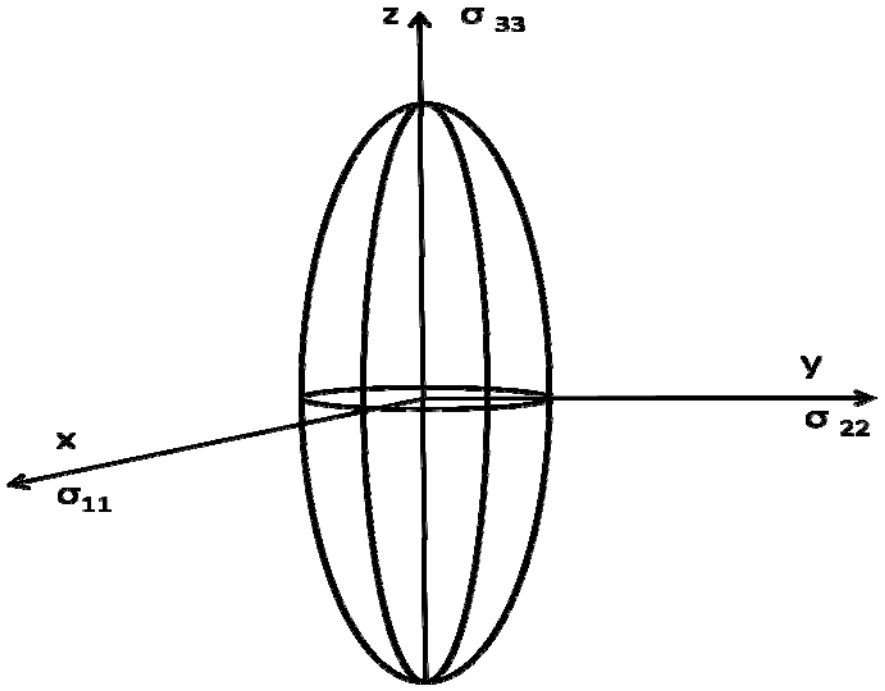

Figure 3.1. A three dimensional ellipsoid illustrating the principal axis associated with the chemical shielding tensor.

Such that

$$\sigma^{AV} = \frac{1}{3}(\sigma_{11} + \sigma_{22} + \sigma_{33}) \tag{3.10}$$

with

$$\sigma^{iso} = \sigma^{AV}\begin{pmatrix} 1 & 0 & 0 \\ 0 & 1 & 0 \\ 0 & 0 & 1 \end{pmatrix} \tag{3.11}$$

and anisotropy

$$\Delta\sigma = \sigma_{33} - \frac{1}{2}(\sigma_{11} + \sigma_{22}) \tag{3.12}$$

The chemical shift can be written in terms of the chemical shift tensors and it is

$$\delta = \sigma_{33} - \sigma^{AV} = \left(\frac{2}{3}\right)\Delta\sigma \tag{3.13}$$

Since the chemical shift interaction has orientation dependence, the spectrum will reflect the orientation of the chemical shift principal axis with respect to B_0. This has important implications for polycrystalline and amorphous materials. In a polycrystalline sample all orientations are realized such that the NMR spectrum reveals a distribution of resonance frequencies. Figure 3.2 shows in (a) a single crystal chemical shift spectrum oriented in the external field and (b) a spectrum of a particular powder sample where we have $\sigma_{11} \neq \sigma_{22} = \sigma_{33}$ and (c) another powder sample where $\sigma_{11} \neq \sigma_{22} \neq \sigma_{33}$. A single crystal can be at any orientation so when $\sigma_{11} \neq \sigma_{22} \neq \sigma_{33}$ the NMR spectrum would differ depending on the orientation. In other words, we observe a shift of the reference frequency upon a change in orientation

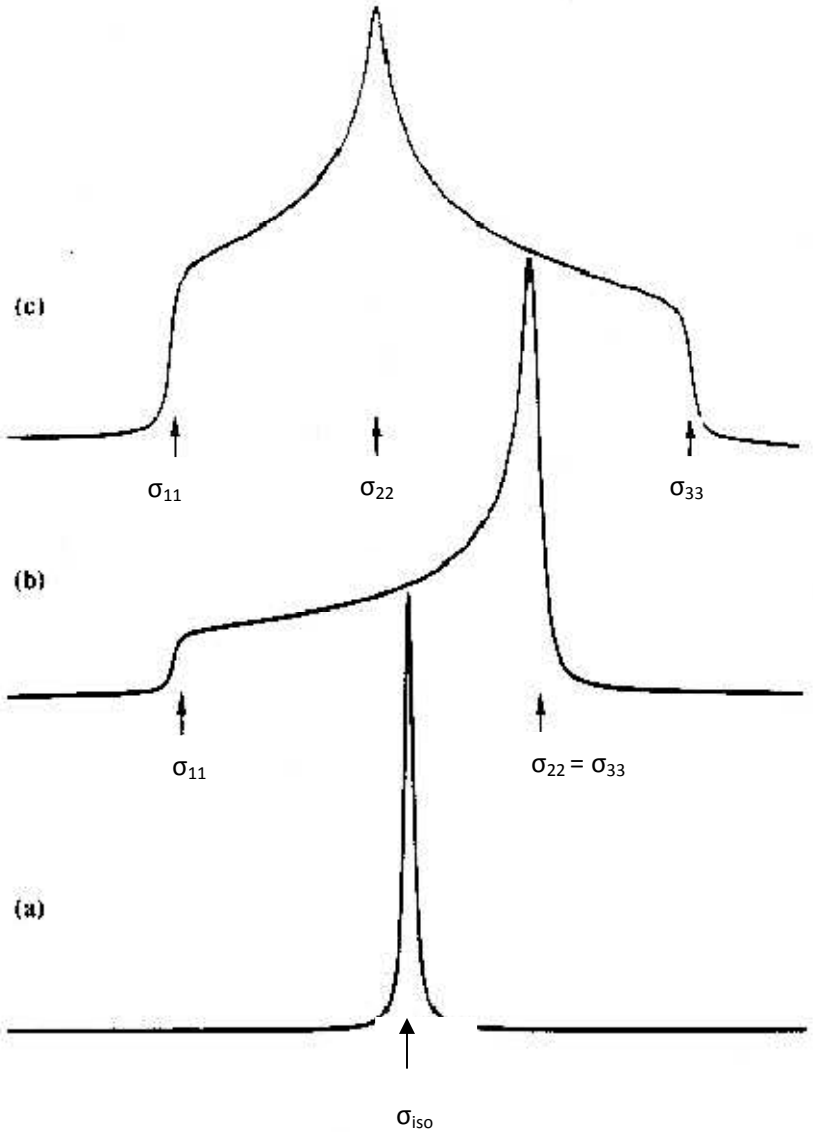

Figure 3.2. Individual spectum for a power sample and single crystal.

If we now return to the NMR spectrum we can note that it is a plot of the radio frequency, which has been applied, versus the absorption. The chemical shift can be defined as the frequency of the resonance expressed with reference to a well known and characterized standard compound, which is defined at 0 ppm. The scale that is used to display the NMR spectrum is often expressed in parts per million (ppm). The ppm scale is often used because it is independent of the

spectrometer frequency and thus more convenient for the purpose of analysis and comparison. We can express the formula for the chemical shift as

$$Chemical\ Shift\ \sigma = \frac{observed\ \ frequency - reference\ frequency}{reference\ frequency}\ x\ 10^6 \qquad (3.14)$$

and it is sometimes called δ.

3.3 Dipole-Dipole Interaction

There are other effects, as seen in Table 3.1 that contribute to the overall Hamiltonian. These effects are smaller than the Zeeman effect but they can be observed in NMR experiments. These smaller field effects interact with other neighboring nuclei. The near effects tend not to extend beyond 3 bond lengths. One such interaction is the dipole-dipole. The dipole-dipole interaction is on the order of 10^3 Hz. Dipole-Dipole interaction or dipolar coupling is the interaction of two nuclear magnetic moments with a non-zero spin ($I \geq 1/2$) separated by a distance r in an external magnetic field.

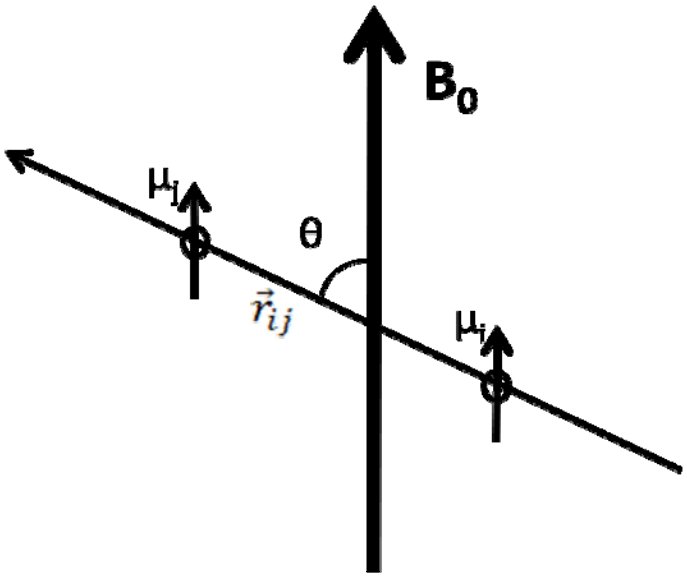

Figure 3.6 Two magnetic dipole moments in an external magnetic field B_0 separate by a distance r and an angle θ in reference to B_0.

$$\vec{r}_{ij}$$

The equation for the magnetic field of a dipole a distance $\vec{r}$ away is given by equation 3.15

$$\vec{B}_D(\vec{r}) = \frac{\mu_0}{4\pi}\frac{3(\vec{\mu}\cdot\hat{r})\hat{r} - \vec{\mu}}{r^3} \tag{3.15}$$

If the aforementioned magnetic dipole interacts with a neighboring dipole, the energy that is associated with the interaction of these two moments as seen above in figure 3.6 is

$$E_D = -\vec{\mu}\cdot\vec{B}_D \tag{3.16}$$

The result of the dot product is of the field and the magnetic moment is

$$= -\frac{\mu_0}{4\pi}\frac{3(\vec{\mu}_i\cdot\hat{r})(\vec{\mu}_j\cdot\hat{r}) - (\vec{\mu}_i\cdot\vec{\mu}_j)r^2}{r^5} \tag{3.17}$$

Finally upon replacement of $\vec{u}$ by operators the 1st –order representation of the energy between two dipoles is

$$\widehat{H}_D = -\frac{\mu_0}{4\pi}\frac{\gamma_i\gamma_j\,\hbar^2}{r^3}(1-3\,cos^2\,\theta)(3I_iI_j-\vec{I}_i\cdot\vec{I}_j) \tag{3.18}$$

Equation 3.18 shows that there is an angular or orientation dependence to the energy. Equation (3.18) can be for both similar nuclei (homonuclear) of dissimilar (heteronuclear) nuclei. In a macroscopic sized sample containing many $\vec{\mu}_i\cdot\vec{\mu}_j$ interactions, the dipolar Hamiltonian is generally represented by the summation. The dipole contribution (to the total energy) $\widehat{H}_D$ now becomes

$$\widehat{H}_D = -\sum_{i<j}\frac{\mu_0\gamma_i\gamma_j\,\hbar^2}{4\pi}\left[\frac{(\hat{I}_i\cdot\hat{I}_j)}{r_{ij}^3}-3\,\frac{(\hat{I}_i\cdot\vec{r}_{ij})(\hat{I}_j\cdot\vec{r}_{ij})}{r_{ij}^5}\right] \tag{3.19}$$

As previously stated there is an orientation aspect to the dipolar coupling. If the vector is aligned with $\vec{B}_0$ ($\theta = 0^0$) or is perpendicular ($\theta = 90^0$) as seen in figure 3.7 a), are obtains its characteristic spectrum. If the sample is that of a powder all orientations are realized and, there is a Pake pattern which emerges in figure 3.7 d). A Pake doublet is the collective sum of resonances for each crystallite within the powder, as they are randomly distributed throughout sample.

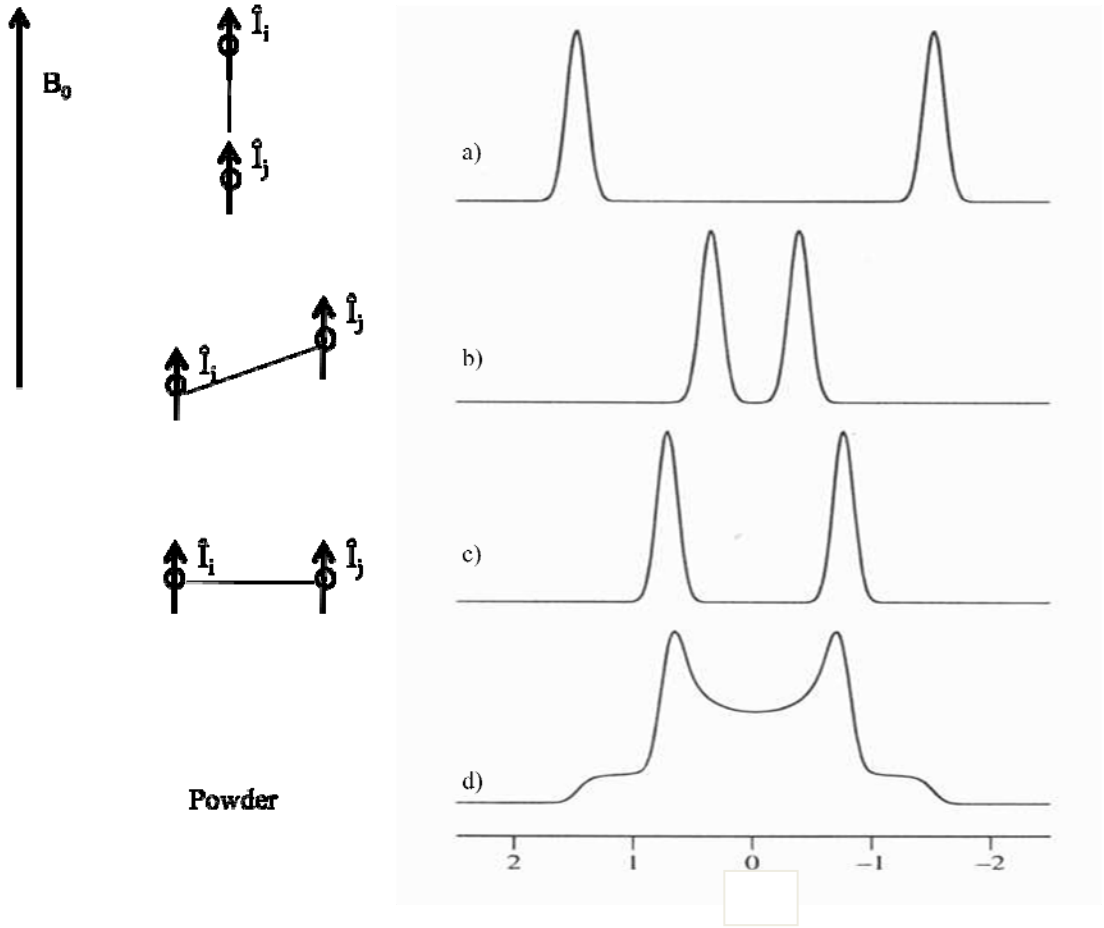

Figure 3.7 Dipole-dipole coupling with orientation dependence and associated peak pattern. [12]

In figure 3.8 we can see the peak separation of the NMR spectrum, as well as how the angular orientation affects the spectrum. The peak separation is primarily dependent on the distance between the two spins the orientation with respects to $\vec{B}_0$ and the gyromagnetic ratios.

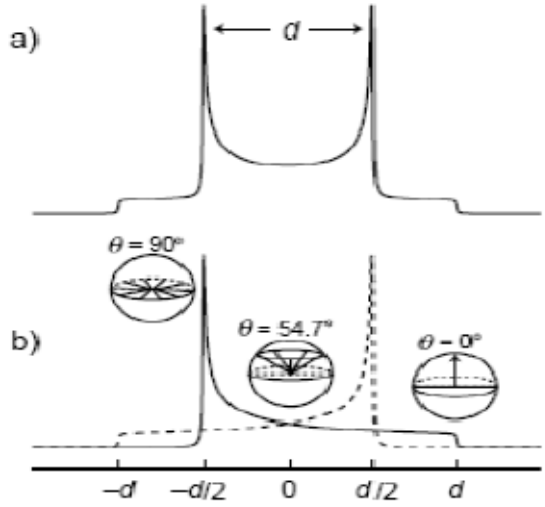

Figure 3.8 Pake Powder pattern of dipolar coupling with angular orientation shown [11].

From the above description of the dipole coupling in solid state NMR, we can determine distance and orientation information.

3.4 Quadrupolar Interaction

The quadrupole energy term results from the interaction between the nuclear quadrupole moment and the electric field gradient generated primarily by the bonding electrons. Nuclei with spin $I \geq 1$ have non-spherical charge metrical distribution [4], [5]. The magnitude of the asymmetry is eQ where e is the charge of the proton and Q is the nuclear quadrupole moment and is given by:

$$Q = \int \rho r^2 (3\cos^2\theta - 1) d\tau \qquad (3.20)$$

The integral is performed over the nuclear volume ($d\tau$) where ρ is the nuclearcharge density, r is the radial distance, and θ the angle $\vec{r}$ makes with the nuclear spin quantization axis. The charge distribution of nucleons affects the sign of Q. If Q is positive then the charge distribution is elongated, where as if it is negative then the charge distributions is flattened along the spin axis. The asymmetry of the charge distribution due to surrounding electrons gives rise to electric field gradient. The electric field gradient can be represented as a tensor, and the interaction of the nuclear quadrupole moment and the electric field gradient is the NMR quadrupolar interaction. The quadrupole interaction energy, $\widehat{H}_Q$, is given by the equation

$$\widehat{H}_Q = \frac{eQ}{2I(2I-1)\hbar}\vec{I}\cdot\boldsymbol{V}\cdot\vec{I} \tag{3.21}$$

where $\boldsymbol{V}$ is the EFG tensor and in the frame where $\boldsymbol{V}$ is diagonalized called the principal axis system (PAS). The Hamiltonian in the PAS then becomes

$$\widehat{H}_Q = \frac{eQV_{ZZ}}{4I(2I-1)\hbar}\left[(3I_z^2 - I^2) + \left(\frac{V_{xx}-V_{yy}}{V_{zz}}\right)\left(I_x^2 - I_y^2\right)\right] \tag{3.22}$$

where I is the nuclear spin, e is the electron charge, Q the electric quadrupolar moment of the nucleus and V_{xx}, V_{yy}, and V_{zz} are the components of the electric field gradient, EFG. The two primary contributions to the EFG come from charges of distant ions as well as incomplete valence electron shells. The EFG tensor, $\boldsymbol{V}$, when diagonalized can be written as

$$\boldsymbol{V} = \begin{pmatrix} V_{xx} & 0 & 0 \\ 0 & V_{yy} & 0 \\ 0 & 0 & V_{zz} \end{pmatrix} \tag{3.23}$$

where V_{xx}, V_{yy} and V_{zz} are its principal axes components. Since the V is traceless then we have

$$V_{xx} + V_{yy} + V_{zz} = 0 \tag{3.24}$$

In addition to the above characteristics, we have

$$|V_{zz}| \geq |V_{yy}| \geq |V_{xx}| \tag{3.25}$$

and the EFG asymmetry parameter, η, is defined by

$$\eta = \frac{V_{yy} - V_{xx}}{V_{zz}} \tag{3.26}$$

and it is bounded as follows: $0 \leq \eta \leq 1$. Another parameter is the quadrupole coupling constant

$$Q_{cc} = \frac{eQV_{zz}}{h} \tag{3.27}$$

and eV_{zz} is the largest component of the EFG. The quadrupolar interaction as previously stated leads to changes in the energy. The energy lines change by ω_Q, as understood by 1st-order treatment of equation 3.22 and shown in figure 3.10.

$$\omega_Q = \omega_Q^{PAS} \frac{1}{2} [3\cos^2\theta - 1 - \eta \sin^2\theta \cos 2\varphi] \tag{3.28}$$

where the frequency, ω_Q^{PAS}, of equation 3.28 is

$$\omega_Q^{PAS} = \frac{3eQV_{zz}}{\hbar 2I(2I-1)} \tag{3.29}$$

In equation 3.28 θ and φ are defined in relation to the coordinated system below in figure 3.9

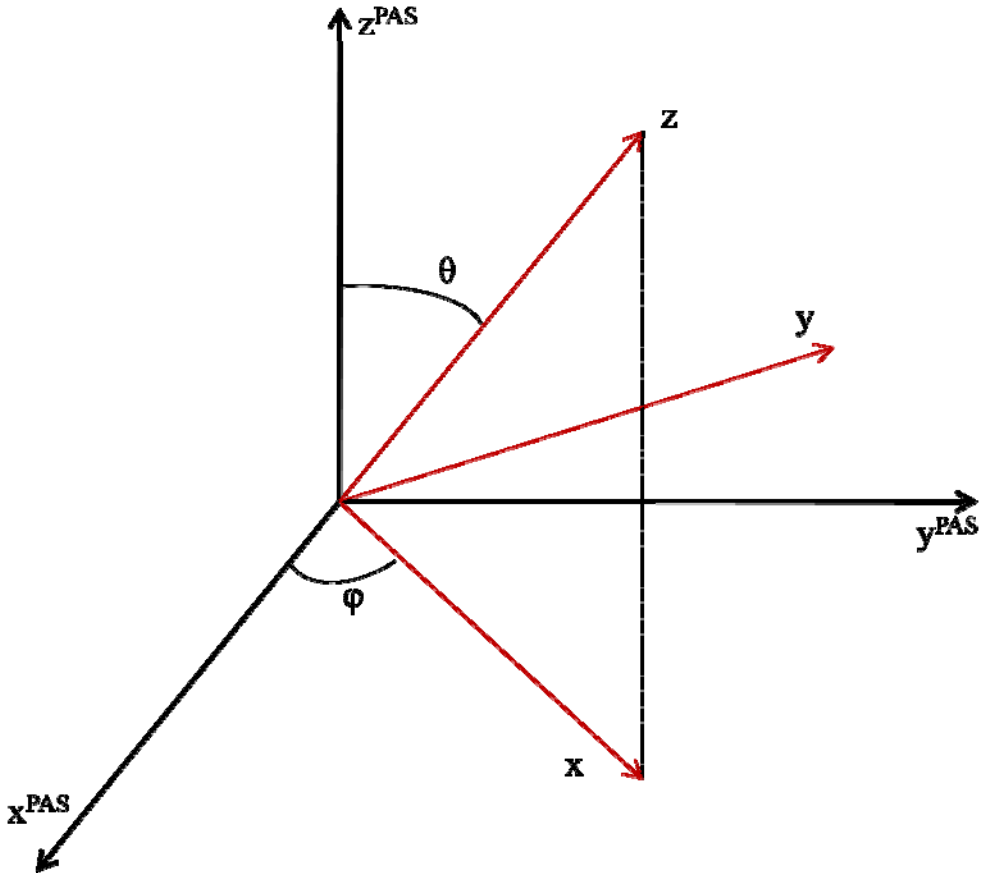

Figure 3.9 The principal axis coordinate system.

Finally, the energy that is associated with the levels is

$$E_m = \frac{1}{4\pi}\omega_Q \left[m^2 - \frac{1}{3}I(2I+1)\right] \tag{3.30}$$

The above is the high field approximation [6]-[10].

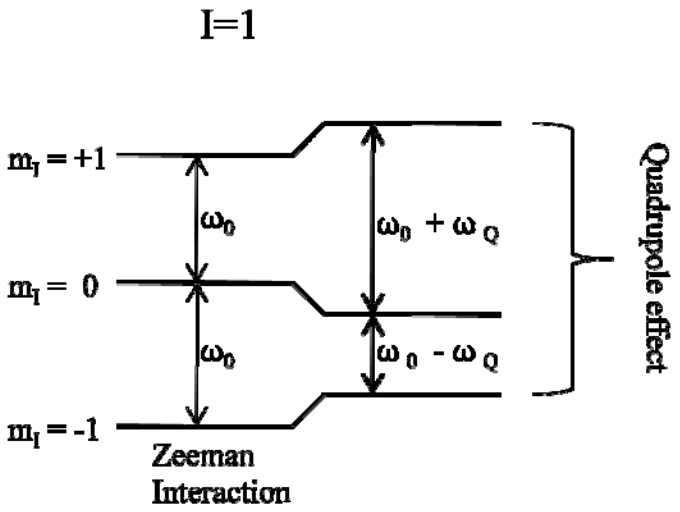

Figure 3.10 A system of spin $I = 1$ with the quadrupolar effect changing the energy levels from the initial Zeeman condition.

Quadrupolar interactions can lead to a powder pattern. For system of spin 1 there are two possible transitions ($2I+1$) as seen in figure 3.10. The resulting powder pattern leads to a similar outcome as observed in the dipole-dipole example of figure 3.7 d) . In the case of quadrupolar interaction the splitting similar to that shown in figure 3.7 is proportional to$Q_{CC}(1-\eta)$.

[1] A. Abragam *Principles of Nuclear Magnetism*, Oxford University Press 1999

[2] V.J. McBrierty and K.J. Packer, *Nuclear Magnetic Resonance in Solid Polymers*, Cambridge University Press, 1993

[3] J. L. G. Fierro *Spectroscopic Characterization of Heterogeneous Catalysts*, Elsevier Science Ltd, 1990

[4] I. Hung, A. Wong et al., *Journal of Magnetic Resonance*, 188 2007

[5] R. Liboff, *Introductory Quantum Mechanics* 4ed., Addison Wesley, 2002

[6] S.K. Strauss, *NMR Interactionns*, "www.chem.ubc.ca/faculty/straus/c518_08.html" 2007

[7] A. Godec and U Maver, *Solid State NMR theory and pharmaceutical applications*, National Institute of Chemistry Solvenia, 2008

[8] R.W. Schurko, I. Hung, C. L. B. Macdonald, and A. H. Cowley, Journal of American . Chemical Society , 124 (44) , 2002

[9] Z. Fang, *Accomplishment of VACSY experimental set-up and Its Application to Investigate Molecular Orientation Distribution of Solid-State Polymers* "http://sundoc.bibliothek.uni-halle.de/diss-online/99/99H200/t3.pdf", 1999

[10] R. Schurko, *Introduction to Solid State NMR*, "http://mutuslab.cs.uwindsor.ca/schurko/ssnmr/ssnmr_schurko.pdf" 2007

[11] Angewandte, Chemie International Edition 41,2002

[12] R.E. Wasylishen, Encyclopedia of NMR, Grant and Harris (eds.)

Chapter 4 - Solid State

4.1 Solid State NMR

Solid state NMR is characterized by anisotropic interactions that are not averaged out by rapid molecular motion inherent in liquids. The most important of these interactions were described in the previous section. Nuclear spins interact with one another and with electrons depending of the distance of their separation. The anisotropic interactions can lead to a variety effects. In addition to the spin-spin interaction we can have nuclei with electric quadrupole moments interacting with the electric field gradient in certain type of atomic environments. In the aforementioned interaction atomic bond distance is a key factor giving rise to these effects. Solid state NMR is defined by these anisotropic interactions. The characteristic effect of solid-state NMR is a splitting and broadening of the spectral lines, causing a dispersion of the resonant frequencies. These processes cause transverse relaxation time, T_2, of solid-state material to be shorter [1], [2], [3].

There is a need for high-resolution techniques to understand and determine the dynamical structures of solids, atomic and molecular orientations, bonding distances, and ionic motion. The use of a variety of pulse sequences and magic angle spinning has allowed for better NMR resolution in the solid state.

4.2 Bulk Magnetization and RF B_1 Interaction

The rotation of the bulk magnetization into the *x-y* plane is cause by the application of a radio frequency pulse of a set duration. The pulse is perpendicular to the external field B_0 and

can be oriented along the *x* or *y* axis. The process of applying the pulse and the subsequent rotation is illustrated below in figure 4.1.

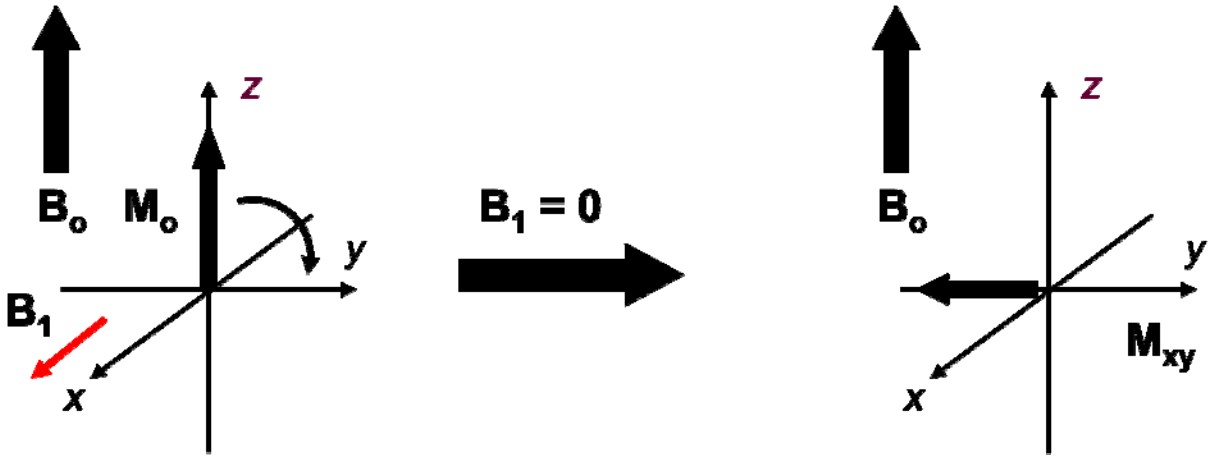

Figure 4.1. The rotation of the magnetization vector, $\vec{M}$, into the *x*-*y* plane by the application of the B_1 filed due to the rf pulse of a fixed duration.

The two fields B_1, generated by the RF pulse, and B_0 combine to form an effective field, B_{eff}. B_{eff} is the resultant vector of the combination of B_0 and B_1 as seen in the lab frame. Both fields together are present for a short time (equal to the B_1 pulse width) and during this period the bulk magnetization precesses around B_{eff}. The bulk magnetization contains a group of spins and the spins precessing exactly at the Larmor frequency (associated with B_0) feel primarily the effect of B_1. In the rotating frame these spins precess about B_1 for the duration of the pulse. The off resonance spins precess at a slightly different frequency, ω, from the Larmor frequency ω_0. These spins sense a different magnetic field which is given by

$$B' = \left(B_0 - \frac{\omega}{\gamma}\right) \tag{4.1}$$

where

$$B_{eff} = \left(B_0 - \frac{\omega}{\gamma}\right)\hat{k} - B_0\hat{\imath} \tag{4.2}$$

The Bloch equations provide a classical mathematical description of the evolution of the magnetization vector in the laboratory as well as the rotating reference frames. Another way to understand the evolution of the magnetization is depicted in figure 4.2. It is rotating in its relaxation return to the equilibrium state along the *z* axis. During this process the magnetization component along the *z* axis grows as the bulk magnetization $\vec{M}_{xy}$ component in the xy-plane becomes smaller.

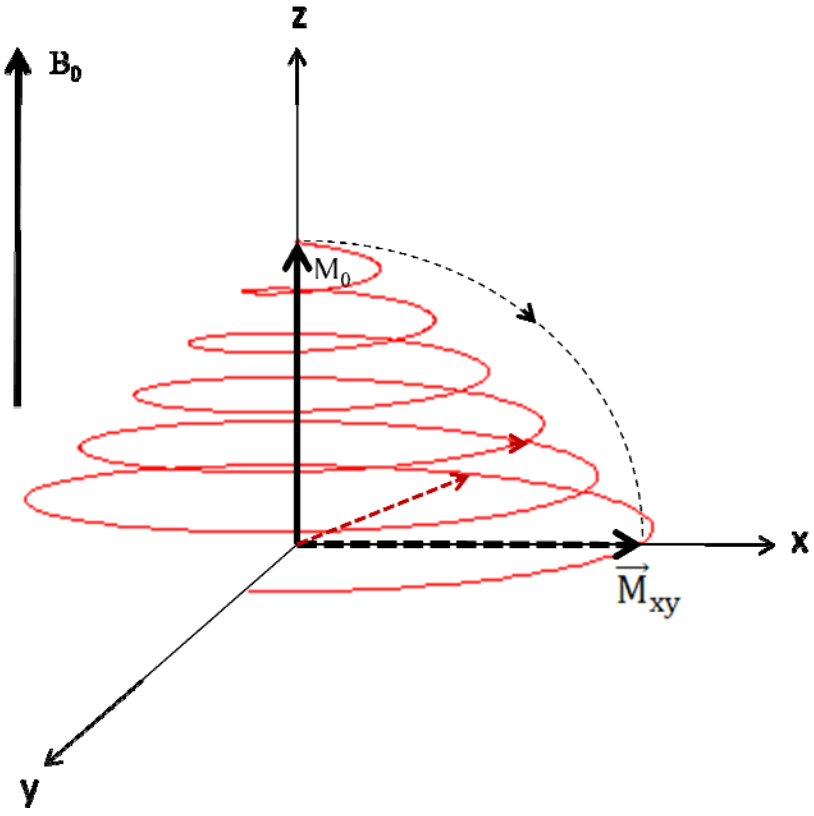

Figure 4.2. The precession of the bulk magnetization, in the laboratory frame, after B1 is applied and its return to the z axis.

The sinusoidal changes that are seen and measured in the decaying rotating magnetic field, $\vec{M}_{xy}$, as it returns to equilibrium leads to the formation of the FID. The resulting FID can be seen in the below figure 4.3.

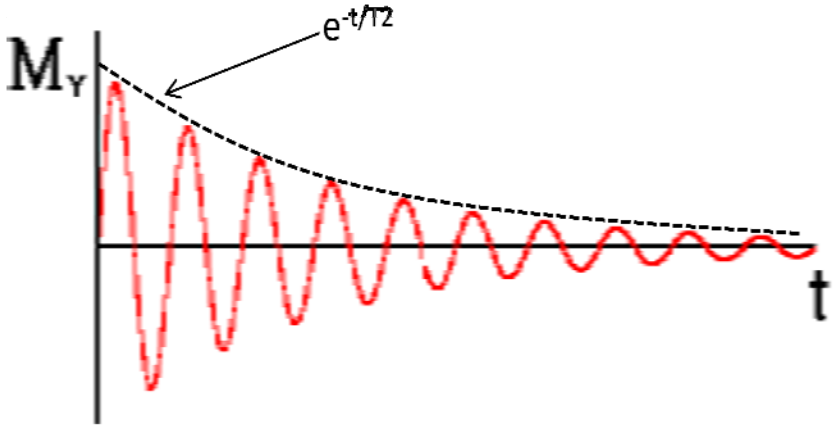

Figure 4.3 FID associate with the decay of the transverse magnetization.

In addition to the above description of the excited magnetization, is the relaxation process by which the magnetization recovers its initial value at thermal equilibrium.

4.3 Relaxation

The bulk magnetization, as seen in figure 4.2, precesses in the transverse plane for a finite time as it returns to a state of thermal equilibrium. The process of returning to the equilibrium state is called relaxation. There are two types of time constants that describe the behavior of returning to equilibrium. The time constant, T_1, is the time it takes the magnetization to return to the initial distribution of the α and β states. T_1 can also be understood as the time

taken for the excited nuclear spins to give back their energy to the surrounding lattice. The measuresd value of T_1 can give information about the molecular dynamics of the system that is being studied as seen below in figure 4.4

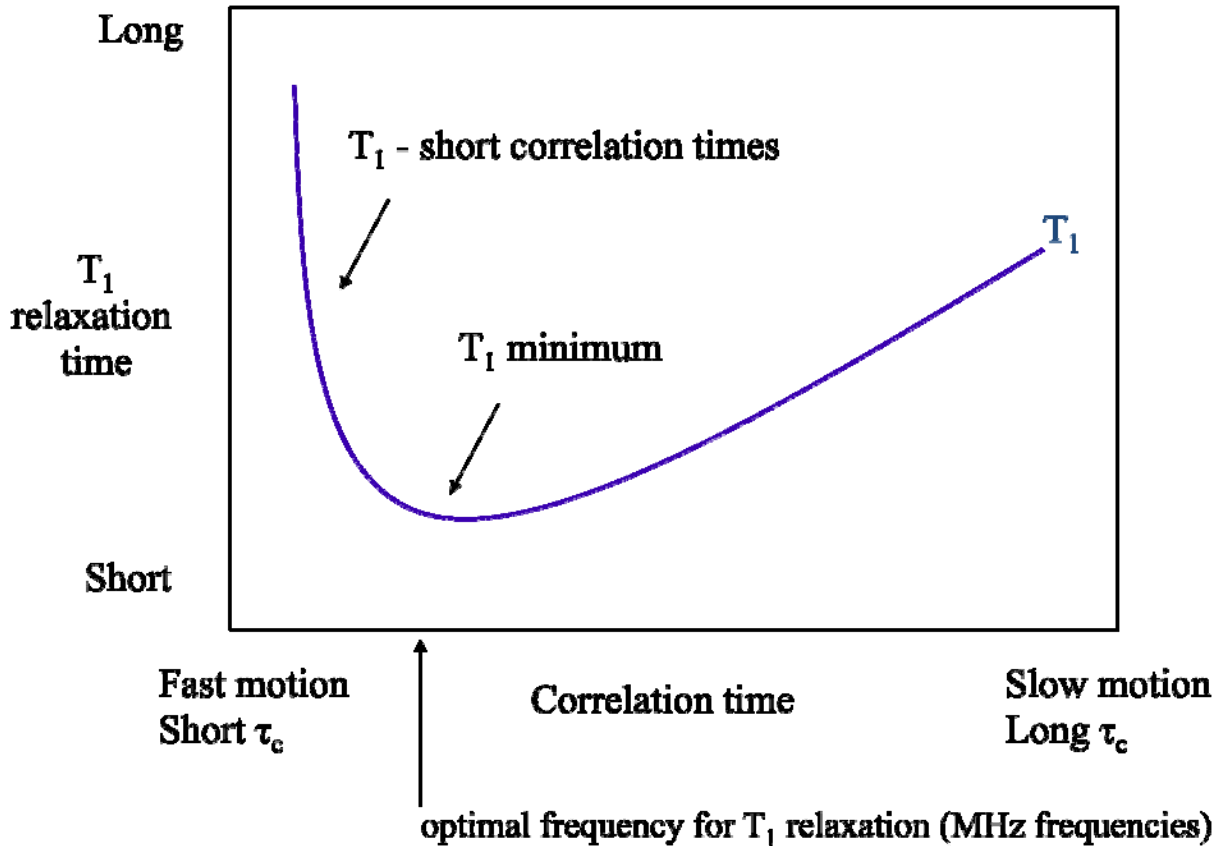

Figure 4.4 Graphical representation of T_1 time and the associated molecular dynamics.

The other time constant, T_2, is the de-phasing of the coherent transverse component of the magnetization vector in the *x*-*y* plane. Figure 4.3 shows the T_2 time constant as characterized by an exponential decay.

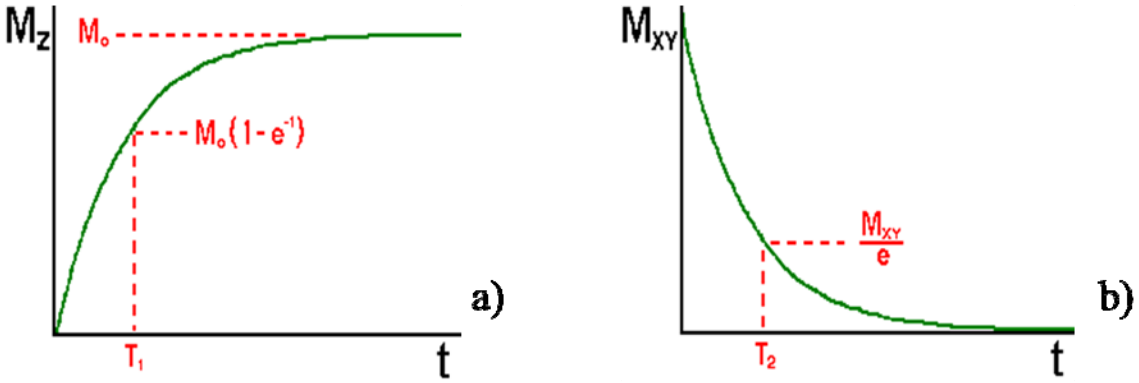

Figure 4.5 The above graphs illustrate the two relaxation processes. a) is a graph of the longitudinal relaxation and b) is a plot of the transverse relaxation as the magnetization dephases.

T_2 is the time it takes for the signal to decay to *1/e* of its original magnitude as illustrated in figure 4.5 *b)*. T_2 is related to the linewidth of an observed NMR signal and represents the width of the signal at half height is given by

$$\Delta\nu_{\frac{1}{2}} = \frac{1}{\pi T_2} \tag{4.3}$$

as shown in the figure 4.6 below.

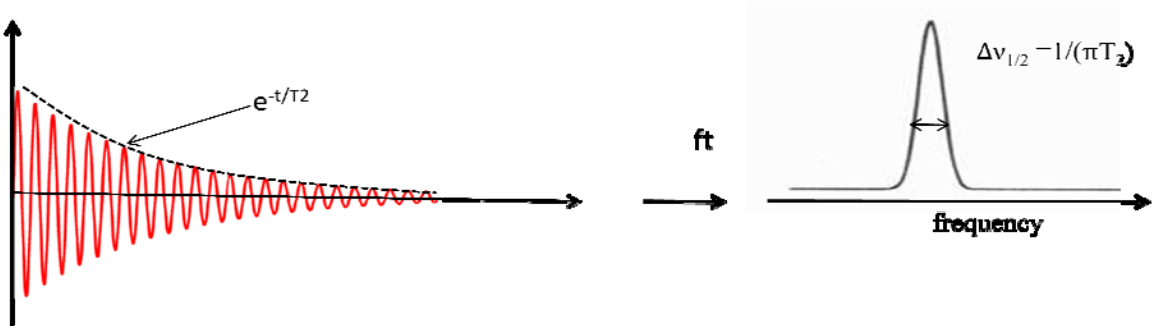

Figure 4.6 T_2 and its relationship to the FID and the fourier transformed NMR spectrum

4.4 NMR Pulse Techniques

NMR experimentation is heavily influenced by the pulse techniques that are used. These pulses are designed to extract information from the examined material. Because of environmental constraints, sample type and size pulse techniques are utilized to gain fragments

of information upon which interpretation is based. Below are a few of the fundamental pulse sequences that are used in order to gain, spatial, structural and dynamic information.

4.5 Magic Angle Spinning

The typical NMR experiment for a solid sample gives an absorption line of width greater than tens of kHz. This is due to the variation in local magnetic field or the quadrupole interaction (or both) as mentioned in previous sections. The main contributors to local field variation are the dipole–dipole interaction and the chemical shift anisotropy. Dipole-dipole, quadrupole interactions, chemical shift interactions have $(3\cos^2\theta\text{-}1)$ terms to first order in their mathematical representation. In solid state these terms exist and can obscure valuable information namely the isotropic chemical shift, that could be gained from a NMR spectrum, especially when overlap can obscure closely spaced lines. Magic angle spinning (MAS) introduces periodic mechanical motion at an angle of $\theta = 54.74^0$ with respect to $\vec{B}_0$. The $(3\cos^2\theta - 1)$ factor becomes zero when $\theta = 54.74^0$. The MAS spinning rate has to be greater than or equal to the magnitude of the static line width to achieve sufficient spectral narrowing. To accomplish this test samples are packed into rotors, which are then spun at rates from 1 to 40 kHz. The specific rate is experimentally limited by the rotor size, type of experiment and material being used. Spinning side bands can appear if the sample is spun at a rate less than the magnitude of the anisotropic. The spinning side bands are separated from the main peak by the spinning frequency[4], [5], [6].

4.6 90^0 pulse

The most basic pulse technique is the 90^0-pulse sequence. The 90^0-pulse is designed to rotate the bulk magnetization into the *x*-*y* plane. The carrier frequency must be equivalent to the Larmor frequency and cause a change of spin state from α to β. Once the RF pulse has perturbed the sample to its new state a Free Induction Decay (FID) will follow as it returns to the equilibrium position or as spins diphase in the *x*-*y* plane. Applying a Fourier Transform to the time dependent FID will give us the frequency domain or spectrum. The duration of the pulse and the B_1 amplitude are the factors that determine the flip angle for the sample. The flip angle is given by $\theta = \gamma B_1 t_p$ where t_p is pulse length. Below, in figure 4.7 is an example of pulse with t_p duration that is applied to a target nucleus. It produces a FID, which then is Fourier transformed from time domain to a frequency domain NMR spectrum. The rf-pulse excites a broad range of frequencies.

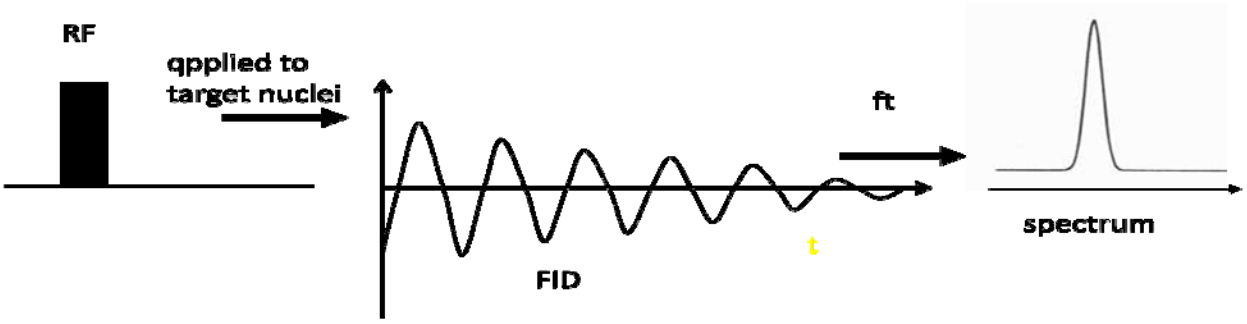

Figure 4.7 The application of a NMR pulse to a target nuclei and the resultant signal is transformed into a NMR spectrum.

Thus in attaining a 90^0 flip angle it is desirable to use sufficient RF power so as to limit the pulse duration for adequate spectral average [7], [8].

4.7 Inversion recovery

Inversion recovery is a pulse sequence used to determine T_1 that consists of using a 180^0 followed by a 90^0 which leads to the FID. The first pulse rotates the magnetization, $\vec{M}$, 180^0 from the positive z to $-z$ axis. Time τ is the delay that allows $\vec{M}$ to partially recover. On its way to recovery a 90^0 pulse then samples the partially recovered magnetization. This technique is especially helpful if T_1 is short (less than *1* second).

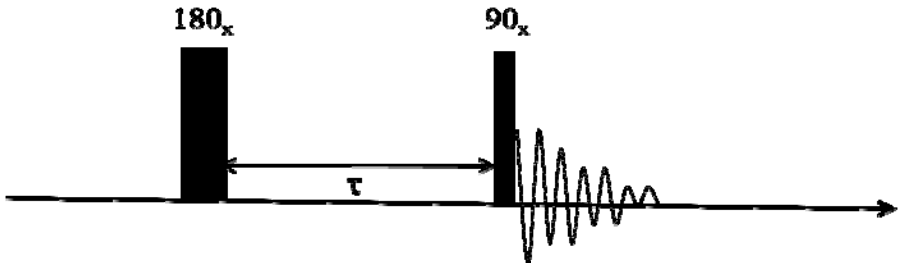

Figure 4.8 A 180^0, 90^0 pulse sequence used in the determination of T_1.

4.8 Saturation recovery

The saturation recovery pulse sequence is made up of a series of *90°* pulses separated from one another by equivalent periods of time. The *90°* RF pulse rotates the bulk magnetization, which is parallel to B_0, from the *z*-direction into the *xy*-plane. In order to saturate the sample a sequences consisting of multiple *90°* RF pulses are generated at relatively short repetitive times.

The main purpose of saturation recovery is to measure long T_1 times more accurately than an inversion recovery pulse sequence [7].

4.9 Cross Polarization and heteronuclear decoupling

Solid State NMR cross polarization experiments are performed to enhance the resonance signal. Nuclei which have a low gyromagnetic ratio, γ_s, or low natural abundance are enhanced by the transference of magnetization from a resonant nucleus that has a high gyromagnetic ratio γ_i. The transference of energy occurs when frequencies are matched in the rotating frame as seen in figure 4.9. This is called the Hartman-Hahn condition and is given by the equation within the same figure [9], [10], [11]. The equation shown is for the case of ^{13}C and ^{1}H nuclei. In addition when we use this technique we can improve the signal to noise ratio by a factor of γ_{1H}/γ_{13C}.

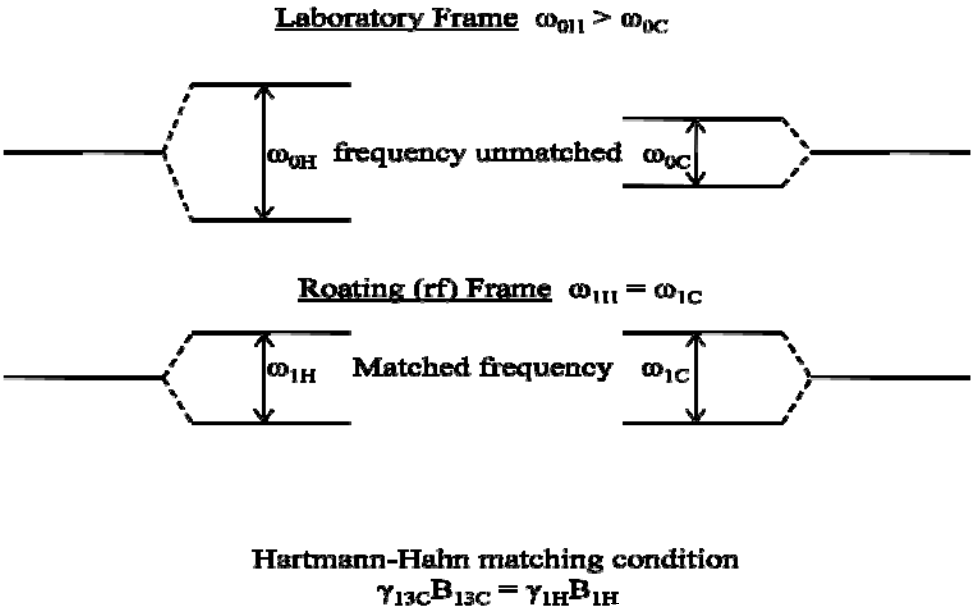

Figure 4.9 Hartmann-Hahn condition showing the process of frequency matching from the laboratory frame to the rotating frame.

Cross polarization is typically accomplished by 'spinlocking' the transverse magnetization so

that the field strengths for the two nuclear species satisfy the Hartmann-Hahn matching condition. The ratio of the pulses is approximately $4B_{1_H}$ to $1B_{13_C}$as illustrated in figure 4.10.

Cross polarization experiments are often combined with the MAS roto-synchronization technique (CP/MAS NMR) in addition to proton decoupling during detection as seen in the below figure.

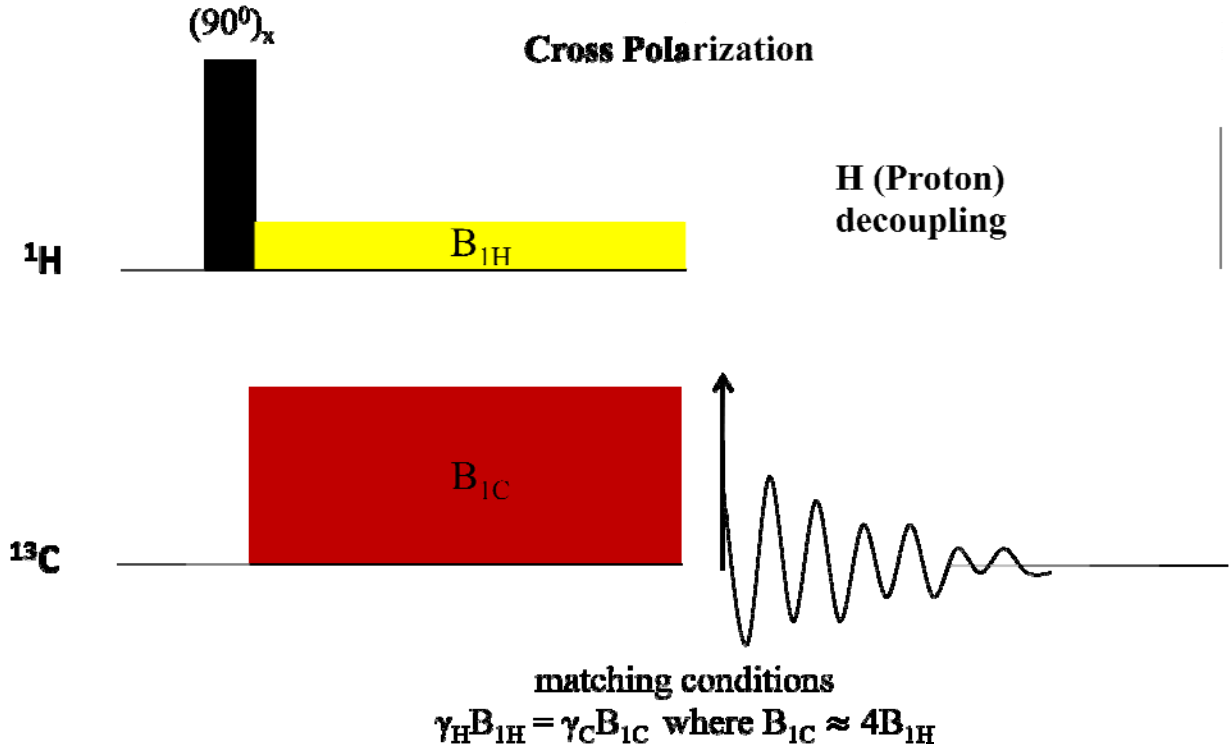

Figure 4.10 The Hartmann-Hahn matching in conjunction with a proton decoupling

After CP we want to eliminate the influence of the proton on the carbon as it evolves during the FID [12], [13]. Decoupling occurs on the order of the width of the proton line. Solid state NMR CP MAS has become a standard experiment in for nuclei with spin *1/2*. CP MAS with decoupling suppresses line broadening caused by ^{13}C and ^{1}H dipolar coupling. The MAS portion

alsoaverages out the chemical shift anisotropy [14], [15]. The CP enhances measurement sensitivity.

[1] M. Levitt, *Spin Dynamics: Basics of Nuclear Magnetic Resonance*, John Wiley & Sons, 2001

[2] M.J. Duer, *Introduction to Solid-State NMR* , Wiley-Blackwell, 2005

[3] G. Gauglitz, and T. Vo-Dinh, *Handbook of Spectroscopy*, (2 Vol. Set), Wiley-VCH, 2003

[4] L.J. Mathias, *Solid State NMR of Polymers*, 1ed, Springer, 1991

[5] C.P. Slichter, *Principles of Magnetic Resonance* 3ed. Springer-Verlag 1990

[6]] R. Liboff, *Introductory Quantum Mechanics* 4ed., Addison Wesley, 2002

[7] S.K. Strauss, *NMR Interactionns*, "www.chem.ubc.ca/faculty/straus/c518_08.html"

[8] D. J. Griffiths, *Introduction to Quantum Mechanics* 2ed. Benjamin Cummings, 2004

[9] T.L. James, *Fundamentals of NMR*, Department of Pharmaceutical Chemistry University of California, 2008

[10] G. Moyna, *NMR lectures in Advanced Spectroscopy*, "http://tonga.usip.edu/gmoyna/NMR_lectures/NMR_lectures.html", 2008

[11] A. Godec and U Maver, *Solid State NMR theory and pharmaceutical applications*, National Institute of Chemistry Solvenia, 2008

[12] O. Zerbe , NMR Spectroscopy Lecture Course, “http://www.oci.uzh.ch/group.pages/zerbe/” 2005

[13] S. Strauss, Solid State NMR: Cross Polarization, “http://www.chem.ubc.ca/faculty/straus/Nlecture17.pdf” 2007

[14] *Basic Cross Polarisation* “http://www.dur.ac.uk/resources/SSNMR/three5.pdf” Durham University, Solid-state NMR Service 2002

[15] S. Hafner and H.W. Spiess, *Concepts in Magnetic Reso*nance, 10 (1), John Wiley & Sons, 1998

Chapter 5 - Electrolyte additives

5.1 Introduction

Many of today's technological devices require battery power for operation. The demands for a battery that can produce consistent power over several hours have grown with industry and consumer demands for portability. These batteries must be able to meet a wide variety of demands and application formats. They are used in mp3 players, cellular telephones, personal media center players and others devices. Other areas where battery life and function are vital are aerospace and medical devices. Their requirements are similar to the aforementioned technological devices but they include environments that are challenging. One such area is space exploration. One of the challenges of aerospace requires that batteries operate efficiently over a great temperature range. The ability to consistently charge and discharge over the life of the battery is crucial especially when the battery cannot readily be replaced.

One of the processes that prevent long battery life and effective recharging is a layer that builds on the interface between the battery electrodes and the electrolyte. This film that develops is called the solid electrolyte interface or SEI. The internal operation of a lithium ion battery is based on electrochemical reactions which produce a variety of reaction products. The formation of these reaction products starts upon the contact of the electrolyte with the electrodes. The reaction is accelerated by the operation of the battery as it discharges and recharges or with increase in temperature during operation or storage. The initial formation of the SEI serves as a protection layer for the electrodes. This passivating film reduces the level to which the electrode will react further with the electrolyte. However further decomposition of the solvent and the

lithium salts leads to significant surface build up. A thicker SEI layer contributes to the impedance of the lithium ion in reaching the electrode [1], [2].

Many commercial batteries perform well around room temperature but their operation can be critically affected by significant rise or fall in temperature. It is widely known that the electrolytes have poor thermal stability at temperatures above 60^0C. Lithium Hexafluorophosphate, $LiPF_6$, is one of the most widely used salts in electrolytes of Li-ion batteries because it has high ionic conductivity but it too is vulnerable to hydrolytic and thermal instability. Thermal degradation of lithium ion batteries has been linked to the decomposition of $LiPF_6$, for example, into LiF and PF_5. The PF_5 is considered a strong Lewis acid which in turn reacts with carbonates to form a variety of reduction products [3], [4].

Other carbonates added to the electrolyte are believed to selectively change the reduction reactions that take place at the anode, leading to improvements in battery performance. Example of this kind of additive are vinylene carbonate (VC) and vinyl ethylene carbonate (VEC). Both VC and VEC appear to form a passivating film that prevents solvent co-intercalation and exfoliation of the graphite at lower potentials [4], [5], [6]. A baseline electrolyte that is composed of a mixture of alkyl carbonates with $LiPF_6$ performs well at low temperatures. The formulation of this electrolyte is 1:1:1 (vol. %) of ethylene carbonate (EC): diethyl carbonate (DEC): dimethyl carbonate (DMC) with 1 M $LiPF_6$.

The cathode in this investigation $LiCo_xNi_{1-x}O_2$ is a highly regarded material for Li-ion batteries. The Co provides stabilization of the structure while Ni gives higher capacity than the well-known $LiCoO_2$ compound.

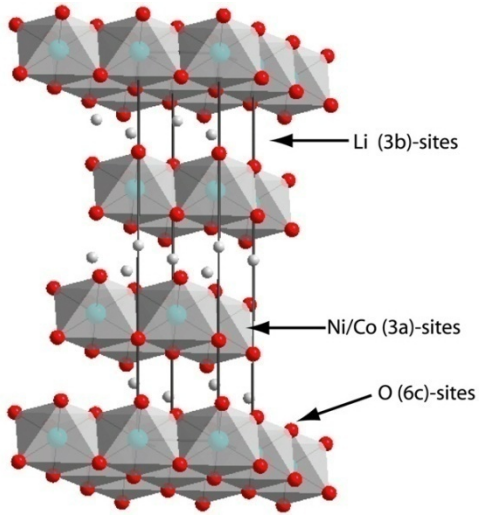

Figure 5.1. Lithium Nickel Cobalt Oxide structure

This layered structure, as seen above is formed from alternating $NiCoO_6$ and LiO_6 octahedral edges. In this structure the Ni and Co ions play an important role. They each are trivalent and low spin state. The Ni^{3+} is paramagnetic and the Co^{3+} is diamagnetic [7] – [15].

The use of MAS NMR can now probe the nature of both the cathode and anode material hopefully distinguishing between Li in the active material and Li in the SEI. The effects of electrolyte additives on the surfaces of six battery electrodes were investigated [16] –[18].

5.2 Experimental

The samples were prepared and supplied by Dr. Marshall Smart of the Jet Propulsion Laboratory. Each battery cell investigated is constructed of a mesocarbon microbead (MCMB) anode and a cathode of a form $LiNi_{1-x}Co_xO_2$ with x = 0.20. All cells were constructed with a

baseline of 1.0 M solution of $LiPF_6$ in ethylene carbonate (EC) + diethyl carbonate (DEC) + dimethyl carbonate (DMC) in a 1:1:1 v/v % electrolyte. All cells were charged to an approximate potential of 3.8 volts then followed by a full discharge. The specific cell voltage potential is calculated by subtracting the anode potential from the cathode potential. The electrode potentials were measured with respect to the reference electrode in a three electrode cell. The following are the composition of each cell with the anode potential and cathode potential listed:

BL01 = 1.0 M LiPF6 EC+DEC+DMC (1:1:1 v/v %) (Baseline Electrolyte)

Cell Voltage = 3.78 V

Anode Potential = 0.472 V

Cathode Potential = 4.25 V

BL02 = 1.0 M LiPF6 EC+DEC+DMC (1:1:1 v/v %) + 1% DMAc (DMAc = dimethyl acetamide)

Cell Voltage = 3.78 V

Anode Potential = 0.202 V

Cathode Potential = 3.99 V

BL04 = 1.0 M LiPF6 EC+DEC+DMC (1:1:1 v/v %) + 10 % DMAc (DMAc = dimethyl acetamide)

Cell Voltage = 3.80 V

Anode Potential = 0.231 V

Cathode Potential = 4.03 V

BL05 = 1.0 M LiPF6 EC+DEC+DMC (1:1:1 v/v %) + 3% NMP (N-methyl pyrrolidinone)

Cell Voltage = 3.75 V

Anode Potential = 0.227 V

Cathode Potential = 3.98 V

BL06 = 1.0 M LiPF6 EC+DEC+DMC (1:1:1 v/v %) + 1.5 % VC (VC = vinylene carbonate)

Cell Voltage = 3.79 V

Anode Potential = 0.197 V

Cathode Potential = 3.99 V

The DEC, DMAc,DMC, EC, NMP and VC structures are shown in the appendix.

As seen above in addition to the baseline electrolyte each cell had a different solvent co-additive, 1% dimethyl acetamide, 10% dimethyl acetamide, N-methyl pyrrolidinone, and vinylene carbonate. Charge-discharge measurements and cycling tests were performed with an Arbin battery cycler. The cycling tests were done at current densities of 0.25 mA/cm^2 (~ C/12 rate) and 0.50 mA/cm^2 (~ C/6 rate) for charge and discharge, respectively. The cells were charged to 4.10V, followed by a tapered charge period at constant potential for three hours, and discharged to 2.75V, with 15 minutes of interval between the charge/discharge steps. After, all cells were held at 70^0C in the fully charged state for 10 days, the electrodes were rinsed for approximately 60 seconds in a beaker of DMC (50- 100 ml) and again in a second beaker for 60 seconds. Each cell was fully discharge prior to analysis. The preparation for NMR analysis, both for the cathode and anode material, was done by scraping it from the current collectors and packing the material into a 3.2 millimeter rotor. The NMR samples were packed in an Argon

filled glove box with an oxygen and water content of one to several ppm. All rotors were filled to the same volumetric level in order to better compare the spectral results.

All ^{7}Li NMR studies were performed on a 7.1 Tesla Chemagnetics CMX-300 spectrometer. The resonance frequency use for ^{7}Li nucleus was 116.98 MHz and static as well as the Magic Angle Spinning (MAS) experiments were performed using a Chemagnetics MAS probe. NMR spectra were collected with a 4μs π/2 pulse for both static and MAS measurements. The MAS rate of spinning for all tests was approximately 20 KHz. The chemical shift for all spectra is referenced relative to aqueous lithium triflate, LiTf, at 0 ppm..

5.3 Results and Discussion

A static ^{7}Li NMR study was performed on the five anode samples labeled BL01, BL02, BL04, BL05 and BL06 and figure 5.2 shows a super position of spectra. The control spectrum is BL01 which does not have additional compound in the electrolyte. As seen in the figure, there is a central prominent peak near 0 ppm in all spectra which represent primarily lithium in the SEI and in some cases other sites such as higher-stage intercalated Li which will be discussed later. However spectra BL02, BL04 and BL05 presents additional peaks which indicates the presence of the satellite transition peaks that are characteristic of *3/2* spin ^{7}Li nucleus as well as another component near 50 ppm which will be discussed later. Also, the central peak in the spectrum for BL06 is slightly shifted and the signal is reduced.

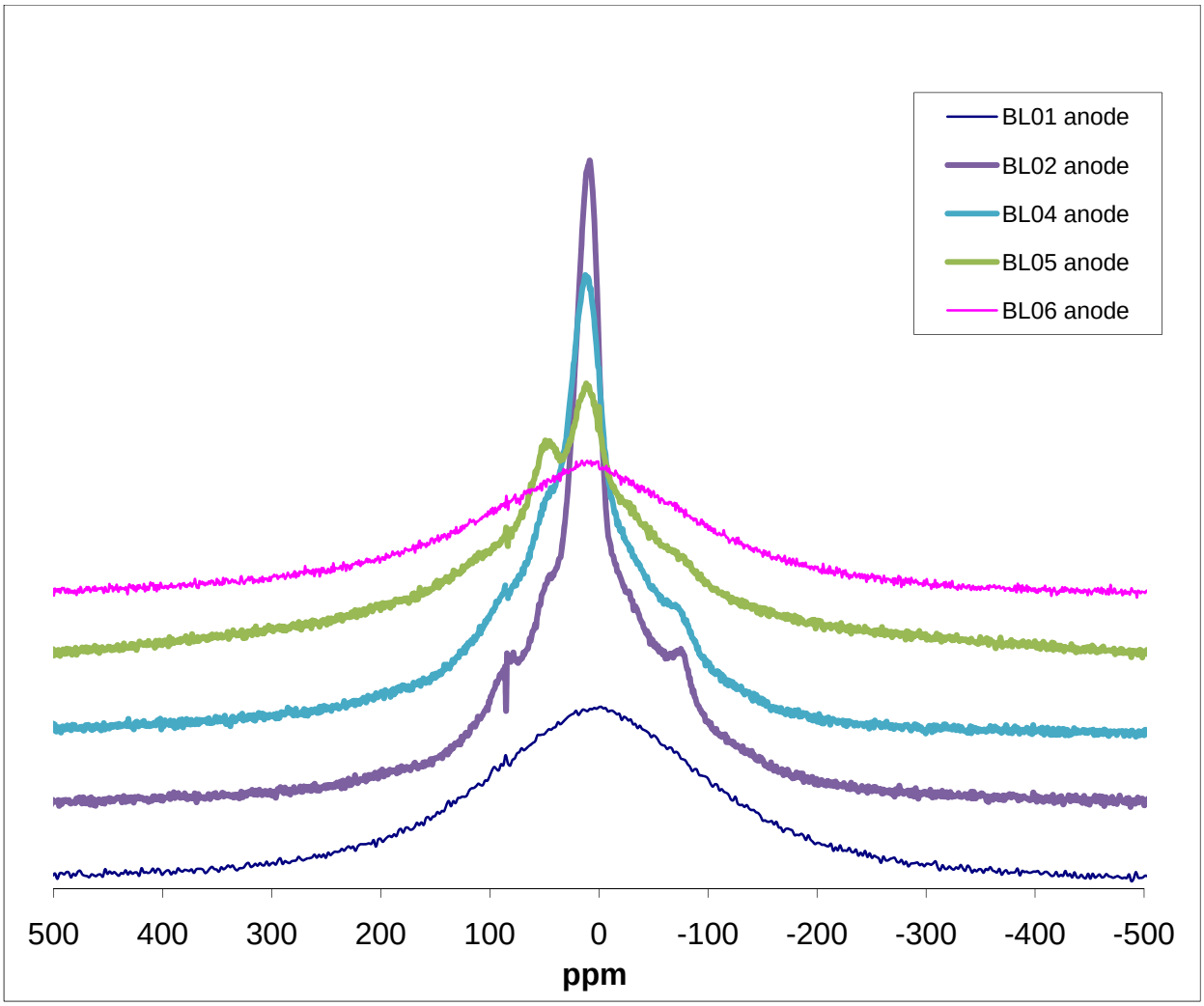

Figure 5.2 ^{7}Li wide-line NMR spectra of cycled anode material.

Further analysis of figure 5.2 reveals additional information. Specifically addition of 3% NMP to sample BL05 and 1.5%VC to BL06 shifted the location of the central peak slightly down field from the 0 ppm position to -9 ppm for BL05 and -8 ppm for BL06. In addition, there is an emergence of a Knight shifted second peak in BL05 at 53 ppm which is characteristic of metallic intercalated LiC_6 which is also present to a lesser degree in BL02 and BL04. The intensity and linewidth differences observed for the central peak suggest different reactions are occuring at the electrode compared to the baseline spectra. These reactants are found within the

SEI and give rise to the central peak in the wide-line spectra. The broad featureless spectra of BL01 and BL06 suggest a broad distribution of species, some of them likely containing protons, which give broadening due to dipole-dipole coupling. This could have been verified by ^{1}H decoupling, which unfortunately was not done.

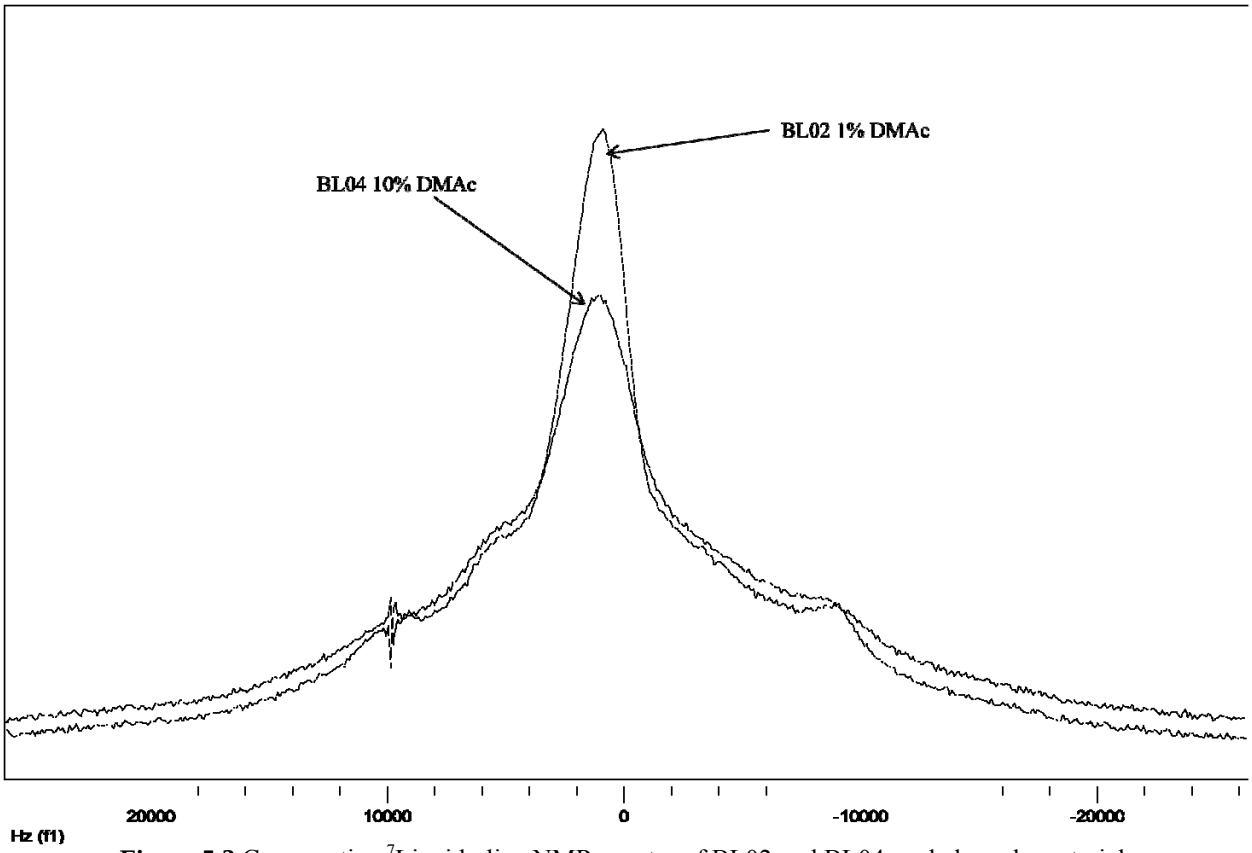

Figure 5.3 Comparative ^{7}Li wide-line NMR spectra of BL02 and BL04 cycled anode material.

The wide-line ^{7}Li *3/2* spin NMR spectra in figure 5.3 for anode sample BL02 and BL04 show the classical quadrupole transition pattern with the central transition about 8 ppm and two satellites transition. They represent the characteristic powder pattern of ^{7}Li nuclei between graphite planes. The powder patterns illustrate a typical lithium quadrupole satellite spectrum and it suggests a crystalline structure this ^{7}Li site, and is consistent with higher stage (i.e. LiC_x, x>6) intercalated graphite [23]. In addition a quadrupole coupling constant (QCC) of 37.7 kHz

for BL02 and 37.9 kHz for BL04 was analyzed. The spectrum of both samples show an asymmetry about the central transition peak. This is due to metallic lithium at 47 ppm and 45 ppm respectively. The increase in the solvent concentration from 1% DMAc in BL02 to 10% DMAc in BL04 suggests the crystalline structure remains relatively the same as illustrated in the similarities of the powder pattern observed in the above superimposed spectra in figure 5.3. The persistence of the well defined powder pattern implies the presence of ordered phases that are not affected by DMAc solvent concentration.

Wide-line spectra do not provide enough distinction between the lithium species therefore MAS was employed to give better resolution to the peaks. This resolution will provide the necesary distinction between intercalated and non-intercalated ^{7}Li as well as possible lithium site differences within the SEI. Since all samples were cycled in the same manner, peak intensies can give an indication to the level of SEI build up as it relates to the type of additional additives

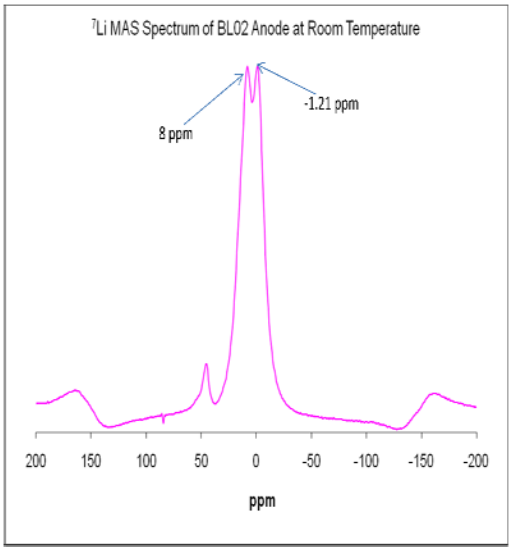

Figure 5.4 ^{7}Li MAS spectrum with 1%DMAc solvent with 10% DMAc with resonance at -1.2, 8 and 45 ppm.

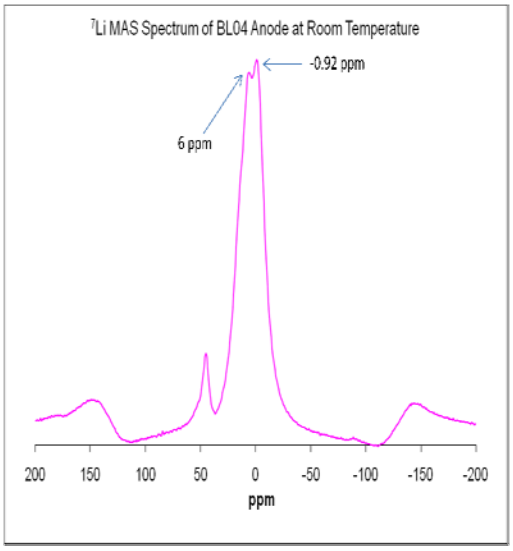

Figure 5.5 ^{7}Li MAS chemical shift spectrum additive and peaks at -0.9, 6 and 45 ppm.

The high resolution MAS spectra of BL02 and BL04 are shown in figures 5.4 and 5.5 respectively. There are several resolved components in BL02. The first is observed at -1.21 ppm

and the other at 8 ppm which are believed to be bound lithium in the SEI. The other peak occurs at 45 ppm which is intercalated lithium, identified as a the stage 1 graphite intercalation compound, LiC_6. BL04 main peak is right shifted from the reference standard. It occurred at -0.92 ppm and again attributed to the SEI layer. In addition there is a secondary ^7Li peak at 6 ppm. The shifts at 6 and 8 ppm could possibly also be attributed to $LiC_{x>12}$ or higher stage intercalation compound. The peak at 45 ppm again is graphite intercalation of the LiC_6 form [4].

Table 5.1 Experimentally determined MAS 7Li anode data for all samples.

Samples (completely discharged)	Electrolyte Additive (anode)	Main Peak Linewidth (Hz)	Intercalated Li^+ Peak Linewidth (Hz)	Chemical Shift Main Peak (ppm)	Chemical Shift Intercalated Li^+ peak (ppm)
BL01	Baseline	4040	No intercalated ions	-2.09	No intercalated ions
BL02	1% DMAc	2354	888	-1.21 and 8.0	45
BL04	10% DMAc	2513	887	-0.92 and 6.0	45
BL05	3% NMP	2468	974	-1.90	45
BL06	1.5% VC	4029	No intercalated ions	-2.61	No intercalated ions

In looking at Table 1, the baseline electrolyte BL01, and compare it to samples BL02 and BL04 would indicate that the addition of DMAc at both concentrations changes slightly the range of the lithium compounds found in the SEI. However DMAc also causes the formation of the secondary lithium peaks assigned to graphite intercalation compounds. The potential candidates in the SEI include LiF and covalently bonded lithium compounds (which occur between +6 to -6 ppm) but LiF has been identified in literature as occurring -1 ppm [1]. A comparison of the ratio of intercalated lithium peaks, occurring at 45 ppm, to the main peaks suggests that the increase in DMAc leads to more intercalation. This is also reflected in the difference in SEI peak intensities from BL02 to BL04. Sample BL05 is also consistent with the reduction of lithium in the main SEI peak with the addition of 3% NMP carbonate. The emergence of the LiC_6 peak at 45 ppm, and $LiC_{x>12}$ peaks at 6 and 8 ppm caused by the additives for BL02, BL04 and BL05, suggests that these compounds affect the reversibility of the lithium ions. When the material is cycled it is possible that lithium remains trapped in the anode and is no longer available for discharge. The VC additive in BL06 does not generate a secondary Knight shifted peak. This would imply that during cycling lithium is removed from the anode and available for further cycling.

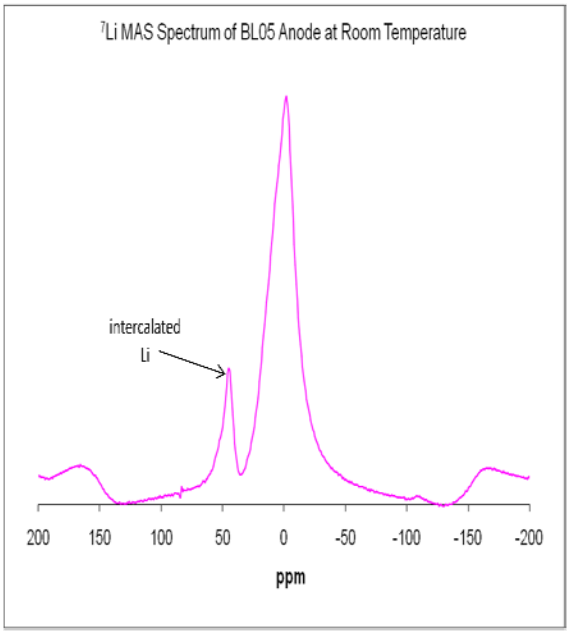

Figure 5.6 ^{7}Li MAS spectrum of the 3% N-methyl pyrrolidinone solvent.

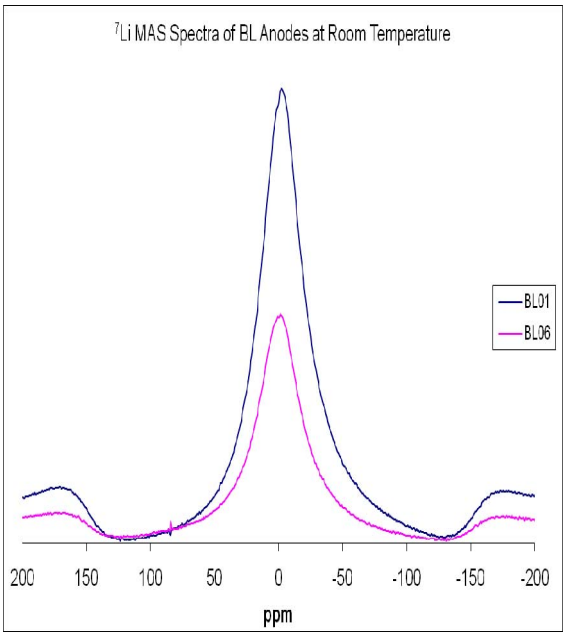

Figure 5.7 ^{7}Li comparison of the baseline electrolyte to BL06 with 1.5% vinylene carbonate additive.

Sample BL05 with 3% NMP additive, as shown in figure 5.6, main peak occurs at -1.9 ppm which is attributed to the SEI while the 45 ppm peak is similar to the peaks in samples BL02 and BL04. The final spectrum BL06 1.5% VC exhibits only a single peak at -2.6 ppm. The VC additive does not significantly change the spectral characteristic of the SEI as compared to the baseline sample BL01. However the additive in BL06 reduces the intensity of the SEI peak. This would imply that the 1.5% VC cause less SEI build-up during the cycling process. The two samples have comparable line width, 4029 Khz (BL06) and 4040Khz (BL01). Table 1 illustrates that the additives in the 1% and 10% DMAc as well as 3% NMP cause narrower linewidth of the SEI component as compared to BL01 and BL06. If we compare the wide line peaks of samples BL01 and BL06 we see that they are both somewhat asymmetrical. Except for the lower intensity of the peak, there is very little change between the baseline BL01 and the addition of the 1.5% VC of the BL06 sample, except for the lower intensity of the peak. The

larger linewidth of BL01 and BL06 compared to the other samples could be due to greater structural heterogeneity, i.e. a distribution of chemical shifts, or heteronuclear dipole broadening from nearby protons or a contribution of both factors.

Table 2 ^{7}Li MAS cathode data for all samples.

	Electrolyte Additive (cathode)	Main Peak Linewidth (Hz)	Ni^{3+} associated Peak Linewidth (Hz)	Chemical Shift Main Peak (ppm)	Chemical Shift Ni^{3+} associated peak (ppm)
BL01	Baseline	1273	2273	-0.60	191
BL02	1% DMAc	1244	8381	-0.99	232
BL04	10% DMAc	1209	4056	-1.96	212
BL05	3% NMP	1373	3438	-1.92	294
BL06	1.5% VC	2011	12609	+1.44	238

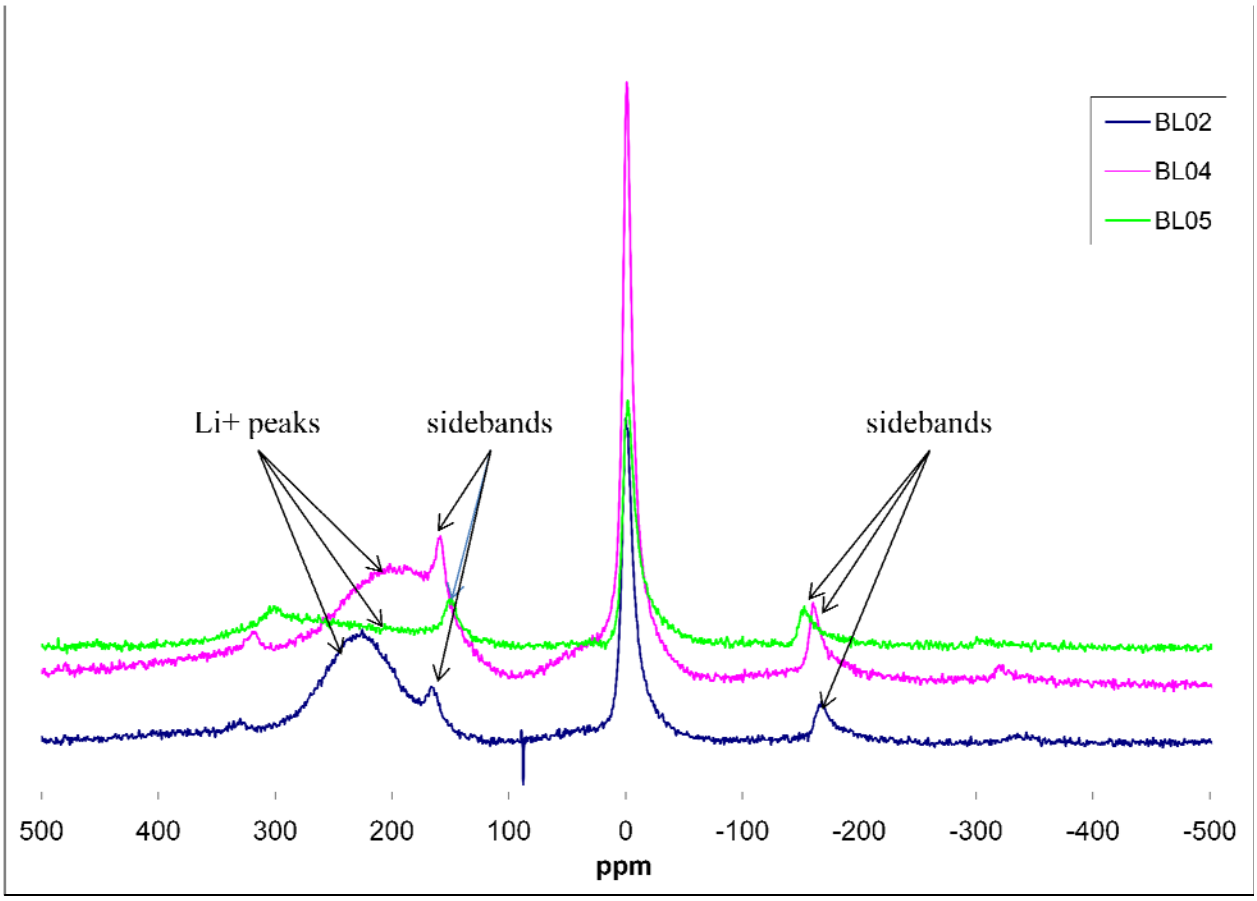

Figure 5.8 BL02, BL04 and BL05 MAS NMR superimposed spectra with delineated sidebands and lithium peaks.

The MAS spectra for the $LiCo_xNi_{1-x}O_2$ cathode where generated with an approximate spin rate of 20 KHz. Table 2, cathode BL02 with 1% DMAc, main peak is situated at -1.0 ppm. A much broader Li^+ peak centered at 232 ppm is present. This is cause by a paramagnetic shift associated with Ni^{3+}, as is the broad width of this peak [19] - [22]. Sample BL04 10% DMAc data is shown in the same table. The peaks are similar to the 1% DMAc with the main peak occurring at -1.96 ppm and the paramagnetic shifted peak at 212 ppm. The 212 ppm peak as compare to the 232 ppm peak may be explained by a higher average oxidization of Ni, with a greater amount of diamagnetic Ni^{4+} present. The paramagnetic peak widths are dissimilar in size for BL02 and BL04. The relatively sharp peak near zero ppm is attributed to SEI formation, as

the starting $LiNi_{0.8}Co_{0.2}O_2$ material shows only the Ni^{3+} associated peak. Normally, the starting (or fully discharged) cathode exhibits a peak position at about 500-600 ppm[8][ ]. The observation of a smaller shift in the present series suggests that the samples are not fully discharged (i.e. contain more diamagnetic Ni^{4+} at the expense of paramagnetic Ni^{3+}). BL05 with 3% NMP spectral peak occurs at -1.92 ppm. It too has a second paramagnetic shifted peak but centered at 294 ppm.

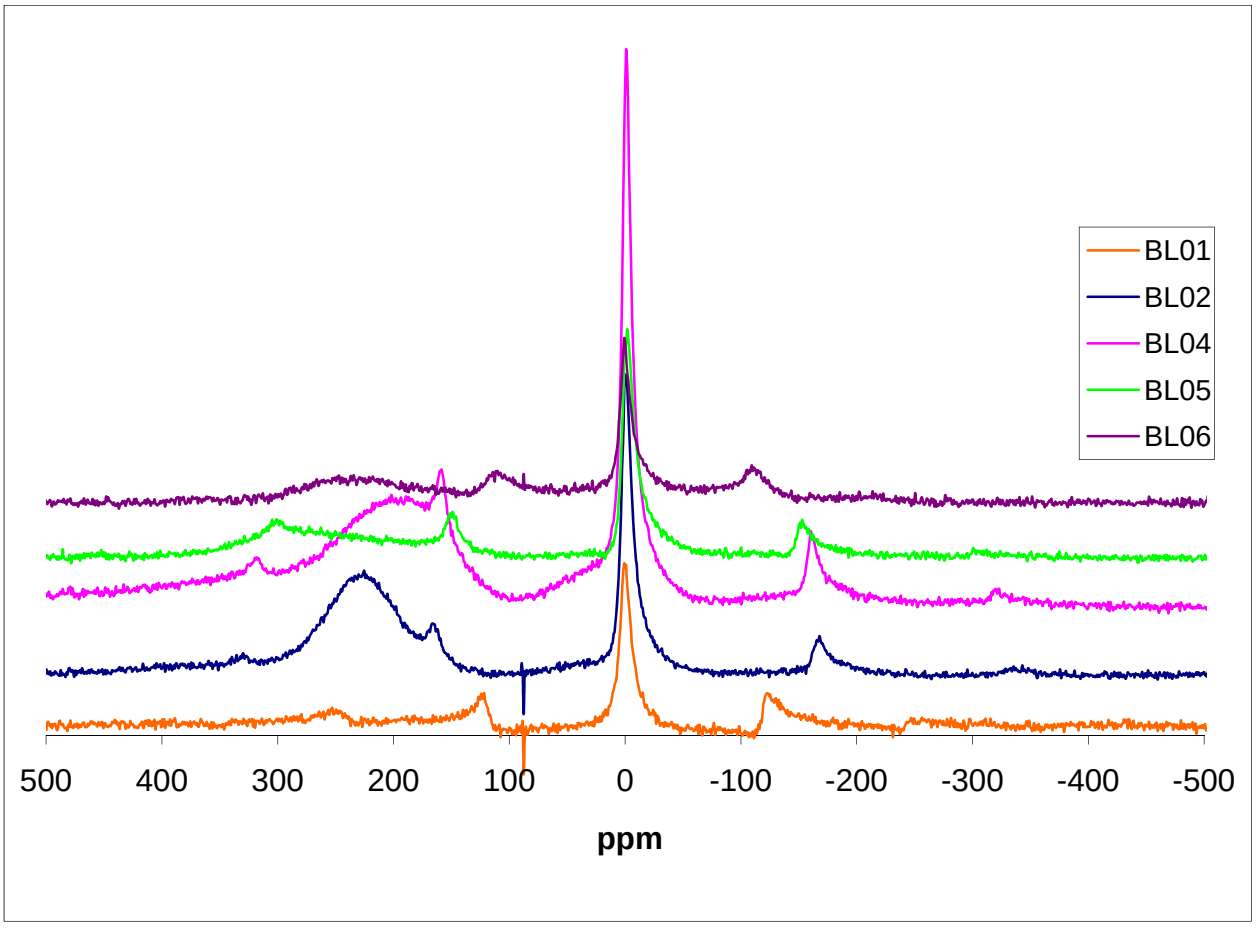

Figure 5.9 Shows the superposition of BL01 – BL06 spectra.

5. 9 shows the superposition of BL01 through BL06. The linewidth of the central peak of BL06 (1.5% VC) is significantly broader than any other peak. The main lithium peak in the SEI is left shifted and occurs at 1.44 ppm.

5.4 Conclusion

Different additives where tried in order to improve the performance characteristics of lithium ion battery. The aim has been to create electrolyte materials which allow better intercalation and de-intercalation at the electrodes by forming a more favorable SEI. The carbonate based solvent additives do affect the SEI formation thus affecting battery performance. We have demonstrated in a quantitative way that certain additives lead to different levels of lithium irreversibility during cycling as well as formation of the passivating layer. The irreversible lithium, in the anode, correlates well with the Ni^{3+}/Ni^{4+} ratio that are in the cathode SEI. The unavailable lithium trapped in the anode leads to more Ni^{3+} in the cathode SEI and a greater paramagnetic shift of the associate lithium. Further studies, such as fluorine NMR, should be performed in order to specify the influence that the solvent salt, $LiPF_6$, has on the chemical composition of the SEI. The charge state of the disassembled electrodes (both anode and cathode) as determined by NMR does not necessarily correspond to the cell potential values upon cell disassembly, indicating that regions of the electrodes were no longer in electrical contact with the current leads.

[1] B.M. Meyer, S.G. Greenbaum, and C.P. Grey, *Electrochemical and Solid-State Letters*, 8 (3) 2005

[2] Y. Wang, X. Guo, S.G. Greenbaum, J. Liu and K Amine, Electrochemical and Solid-State Letters, 4 (6) 2001

[3] Y. Wang, S. Nakamura, K. Tasaki, and P.B. Balbuena, *Journal of American Chemical Society*, 124, 2002

[4] M.C. Smart, B.V Ratnakumar, X. Zhang, S.G. Greenbaum, C.C. Ahna, and B Futz, *Journal of The Electrochemical Society*, 146 (11), 1999

[5] G. Chen, G.V. Zhuang, T.J. Richardson, G. Liu and P.N. Ross Jr., *Electrochemical and Solid-State Letters*, 8 (7), 2005

[6] Y. Matsuda, T. Fukushima, H. Hashimoto, and R. R Arakawa, *Journal of The Electrochemical Society*, 149 (8), 2002

[7] S. Gautier, E. Frackowiak, J. Conard, J.N. Rouzaud, F Beguin, "http://acs.omnibooksonline.com/data/papers/1997_ii148.pdf" 1997

[8] J.R. Dahn, A.K. Sleigh, S. Hang, B.M Way, Q. Zhang, and U. von Sacken, *Elsevier*, Amsterdam, 1994

[9] C. Delmas, I Saadoune and A. Rougier, *Journal of Power Sources*, 43, 1993

[10] W. Li, and C. Curie, *Journal of The Electrochemical Society*, (144), 1997

[11] J. Cho, G. Kim, and H.S. Lim, *Journal of The Electrochemical Society*, (146), 1999

[12] M. Carewska, S. Scaccia, S. Arumugan, Y. Wang, and S. G. Greenbaum. Solid State Ionics, (93), 1997

[13] S. Castro-Gracia, and C. Julien, *Ionics*, (4), 1998

[14] D. Kim, J. Sohn, C. Lee, J. Lee, K. Han, and Y. Lee, *Journal of Power Sources*, (132), 2004

[15] R. Sott, J. Granander, and G. Hilmersson, *Journal of The American Chemical Society*, (125) 2004

[16] D. Carlier, M. Menetrier, C.P. Grey, C Delmas, and G. Ceder, *Physical Review B*, (67), 2003

[17] M.S. Ding and T.R. Jow, *Journal of The Electrochemical Society*, (151), 2004

[18] H, Ora, Y. Sakata, A. Inoue and S. Yamaguchi, *Journal of The Electrochemical Society*, (151), 2004

[19] D. Carlier, M. Menetrier, and C. Delmas. *Journal of Materials Chemistry*, (11), 2001

[20] I. Saadoune, and C. Delmas, *Journal of Solid State Chemistry*, (136) 1998

[21] I. Saadoune, M. menetrier, and C. Delmas, *Journal of Material Chemistry*, (7) 1997

[22] C. Julien, ans S.S. Michael, *Ionics*, (4), 1998

[23] Y. Wang, V. Yufit, X. Guo, E. Peled, and S. Greenbaum, *Journal of Power Sources*, (94) 2001

Chapter 6 - ^{1}H NMR Study of Carbon Nanotubes

6.1 Introduction

Carbon Nanotubes are composed of tubes of graphitic carbon which enhance critical properties in various materials [1]. They can enhance mechanical, electrical, and thermal properties of the materials in which they are placed. Carbon nanotubes belong to the fullerene group of carbon-based structures. Single wall carbon nanotubes (SWNT) are one of the possible forms that the microscopic carbon fibers can take. They are one atomic layer thick and the tube diameter is generally measured in nanometers, with a length to diameter ratio not normally greater than 10000.

Carbon nanotubes have been proposed as fibers to mechanically reinforce polymers [2]. The SWNT form is being used for reinforcing polymer matrices and is heralded as the ultimate carbon reinforcement [3]. The nanotubes are dispersed throughout the polymer matrices in the melt. It is extremely important that they distribute evenly between the long and short polymer chains to ensure effectiveness in strengthening a desired property. Failure to disperse leads to a phase separation due to the strong surface interactions between the tubes [4] , and will diminish the structural integrity that SWNT are to provide. Nanotubes within the polymer may slide and have poor interfacial bonding leading to inhibited load transfer from the matrix to the fiber [5]. Changing or functionalizing the SWNT surface is important in order to avoid the aforementioned

difficulties. The specific goals of functionalization are to disrupt and minimize the diameter of the rope like structure that form, improve nanotube dispersion and nanotube-polymer interaction, and possibly separate nanotubes by type [6]. The prime method for achieving functionalization in polymers with nanotubes is by fluorination. Fluorination is one of the few methods that is easily scalable and does not require a solvent for the functionalization reaction to take place [7],[8]. Improved dispersion of fluorinated nanotubes in composites and increased mechanical properties have already been observed in the works of Zhu [9] and Geng [1 0]

The polymers studied here are Polybutadiene (PB) and Polyisobutylene (PIB). PB and PIB are both synthetic rubber, or elastomers. Nuclear Magnetic Resonance studies can elucidate the structural and dynamical properties of the SWNT polymer composite. Studying PB and PIB with and without SWNT allows us to draw some conclusions about the effect at the SWNT's on polymer chain mobility [3], [4], [11].

6.2 Experimental

A typical fabrication of the PB/SWNT composite involved dissolving 0.10 grams of PB in benzene and suspending 0.01 grams of SWNTs in the liquid. The benzene containing the suspended SWNTs and dissolved PB was allowed to slowly evaporate while being subjected to sonication. The evaporated PB containing the SWNTs was dried for two hours at 75 C. The PIB composite was fabricated in a similar manner. Both the single walled and fluorinated carbon nanotubes were obtained from Carbon Nanotechnologies Incorporated where they are grown by the HiPCO process. Examination of these pristine tubes by paramagnetic resonance indicates the presence of a ferromagnetic signal arising from the iron nanoparticles which serve as the catalyst for growth.

NMR measurements were conducted on a Chemagnetics CMX300 spectrometer, operating at a ^{1}H NMR frequency of 301.0 MHz. Variable temperature NMR spectra were obtained by Fourier transformation of the transient signals following either single pulse or solid echo excitation, with approximately 2 μs pulse widths. Wide-line (static) rather than magic angle spinning NMR was deliberately employed in order to better assess the effect of motional narrowing as a function of temperature. Spin-lattice relaxation times (T_1) were determined by the inversion recovery method.

6.3 Results and Discussion

The wideline proton NMR spectra of PB without SWNT at several temperatures are shown in figure 6.1.

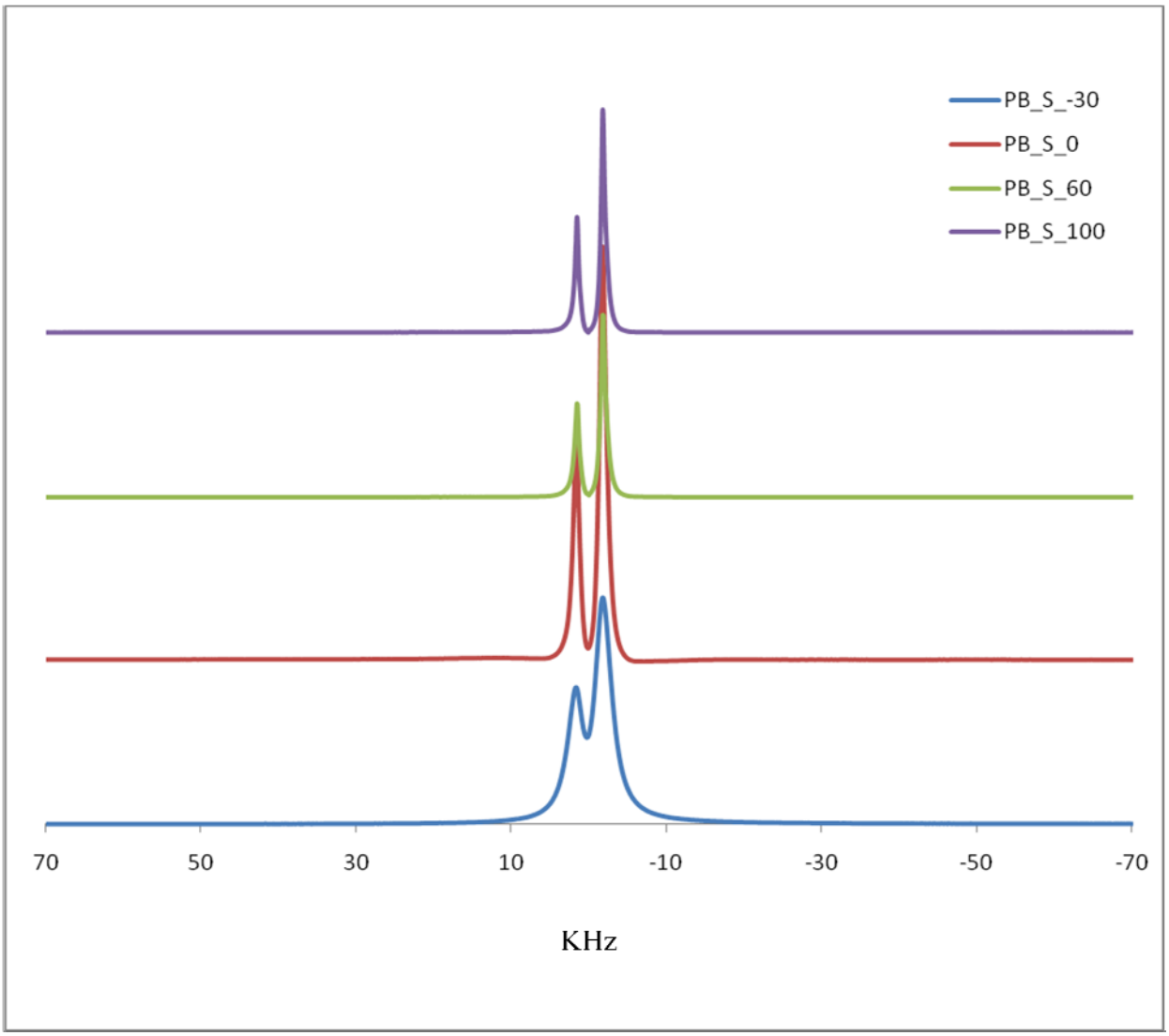

Figure 6.1. PB spectra displayed at various temperatures.

There are two distinct ^{1}H sites corresponding to different chemical environments, namely CH and CH_2 sites. A modest degree of motional narrowing, for both peaks, is observed above $-30^{0}C$ as well as discontinuities of both peaks between -20 and $-10^{0}C$, as shown later, possibly due to a glass transition. The spectra of the PB_SWNT and PB_FSWNT samples are displayed in figures 6.2A and 6.2B and their differences are more pronounced at the higher temperatures.

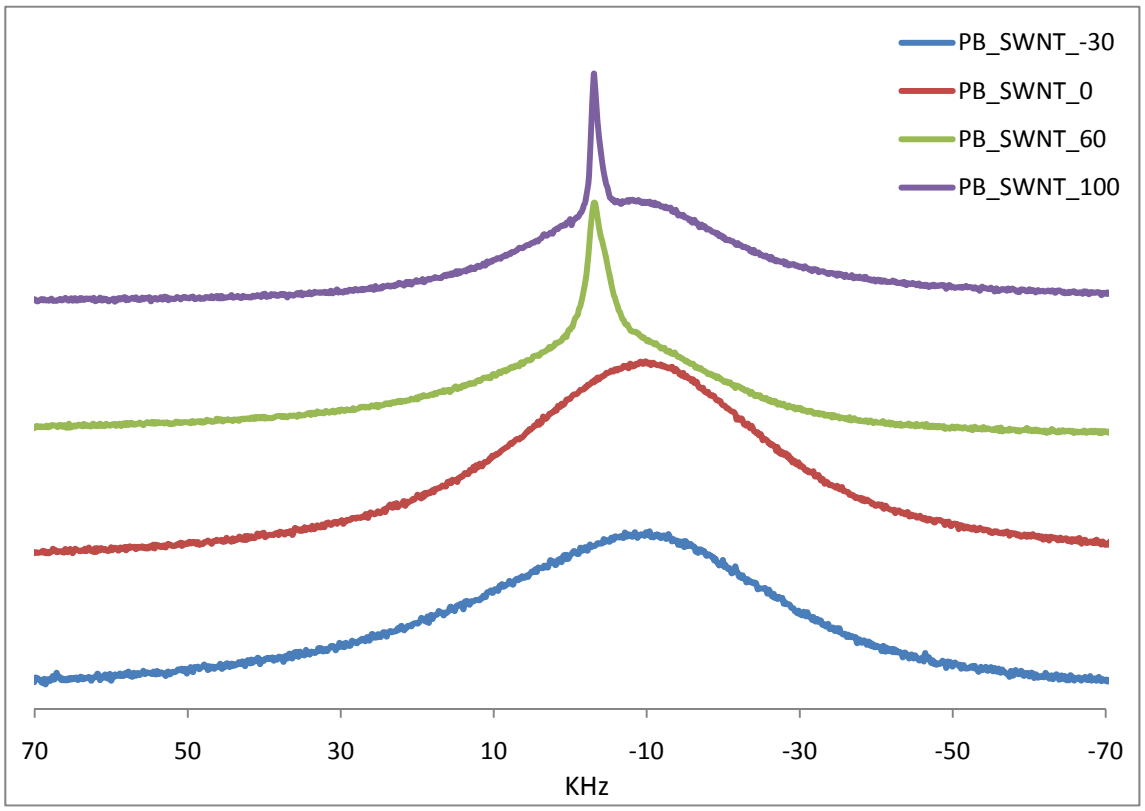

Figure 6.2A. Spectra for PB with SWNT and plotted at several temperatures.

The distinct CH and CH_2 sites are overshadowed by broadening as carbon nanotubes are added. In figure 6.2B, the emergence of a secondary peak with an increase in temperature is attributed to motional narrowing even though the nanotubes add to the overall broadening as compared to the base polymer sample. The PB SWNT CH peak is not suppressed by the addition of the nanotubes where as in figure 6.2B, PB with FSWNT does not exhibit a motionally narrowed CH peak at elevated temperature.

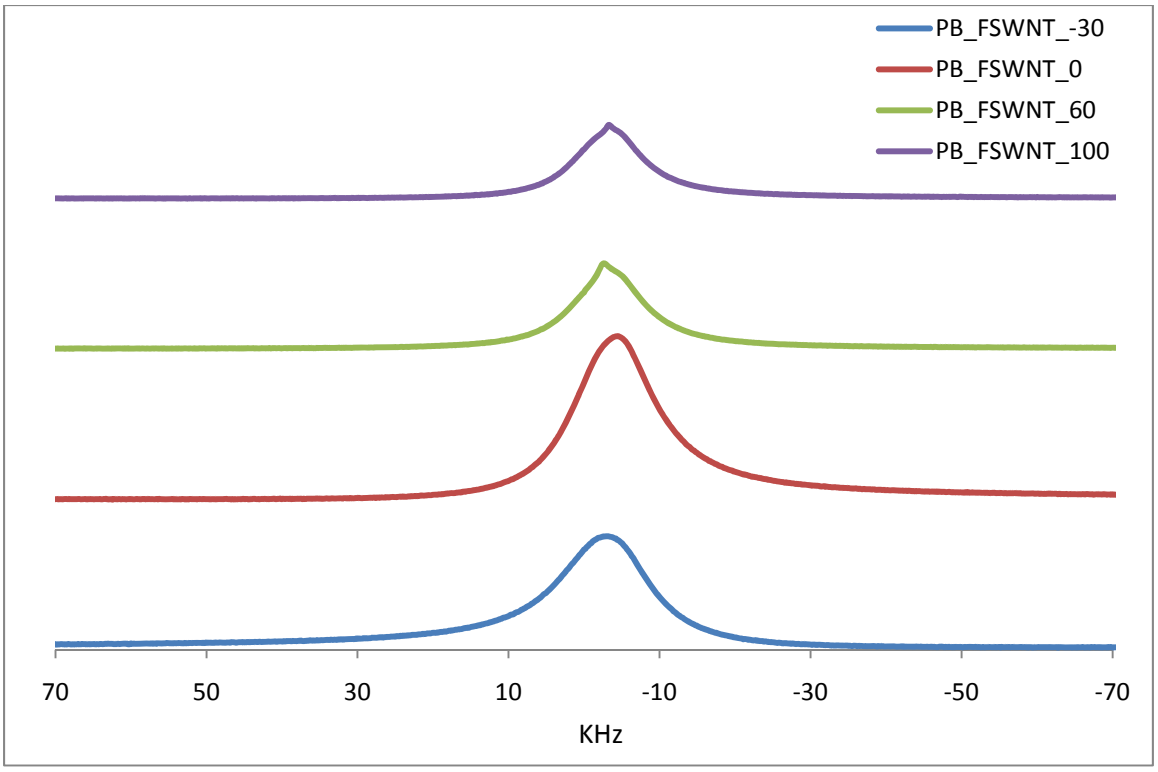

Figure 6.2B. PB with fluorinated SWNT spectra plotted as a function of temperature

The overall line widths of the pristine polymer and PB_SWNT and FSWNT composites are plotted in figure 6.3. In addition to the broader line width of the composites, the transitional changes between -20^0C and -10^0C in the pristine polymer are eliminated. The FSWNT composite also demonstrated a significant increase in overall line width but less than that of the SWNT composite, not counting the narrowed CH peak in the latter. The addition of the both kinds of SWNT causes a significant stiffening of the PB polymer as judged by the increase in line widths attributed to suppression of polymer segmental motion.

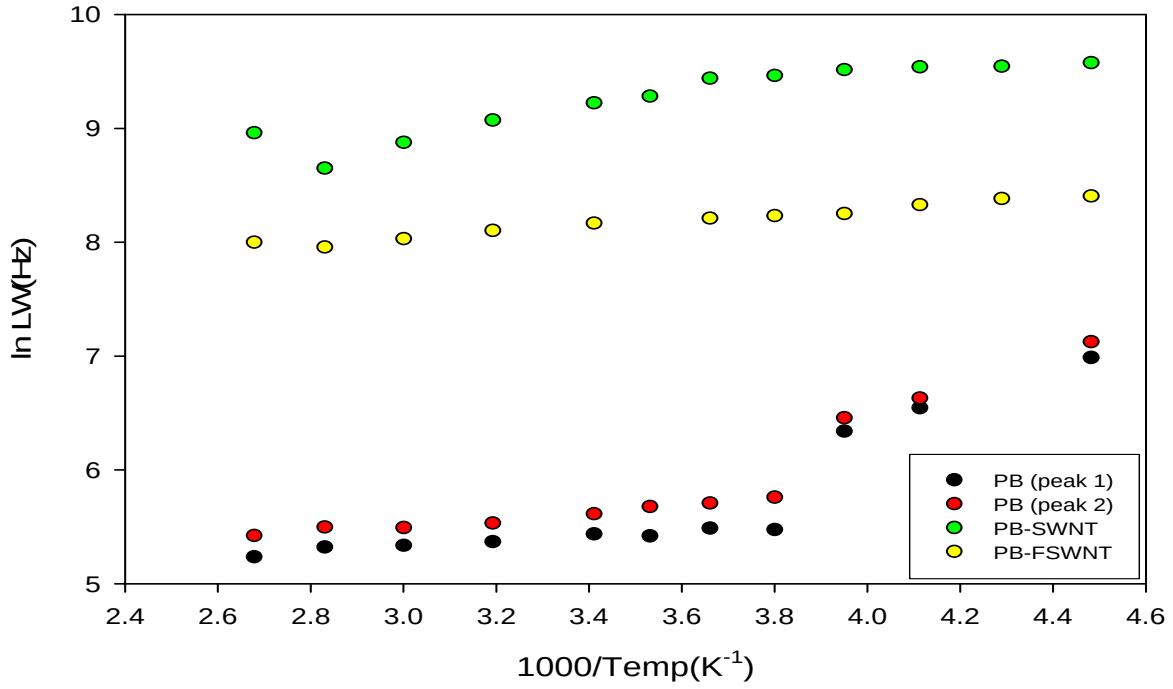

Figure 6.3. ^{1}H Linewidths of PB, PB+SWNT and PB+FSWNT as a function of temperature. The temperature increases from right to left and the data is plot ted as an Arrhenius curve

The spin lattice relaxation time, T_1, for the pristine polymer and the two composites is plotted in figure 6.4.

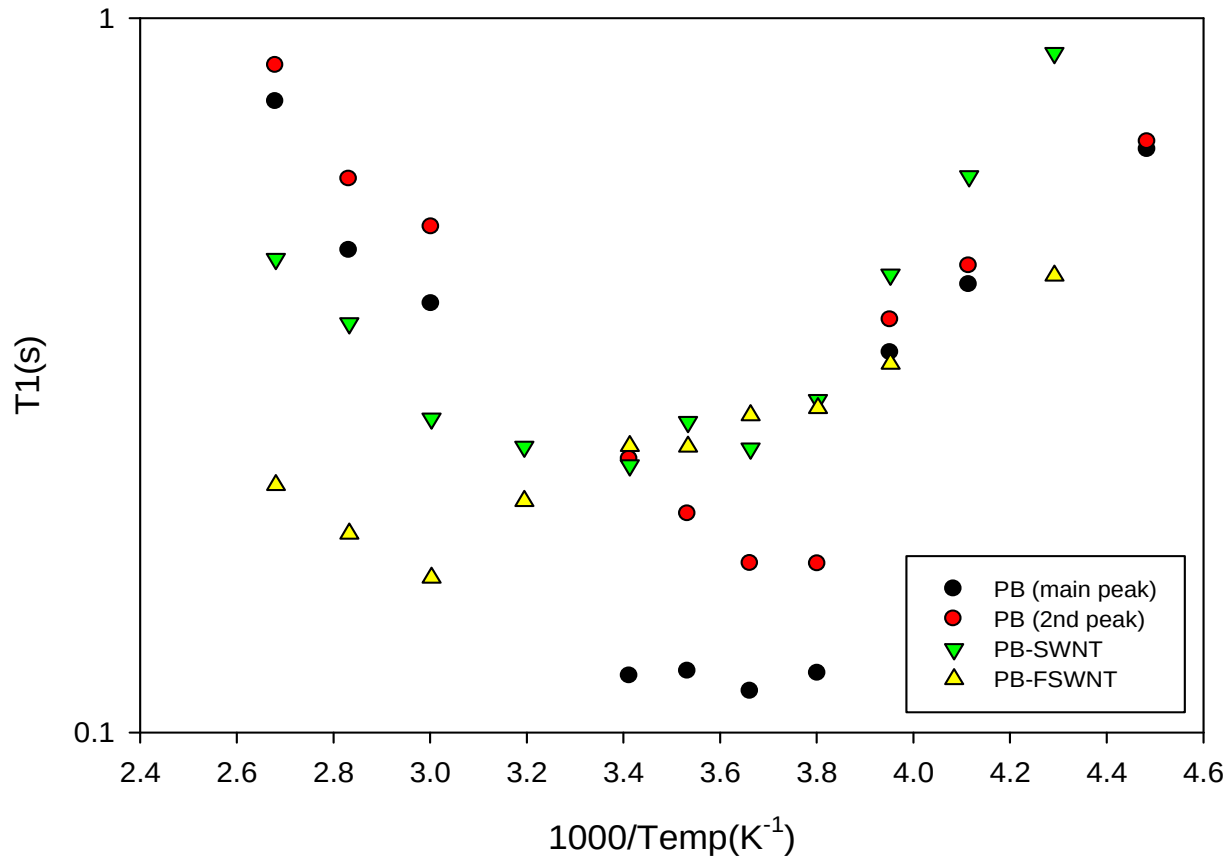

Figure 6. 4. Spin lattice interaction for PB, PB with SWNT and PBD with FSWNT. PBD exhibits a broad T_1 minimum.

For the pure polymer, both proton resonances exhibit T_1 minima. Despite the fact that adding SWNT causes more structural rigidity as evidenced by the line width increase described previously, the temperature at which the T_1 minimum occurs in the SWNT complex is not much higher than that of the pure polymer, indicating that the local segmental dynamics (i.e. sub-nm units with a corresponding timescale of ~ 1 – 100 ns) are only slightly affected by SWNT inclusion. However fluorinated SWNT does cause a significant change in the local structural environment and thus shifts the minimum towards a higher temperature.

Figure 6.5, below, show the spectra of PIB without nanotubes at various temperatures. There is distinctive motional narrowing with the increase of temperature.

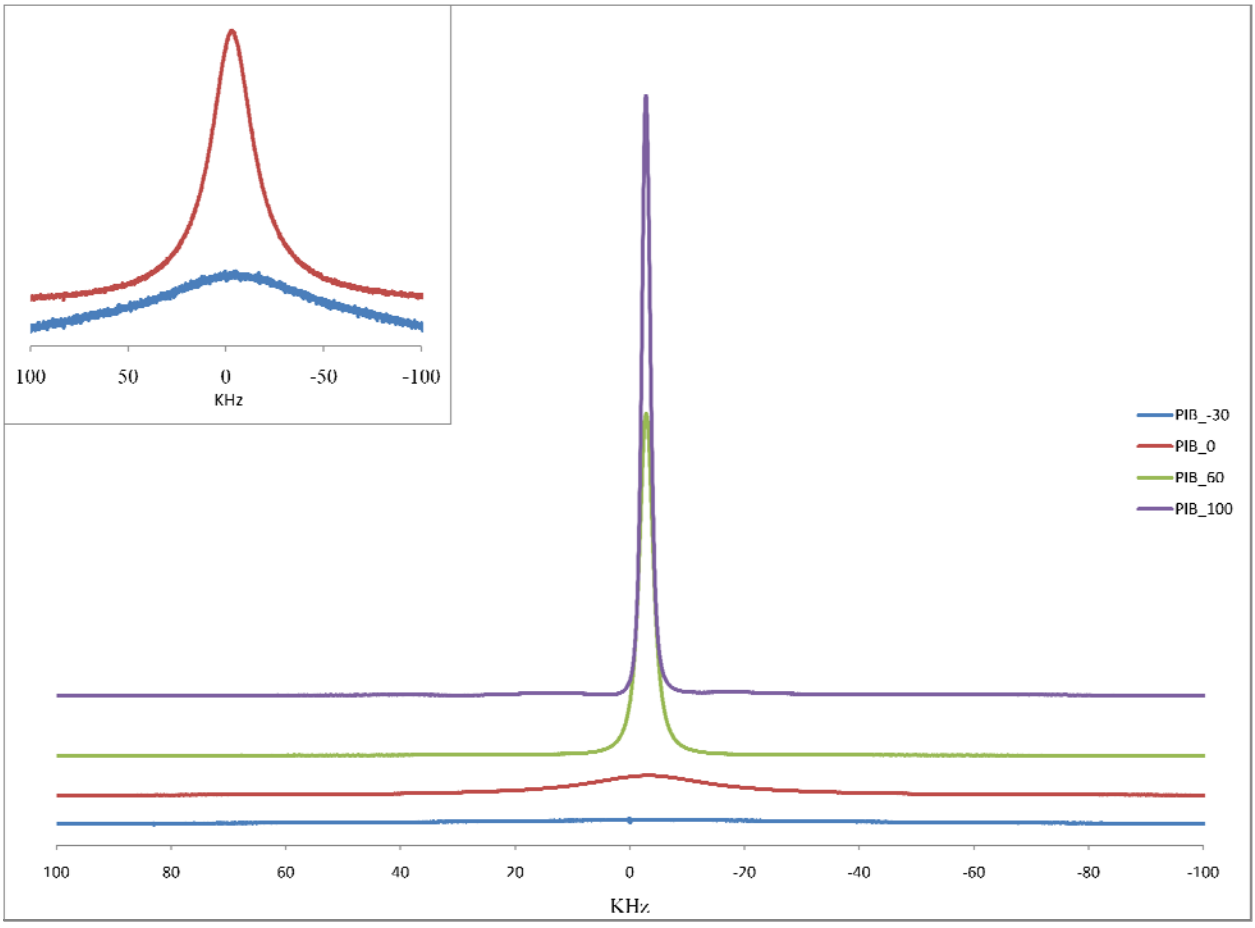

Figure 6.5. PIB variable temperature spectra profile

As observed in the case of PB, the addition of even small amounts of nanotubes to a polymer system can change the mechanical properties. This effect is confirmed in the NMR PIB_SWNT spectra line broadening as seen in figure 6.6. The broadening again is attributed to restricted

segmental motion. The composite exhibits an emergence of a secondary proton peak with an increase in temperature. This peak is assigned to the methyl hydrogen [12], [13]. It is clear that the addition of SWNT while inhibiting segmental motion does not suppress the CH_3 rotation. Fluorinated PIB does not change the basic profile of the polymer when compared to PIB_SWNT as seen in Figures 6.6 and 6.7 nor does it suppress the methyl peak. Figures 6.6 and 6.7 show linewidth narrowing with increasing temperature for both PIB_SWNT and PIB_FSWNT.

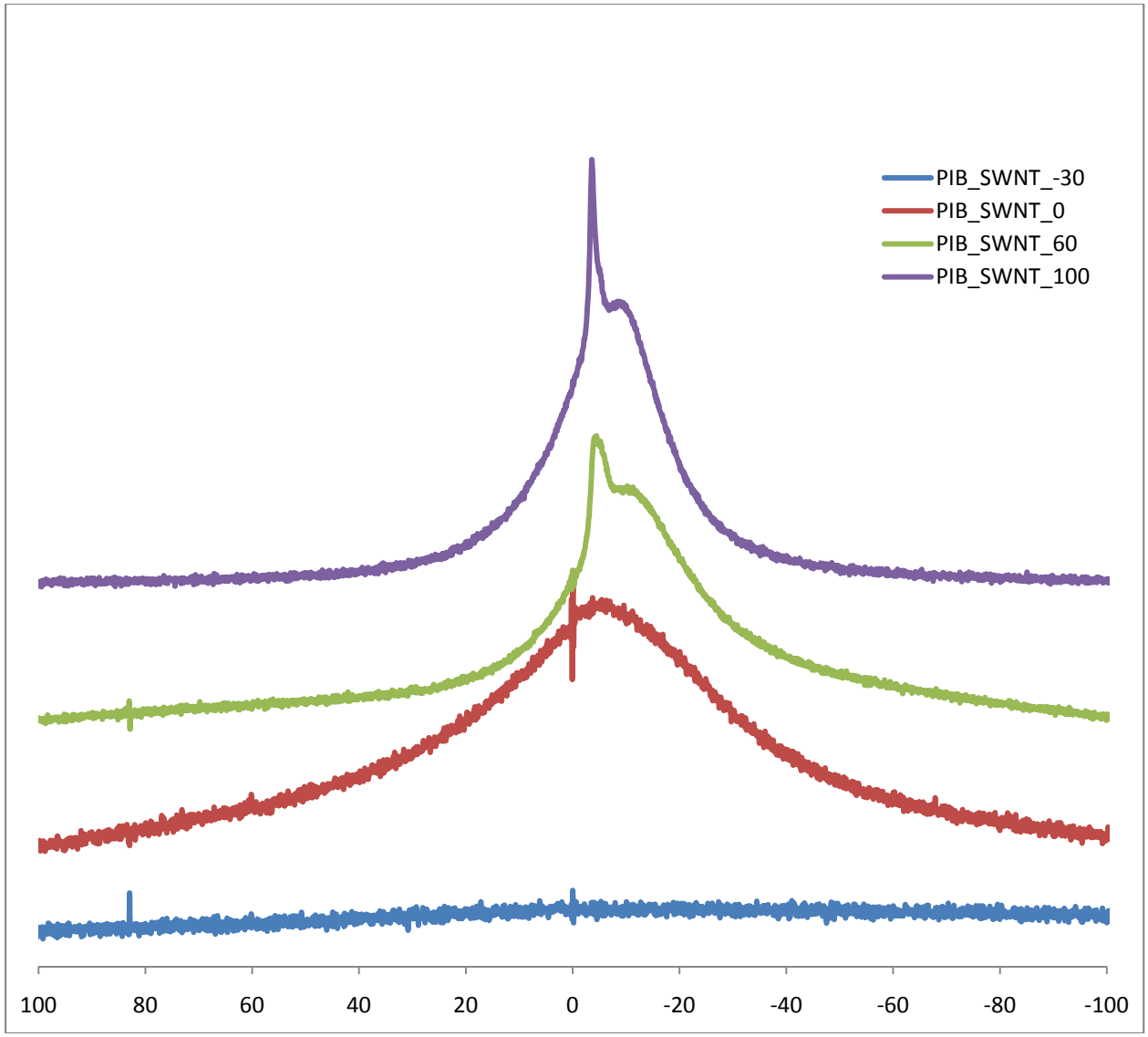

Figure 6.6. PIB SWNT spectra with the emergence of a secondary peak and motional narrowing at higher temperatures.

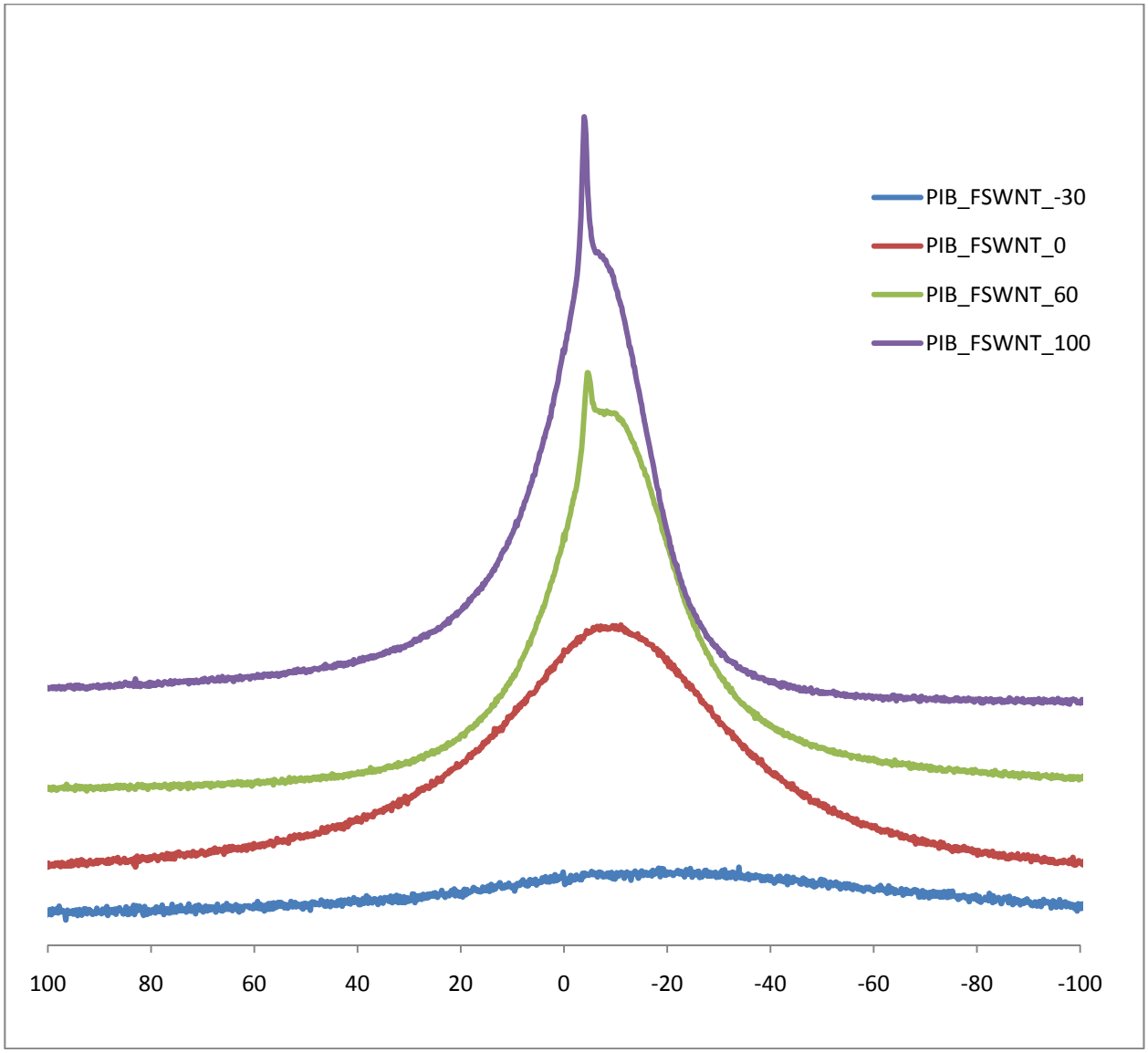

Figure 6.7. PIB with FSWNT proton peak plotted as a function of temperature and linewidth.

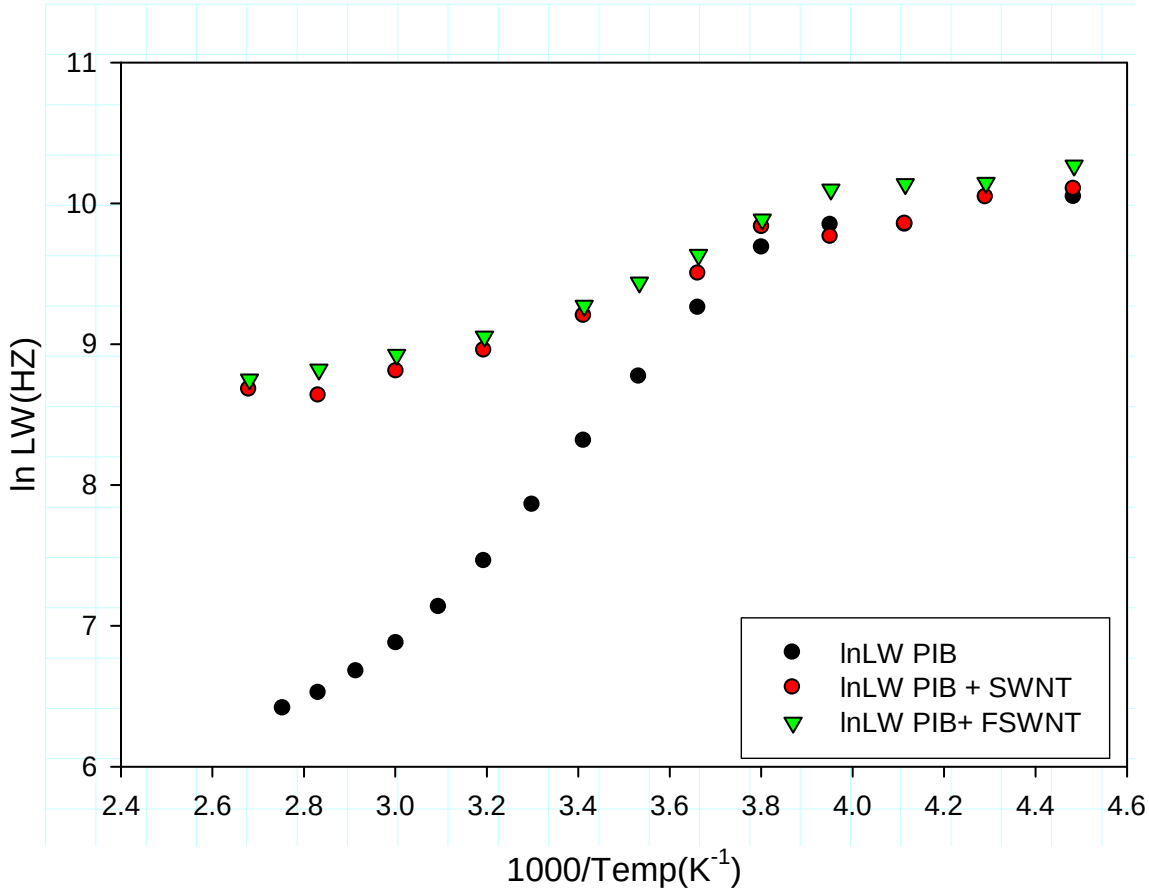

Figure 6.8. Temperature sweep comparative study for ^{1}H linewidth of PIB with SWNT and FSWNT.

The PIB linewidth begins narrowing between $-10^{0}C$ and $0^{0}C$. Adding SWNT does not change the general spectral shape below $-10^{0}C$. However the extent of motional narrowing at elevated temperature is much more modest. We can directly compare the PIB-SWNT and PIB-FSWNT. We note that the linewidths throughout the temperature range are almost identical.

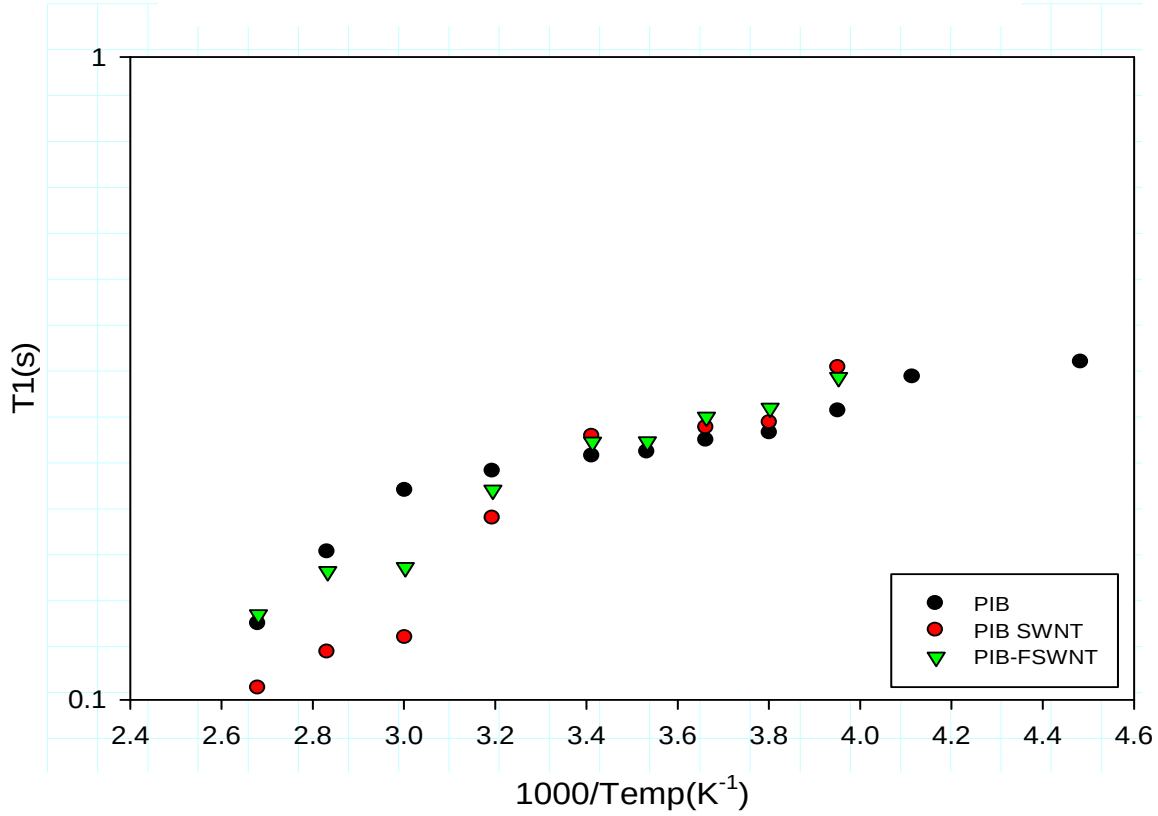

Figure 6.9. Semi-log plot of spin-lattice interaction for PIB, PIB with SWNT and PIB with FSWNT.

The T_1 comparison in figure 6.9 is reflective of short range motion and is remarkably insensitive to the addition of SWNT and FSWNT.

6.4 Conclusion

The addition of both SWNT and FSWNT to the polymers PB and PIB results in hindering segmental motion on the timescale probed by NMR linewidth measurements, from ~ 10^{-4} to 10^{-2} s. For the case of PB, SWNT inclusion gives a greater overall line broadening effect than FSWNT, but some localized motion does become activated at elevated temperature. This process does not appear in the PB/FSWNT composite. Faster dynamical processes probed by T_1

measurements are also affected by NT inclusion, as evidenced by shifting of the T_1 minimum to higher temperature. This effect is significantly greater in for the PB/FSWNT composite.

Line broadening also occurs upon inclusion of both SWNT and FSWNT in PIB, but there are qualitative differences between the PIB and PB results. There is essentially the same broadening for both SWNT and FSWNT and almost no effect of NT inclusion on short-range (or short-time) dynamics probed by T_1 measurements.

[1] P.J. Harris "Carbon Nanotubes and Related Structures" Cambridge University Press, 1999

[2] Q. Chen, R. Xu, and D. Yu, *Polymer*, 47, 2006

[3] S. Kumar, *Polymer/ Carbon Nanotube Composites: Challenges and Opportunities*, Georgia Institute of Technology, 2004

[4] S..J. Frankland, A. Caglar, and D.W. Brenner, *Reinforcing Polymers with Carbon Nanotubes*, Foresight Nanotech Institute

[5] L. Peng, *European Polymer Journal*, 2005

[6] P.M. Ajayan, L.S. Schadler, C Giannaris, A. Rubio, *Advanced Materials*, 12, 2000

[7] M. L. Shofner, V. N. Khabasheskau, and E. N. Barrera, *Chemical Material*, 18 2006

[8] M. J. Connell,P. J. Boul, L. M. Ericson, C. B. Huffman, Y. Wang, E. Haroz, C. Kuper, J. M. Tour, K. Ausman, and R. E. Smalley, *Chemical Physics Letters*. 2001

[9] J. Zhu, J.D. Kim, H. Peng, J.L.Margrave, V.N. Khabashesku, E.V.Barrera, *Nano Letters*, 3, 2003

[10] H.Geng, R. Rosen, B. Zheng, H. Shimoda, L.Fleming, J. Liu, O. Zhou, "*AdVance. Materials*.14, 2002

[11] M. L. Shofner, V. N. Khabasheskau, E.N. Barrera, *Chemical Material*, 18, 2006

Chapter 7 Asymmetric Hybrid Electrochemical Energy Cell

7.1 Introduction

The need for compact, portable and interchangeable energy delivery system has been growing rapidly for the last two decades. The most evident need has been for devices that can produce sustainable energy output over an extended period of time. In addition there has been a desire from several industry sources for a device that can store and deliver a large amount of energy in a short time interval. The devices that have been created and that match the former and the latter needs are the Electrochemical Double Layer Capacitor (EDLC) and a lithium-ion battery respectively [1]. As mentioned in an earlier chapter, batteries have high energy densities and EDLCs have high power densities. An EDLC as seen the figure 7.1 below

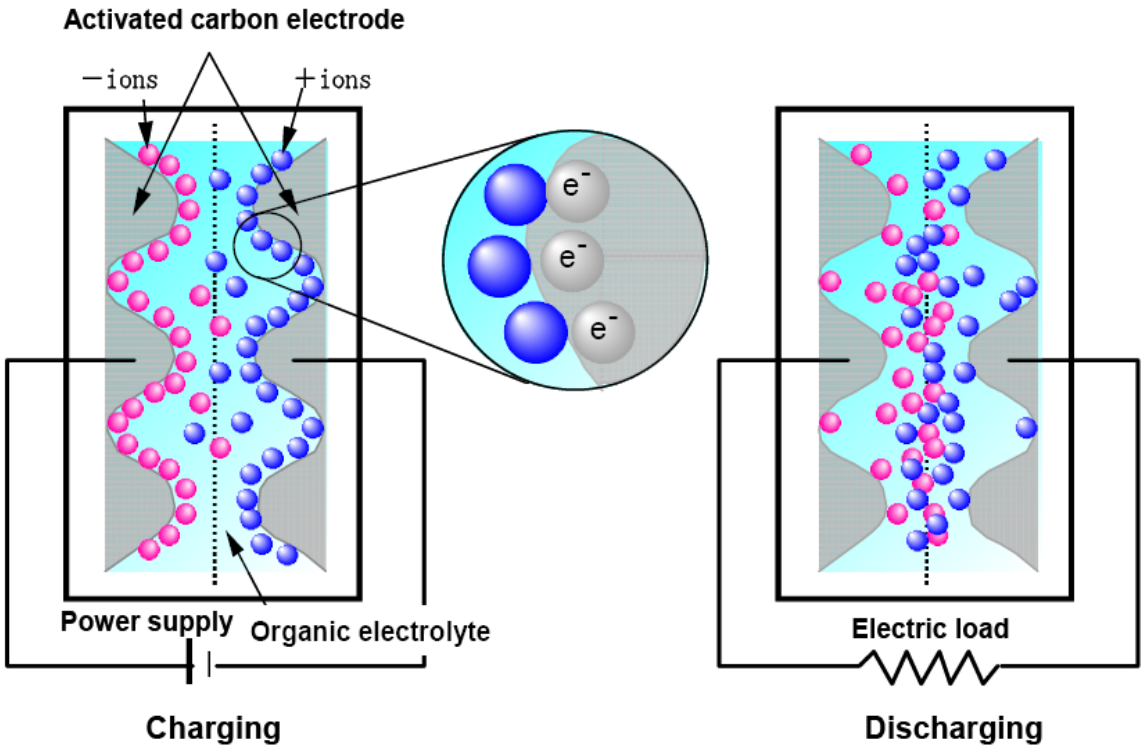

Figure 7.1.Schematic of a supercapacitor with activated carbon and ions during the charging and discharging process with a highlight of the charge particles at the carbon interface.

is made of porous high surface area activated carbon electrodes with an organic electrolyte separating the two carbon electrode layers. The two electrodes are separated by a membrane which is ion permeable. The separator is the porous membrane soaked with electrolyte denoted by the dashed lines in the above figure 7.1. This construction of the EDLC allows for greater surface area which in turn gives rise to more stored charges. Upon the commencement of charging a Helmholtz double layer is formed [2]. The electrolyte can be aqueous or non-aqueous. The choice of a non-aqueous electrolyte separator facilitates a higher voltage operation ranging from 0 to 2.75V [3].

The difference between a conventional electrostatic capacitor (ESC) and an EDLC is substantial. A conventional ESC has two conducting plates of area A separated by a distance *d*, with a dielectric material between the plates. The capacitance is given by the basic equation

$$C = \frac{\varepsilon A}{d} \tag{7.1}$$

where ε is the dielectric constant. EDLC are non-faradaic devices. Faradaic devices utilize oxidation/reduction process which involves the transfer of charge. This can occur between the electrolyte and an electrode. Conversely a non-faradaic process involves no chemical bond breaking or bond creating. It is purely a physical process. An EDLC has two capacitor surfaces. Each electrode, as seen in figure 7.1 develops a capacitive surface, thus the double layer. It can be thought of as two capacitors in series with an internal resistance. In addition the surface areas of an EDLC due to the porous carbon are orders of magnitude greater than ESCs. The energy storage of an EDLC exceeds that of a conventional ESC by one to two orders of magnitude. In addition proper choice of constituent materials that operate at higher voltage can also increase

the energy storage and the power. This can be related by the power and energy relations associated with the device. Both the power and energy directly vary as the square of the voltage.

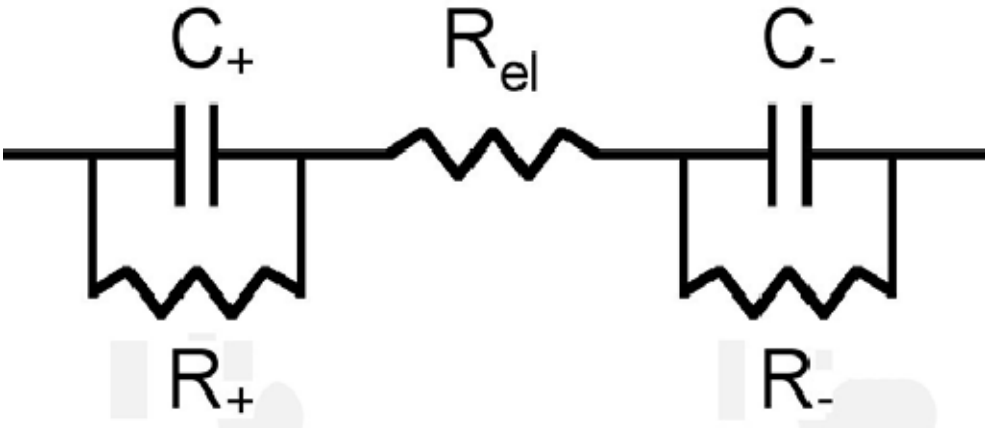

Figure 7.2 An equivalent circuit for an EDLC where R_{el} is the electrolyte resistance, R_+ and R_- are leakage resistance and C_+ and C_- are the capacitance at each node of the EDLC [4].

In the aforementioned equations E is energy stored, P is power, V volts, R the equivalent series resistance, as seen in figure 7.2, and C is capacitance [4]. The choice of the electrode material in the design of the EDLC is also important. Porous activated carbon has been the premier choice due to its high surface area, its manufacturing familiarity, and its low cost. The increased surface area is associated with the micro pores. Typically the increase surface area ranges from 1000 to 2000 m^2/g and leads to significant capacitance gain which generally is above106 F/kg [4]. Cycle life of these cells is critical. Typically the range of EDLCs is 5×10^4 to 1×10^6 cycles.

There are several type of non-aqueous solvents that can be used in the electrolyte. Traditionally in Li-ion battery technology ethylene carbonate (EC), di-ethyl carbonate (DEC)

and di-methyl carbonate (DMC) have had extensive use. Early EDLCs used these solvents. Since then, acetonitrile, CH_3CN, has become a premier choice. Acetonitrile solvent in EDLCs has shown better performance because of its low viscosity which leads to high conductivity, in turn leading to lower internal resistance. It also has higher working voltage and higher electrochemical stability. It has been shown that systems using acetonitrile have had better power performance [5]. In addition they operate at a wide temperature range. In spite of the improvements in the construction of EDLC the overall power density is much less (<10%) than that of Li-ion battery. This would make them not suitable enough for a wide range of applications. A combination of the best assets of a Li-ion battery and an EDLC would enhance its performance and make it suitable for a wide variety of commercial use.

A hybrid non-aqueous device that could increase the energy density without significantly sacrificing power density, and extend the cycle life would be a significant improvement. An asymmetric hybrid non-aqueous energy storage cell (AESC) is a combination of the EDLC and an ion battery. In this hybrid the positive electrode is like that of an EDLC. This allows it to be more robust while increasing its speed of power delivery and density. The negative electrode is similar to that of a battery giving it an energy density 400% greater than that of most types of EDLC. Hybrids such as these, as seen in figure , utilize non-faradaic and faradaic means to move and store charge

Figure 7.3 depicts an example of a particular type of AESC. The reasoning behind the selection of the negative electrode is to improve the operating voltage and maximize the energy density [6].

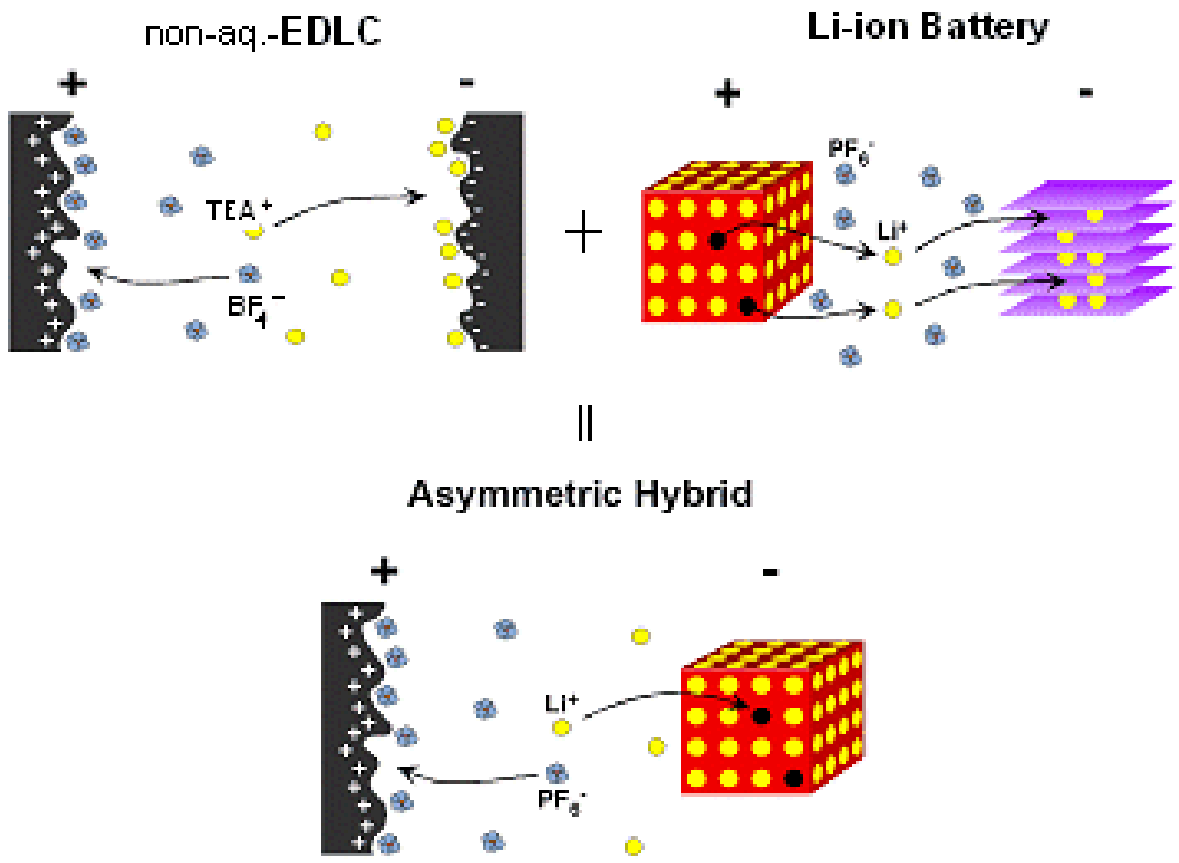

Figure 7.3. An illustration of the formation of an asymmetric hybrid non-aqueous electrochemical double layer supercapacitor [11].

This concept was first developed by Telecordia Technologies. The AESC still possesses the rapid discharge and charging process of the EDLC while maintaining a very long charge life without much loss. A hybrid cell like this can have a charge rate of up to 10C versus that of 2C for a Li ion battery. In addition to the aforementioned it has much higher energy density, which is typically 3 to 8 times more than that of the EDLC. These hybrid cells have an activated double layer carbon positive electrode and a high energy density negative electrode. The negative electrode needs to intercalate ions while minimizing expansion and contraction of the lattice during intercalation and de-intercalation process. The material that so far has best met these challenges has been nano-structured $Li_4Ti_5O_{12}$, used for negative electrode. $Li_4Ti_5O_{12}$

appears to have a two phase intercalation format which leads to flat voltage plateau. The flat plateau mitigates the steep linear non-faradaic profile of the positive activate carbon electrode. The 1.5 V lithium insertion (Li/Li^+) voltage is low enough versus the 3 to 4 volts (Li/Li^+) non-faradaic positive electrode for the energy density to remain high [7]- [11].

7.2 Experimental

The wet and dry AESCs were fabricated at the Rutgers University Energy Storage research facility by Prof. Amatucci's group. Powdered ASupra (AS) was dried 3 hours at a temperature of 110℃ and overnight under vacuum at 120℃. Polyvinylidene Difluoride **(**PVDF) (Kynar 2801) and a lithium titanate tape (70% active LTO) were dried 3 hours at 120℃. In the glove box, 10% Kynar 2801 was mixed with AS. A swagelok cell, as seen figure 7.4 below, was made using a matching ratio 4:1 (AS vs. LTO). Extreme care was undertaken to construct the swagelok cell so that powder would not contaminate the sides and give rise to an electrical shorts. The LTO tape was placed, then 2 glass separators, then Celgard separator with the powder on top.

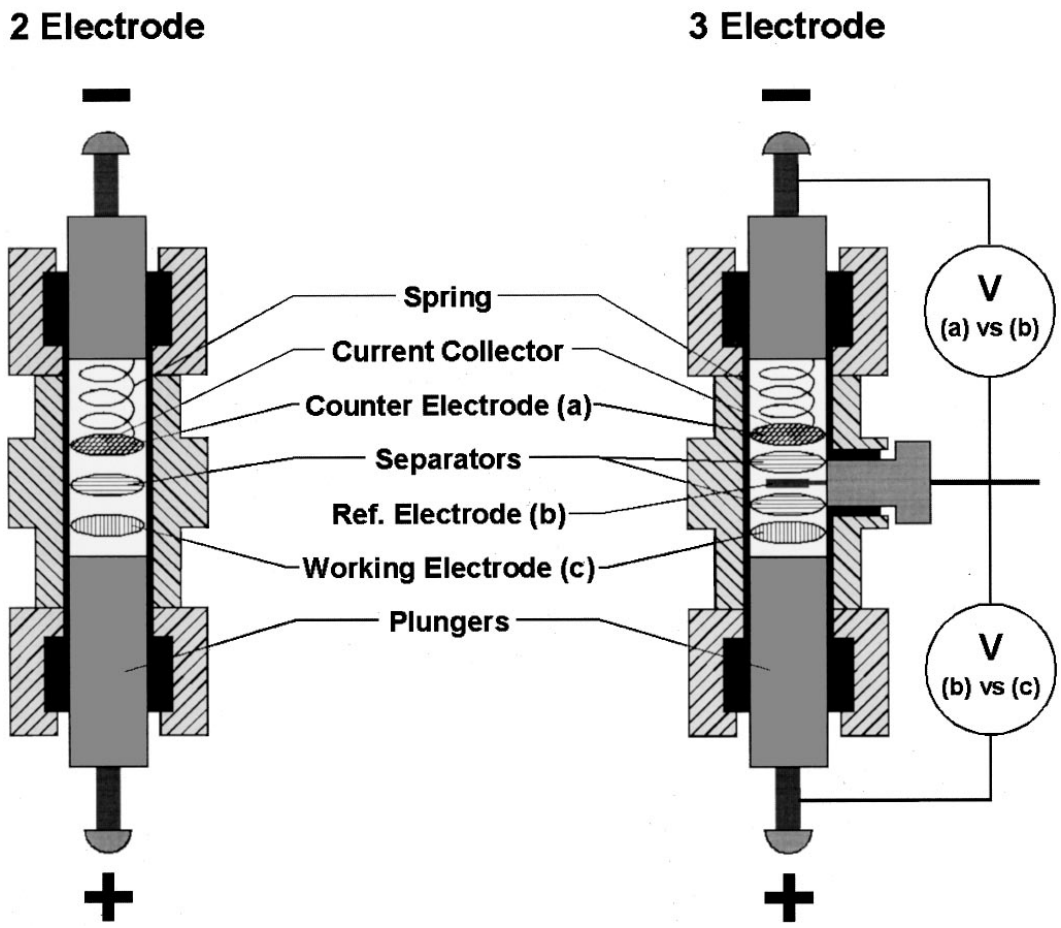

Figure 7.4. A diagram of a two and three electrode Teflon Swagelok hybrid cell [1].

The assembly was closed and turned over, the top removed and a stainless steel disk was put on. The electrolyte was added to cover the disk, the spring was added and the swagelok was tightly closed. The electrolytes were prepared by mixing approximately1.3 ml labeled solvent: acetonitrile-1-^{13}C (Aldrich), or acetonitrile-2-^{13}C (Aldrich) with 2.6 ml of 2M $LiBF_4$ in acetonitrile (Ferro). 0.2 micro liters of de-ionized water was added to 1 ml aliquots of each electrolyte mixture to make a 200 ppm water concentration. It is important to note that even the dry sample has trace amount of water but the wet samples have more. Since this was such a small addition of water, a Karl Fischer titration was performed on a similar solution of standard electrolyte. The water concentration was determined to be approximately 100 ppm. The cells

were charged to 3.1 volts in a dry room (<3% RH) and held at constant voltage for two weeks. The Swagelok hybrid cells were then disassembled in the glove box and the powder recovered for testing. There was no additional treatment such as rinsing of the powder.

All NMR experiments were performed on the Chemagnetics NMR System and a 7.1 Tesla magnet. The measurements for ^{13}C, ^{1}H, and ^{7}Li were executed with a MAS 3.2mm probe. Each test was done with the sample at 293K. Excitation of the target nucleus, ^{13}C, was performed via direct excitation using a 90^0 pulse with a pulse width of 3.3μs and spectral window of 100 Khz. In addition to direct excitation ^{13}C cross-polarization combined with MAS was used. The time domain FID was then transformed by Fourier analysis, which produces the associated spectrum. The proton NMR spectra were acquired by direct excitation with a 90^0 pulse of 1.75 μs width and a relaxation delay of 5 seconds with the Hartman-Hahn contact time of 6000 μs. The power levels of the observed cp (tpwrm) was 53 and decouple power (dpwrm) was also 53.

7.3 Results and Discussion

Each sample for ^{13}C was prepared and divided into lots of wet and dry for the nitrile enriched carbon as well as the methyl-enriched carbon. Cross Polarization in conjunction Magic Angle Spinning, CP/MAS, was the method used to gain enhanced spectra of the ^{13}C. The spinning motion of MAS leads to narrowing of the spectral lines by averaging out the anisotropic effects as discussed in the pulse techniques section of this document. Proton decoupling was applied during the acquisition of the FID which removes line broadenings due to dipolar couplings associated with the protons.

The addition of 200 ppm of water is believed to affect the chemistry and pathways of anodic decomposition in the Asymmetric Hybrid Supercapacitor samples by influencing the type and extent of the electrolytic breakdown products. As seen in the previous study as well as this investigation $HOCH_2CN$ (glycolonitrile) and CH_3CONH_2 are the two principal solvent decomposition products. These two will be further discussed and identified in the body of this paper. The peaks identified were observed by deconvoluting the NMR spectra. As expected the deliberately added 200 ppm of H_2O causes additional breakdown of acetonitrile, by hydrolysis and oxidation. This can be seen in the multiplicity of peaks in figures 7.5 and 7.6. The NMR spectra compare the wet and the nominally dry sample, labeled dry, of the methyl and cyano ^{13}C enriched acetonitrile.

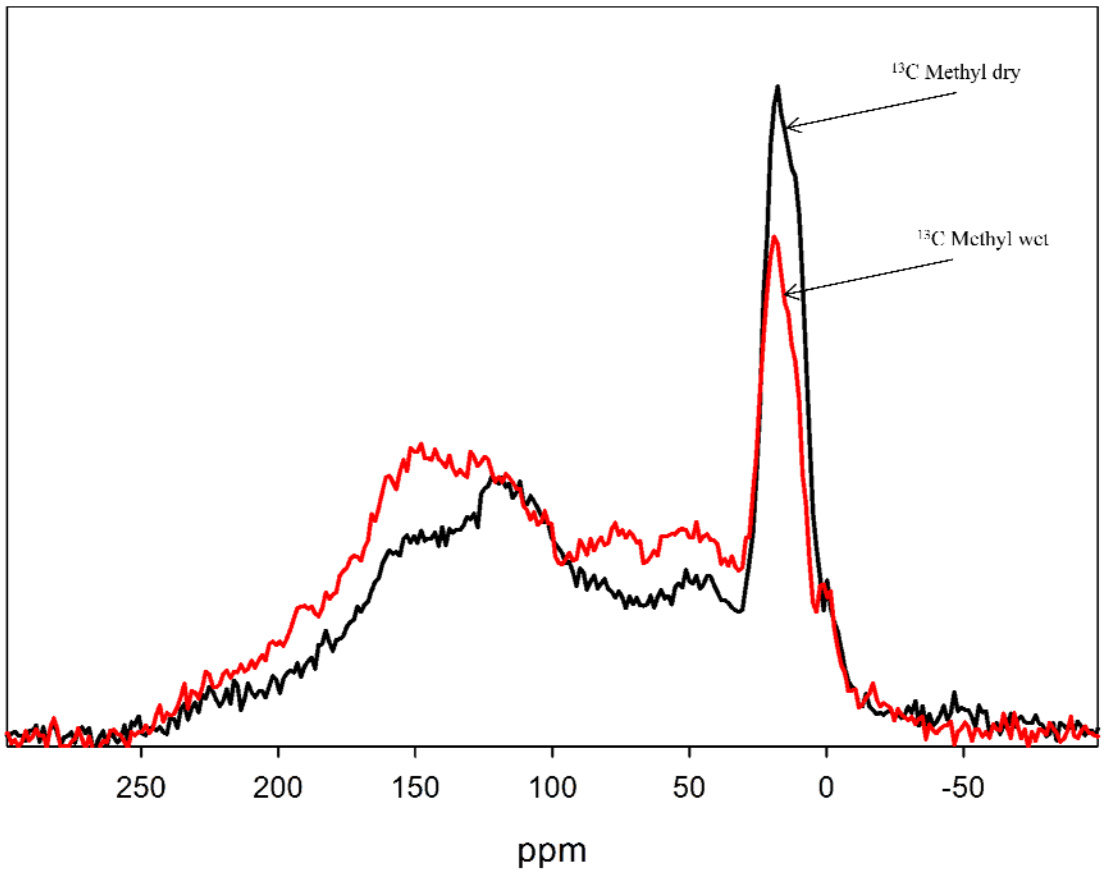

Figure 7.5. ^{13}C enriched CP/MAS proton decoupled spectrum for acetonitrile wet and dry samples. The spectra are compared for changes between wet and dry.

The first sample analyzed was the wet methyl enriched ^{13}C. The ^{13}C CP/MAS wet full spectrum, as seen above, is a result of peaks ranging from -1.1 ppm to 176 ppm. Compared to direct detection the CP/MAS experiment enhanced all peaks associated with protons directly bonded to the enriched methyl carbon of acetonitrile and its breakdown products. The four peaks, at δ = -1.1 ppm, 1.5 ppm, 16 ppm and 39 ppm, are within the region of the alkyl group. This group includes CH, CH_2 and CH_3. The signal at 16 ppm has been identified as the methyl carbon in acetamide, CH_3CONH_2 and δ = 1.5 ppm is the acetonitrile methyl carbon which is close to the expected 1.1 ppm peak in the literature for acetonitrile. The -1.1 ppm peak could be a match for

the compound of CH_2CNLi which is located at -1.9 ppm. Thus both aforementioned compounds are indicated to be present and provide an excellent correlation with literature and projected peaks. Acetamide ^{13}C peaks, in the literature, have been identified at approximately 22 ppm and 172 ppm which is consistent with the observed data in this study. The substantial ^{13}C methyl acetamide peak for the wet sample is center is centered at 16 ppm. This is well within the range of the cited data and correlates well with the cyano carbon of the same breakdown product located at 168 ppm discussed later thus further affirming the identification of acetamide. Also in figure 4 is the spectrum for the nominally dry methyl enriched ^{13}C sample. The main large carbon peak of the nominally dry methyl sample is centered at 18 ppm which is also assigned to acetamide but the small shift between wet and dry is not presently understood. The peak at δ = -0.3 ppm is the enriched ^{13}C of acetonitrile. The wet sample peak located at 16 ppm, is reduced in total area as compared to the dry sample.

The reduction of the wet sample peak area is due to the breakdown of CH_3CN leading to the formation of other breakdown products at 54 ppm and 75 ppm as well as potentially others. In this investigation as well as the previous study the peak at 54 ppm has been identified as $HOCH_2CN$, glycolonitrile, formed by the oxidation of acetonitrile. The methyl carbon, of glycolonitrile, is shifted by approximately 50 ppm due to the effect of the OH, and another of the potential breakdown products located at the 75 ppm peak is $CHCNH_2$, an alkyne. Due to the residual water in the sample anodic decomposition is enhanced and in addition it has been suggested that the glycolonitrile can be further reduced as follows [12], [13]:

$$HOCH_2CN \rightleftharpoons CH_2O + CN^- + H^+$$

The spectral signature that describes glycolonitrile, in the United States Patent for the *Process For Producing Glycolic Acid From Formaldehyde And Hydrogen Cyanide*, is

consistent with the observed data of the present study. In the aforementioned Dupont patent study the spectral signature for the CH_2 carbon of glycolonitrile occurs at 48 ppm and the nitrile ^{13}C is located at 119 ppm. This is consistent with a tested glycolonitrile sample. This test was performed using pure liquid glycolonitrile under similar sample experimental condition. The spectrum peaks were located at 49 ppm and 120 ppm. In addition to those carbon peaks the patent study definitively identified CH_2O, associated with glycolonitrile and its breakdown, ^{13}C peaks at 80-90 ppm. Figure 4 shows that ^{13}C peaks occur at 54 ppm and 126 ppm for the wet sample. These two peaks are consistent with the patent study spectrum (in figure 7.6) as well as with the pure glycolonitrile test under experimental conditions shown below in figure 7.7

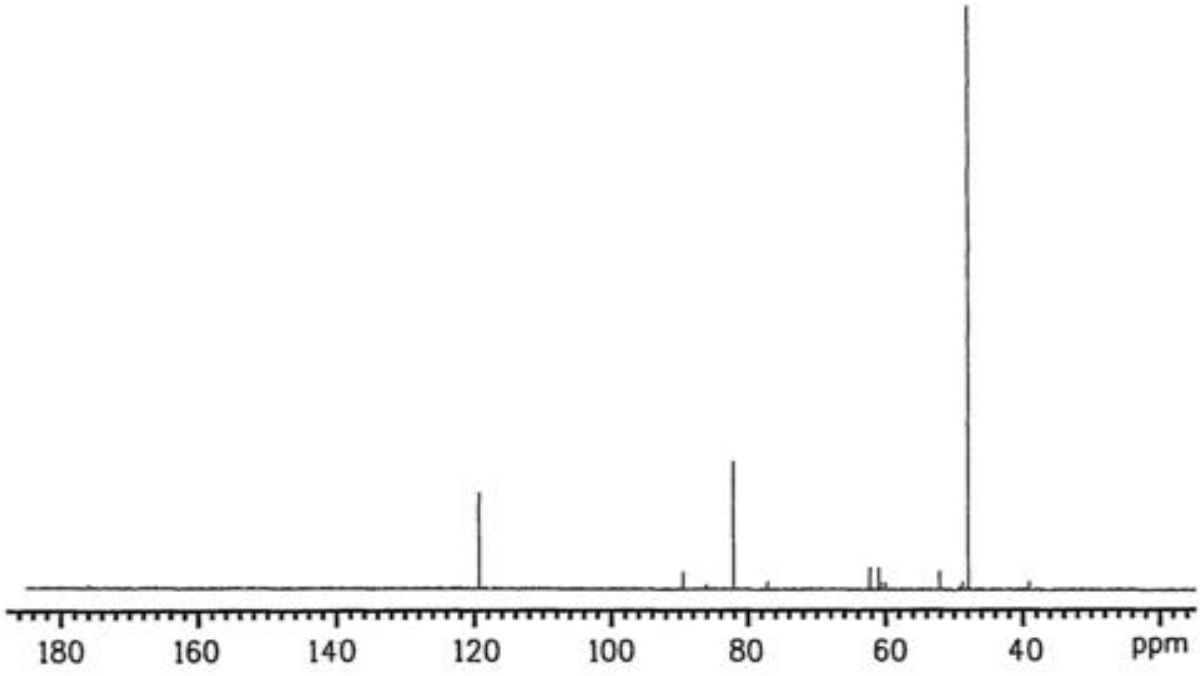

Figure 7.6 The Dupont ^{13}C NMR spectrum shows the major glycolonitrile ^{13}C resonances at about δ 48 and 119 ppm. There are also substantial resonances in the range of δ = 80 - 90 ppm for unreacted formaldehyde

The two spectra, figures 7.6 and 7.7 provide good correlation to indicate the match for ^{13}C in glycolonitrile as well as the progressive decomposition to formaldehyde and other formaldehyde

associated products which are indicated in figure 7.6 around 60 ppm. The Dupont study labeled them as by-product species derived from unreacted formaldehyde.

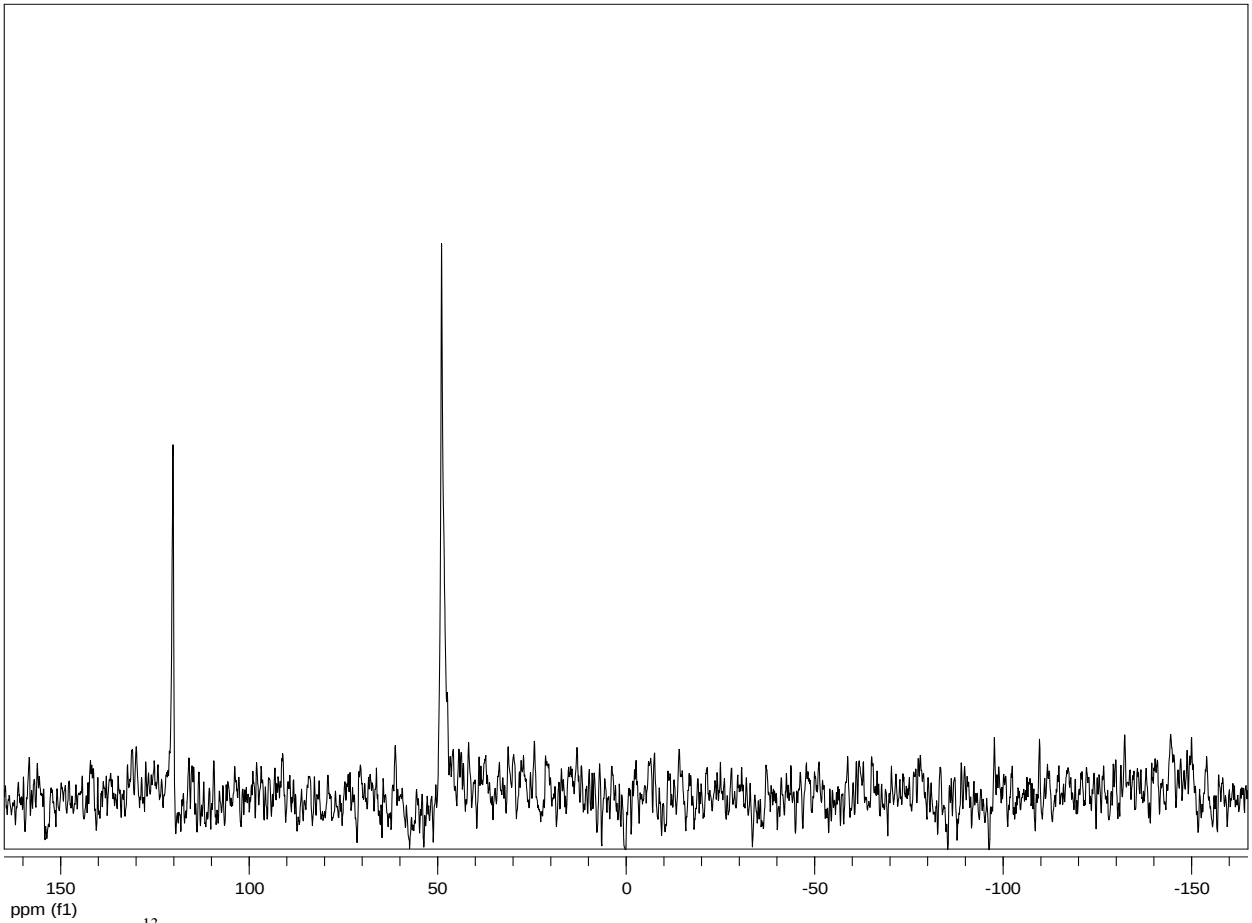

Figure 7.7 ^{13}C NMR spectrum of glycolonitrile with the nitrile peak at 120 ppm and the methyl peak at 49 ppm.

. The dry sample peaks are similarly consistent with the presence of one of the principal breakdown product. The associated peaks occurred at 54 and 127 ppm respectively. The CN^- of the glycolonitrile decomposition is available for bonding with the very reactive Li^+ to form LiCN which has been previously suggested as well as in this work as a potential breakdown product. Nitrogen enriched NMR studies which could have given further information were attempted unsuccessfully. The nitrile carbon of LiCN was projected to occur at 162 ppm and in figure 5 of the enriched nitrile carbon the actual peak is located at 168 ppm. This peak is believed to contain

the LiCN and CH_3CONH_2, a carboxylic carbon of an amide. Confirmation of the further reduction of glycolonitrile is seen in figure 5 of the nitrile enriched spectrum. This spectrum, again, compares the wet sample to the dry. We note in this NMR spectrum that there is a significant reduction of the region from 118 ppm to 146 ppm in the wet sample as compared with the dry sample. This is the region of the acetonitrile and the glycolonitrile. It is believed that the aforementioned change in turn leads to the enhanced peak at 168 ppm and a clear peak at 88 ppm. The enhanced peak at 168 ppm is potentially do to having more LiCN present and the 88 ppm peak falls within the region of CH_2O, formaldehyde which occurs between 80-90 ppm [13].

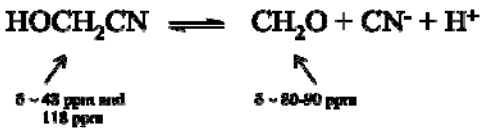

The methyl enriched ^{13}C also show enhancement of a peak centered at 75 ppm which was previously attributed to the alkyne alone. This peak is broad enough and does encompass the area in which CH_2O formaldehyde would be expected in an NMR spectrum. Both of these attributes would lend to suggestion that glycolonitrile may be an intermediate product and further break down with the additional of water in the deliberately water-added sample [12] –[15]. While pure formaldehyde (without any trace of water) can have a higher chemical shift, hydrated formaldehyde chemical shift is significantly lower and show a characteristic signal of a CH_2 group around 82 ppm [14].

Inspection of the methyl enriched carbon NMR peak (as seen in figure 7.5) shows an increase in peak height and area, of the wetter sample, ranging from approximately 40 to 90 ppm. This same effect is also evident from 125ppm to 220 ppm. These changes in peak height and integrated areas are consistent with the creation of additional breakdown linked to the

increase in water content. Confirming details are evident in (figure 7.8) the nitrile carbon enriched spectra from 148 to 190 ppm where the same type of peak increase takes place.

The carbon CP/MAS NMR spectra, below in figure 7.8, is from sample set number 2, wet and dry, for the enriched nitrile carbon. There are four peaks that constitute the main breakdown species of the wet sample spectrum. These peaks are located at 126 ppm, 137 ppm, 148 ppm and 168 ppm. Although some of the peak identity have been previously mentioned they are as follows: The ^{13}C peak at 126 ppm is that of the enriched nitrile carbon of CH_3CN, the peak located at 148 ppm is consistent with the CH_2CNLi (aminoacetylene) breakdown product, and the peak at 168 ppm is acetamide. Identification of these compounds by enrichment of both carbons lends confidence to these assignments. These results are conclusively consistent with the previous study of enriched acetonitrile in the asymmetric hybrid supercapacitor. The peak 133 ppm is yet to be identified. The dry sample has a similar peak identity but the difference with the wet sample lies in the breakdown product distribution. The clear peaks are at 127 ppm, 145 ppm

and 166 ppm.

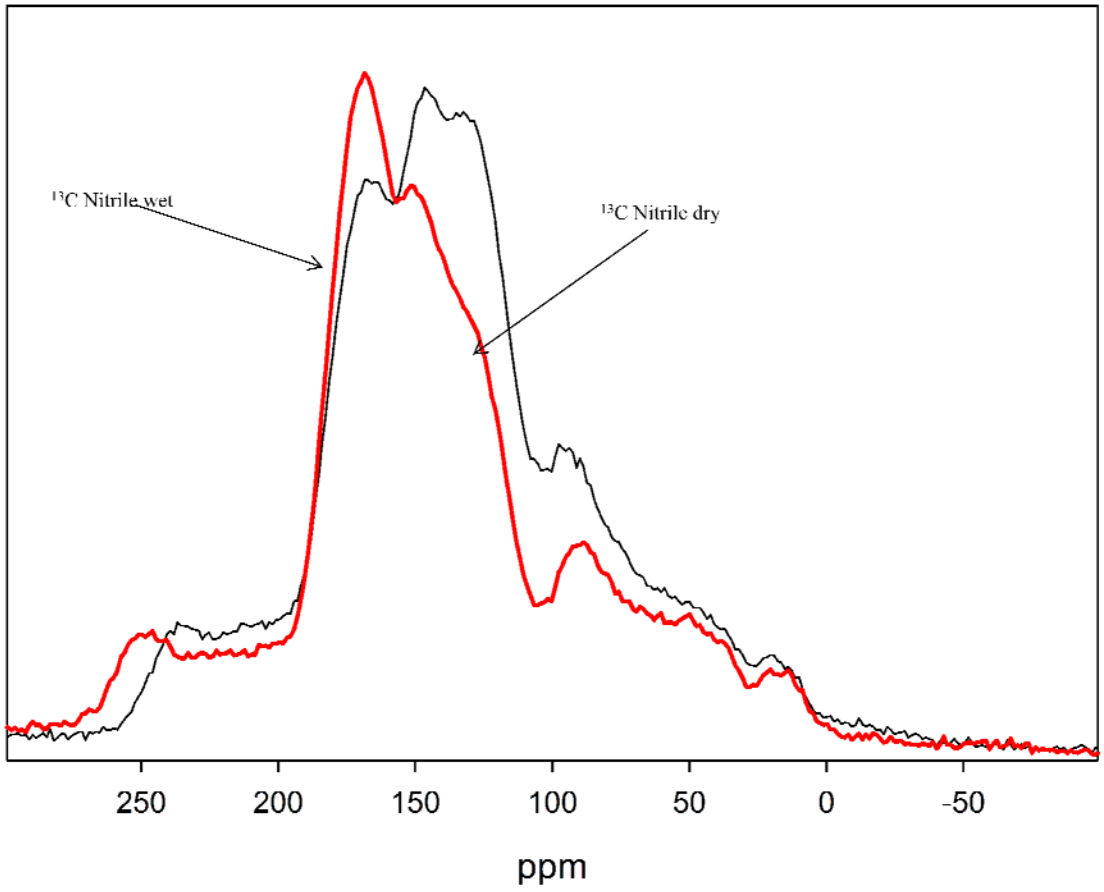

Figure 7.8. The above spectra are the nitrile enriched C^{13} samples. The spectra are a result of using CP/MAS with decoupling of the proton

The mechanism of action of the additional water facilitates significant chemical change of the acetonitrile and in turn leads to more production of the amide breakdown product located at approximately 168 ppm. This change can be seen in the above figure 7.8 spectra. As illustrated above the change is also significant not only for amide but also for the aminoacetylene peak at 145 ppm. Finally as previously mentioned the additional water promotes some of the glycolonitrile to further decompose to form formaldehyde. Again this is depicted in figure 7.8 by the reduction of the ^{13}C peak of glycolonitrile signal. The aforementioned changes are not seen in

the drier sample. It is important to note that in both the methyl enriched peak and the nitrile enriched peak, the acetamide production undergoes the most change.

7.4 Conclusion

The deliberately added 200 ppm of water does cause additional breakdown products. The water does enhance presence of at least two electrolyte solvent decomposition products, CH_3CONH_2 and $HOCH_2CN$, and in addition the glycolonitrile of the wetter sample goes through further decomposition. The changes from wet to dry in both the nitrile and methyl enriched ^{13}C are consistent with the acetonitrile being hydrolyzed. We can conclude this because the integrated areas of central peaks, in both groups of samples, are less in the wet than in dry. The methyl enriched group shows more acetamide is made in the wet sample, by hydrolysis, as compared to the dry. This would imply that the main breakdown pathway is that of acetonitrile to acetamide and the enriched carbon NMR signals are of the methyl carbon of acetamide and the carboxylic carbon of the amide.

[1] G.G Amatucci, F. Badway, A. Du Pasquier, and T. Zheng, *Journal of The Electrochemical Society*, (148), 2001

[2] J.S. Reed, Introduction to the principles of ceramic processing, p. 140 John Wiley & sons, Inc New York (1988)**]**

[3] G.G Amatucci, F. Badway, A. Du Pasquier, and T. Zheng, *Journal of The Electrochemical Society*, (148), 2001

[4] Advance Electrochemical Capacitor,*Technology and Applied R&D Needs for Electrical Energy Storage,* Department of Energy, 2007

[5] ”www.ornl.gov/sci/sp/Pres/Duong.ppt”

[6] Journal of The Electrochemical Society 150 (4) A484-A492 (2003)]

[7] J.P. Zheng, *Journal of The Electrochemical Society*, 148 (8), 2001

[8] A. Du Pasquier, I. Plitz, S. Menocal, and, G. Amatucci, *Journal of Power Sources*, (115) 2001

[9] M.S. Halper, and J.C. Ellenbogen, “www.mitre.org/tech/nanotech” , Mitre 2006

[10] A. Du Pasquier, A. Laforgue, P. Simon. G. Amatucci, and J.F. Fauvarque, Journal of The Electrochemical Society, (149) 2002

[11] Energy Storage Group, “http://www.argreenhouse.com/ESR/ah-main.html”, Telecordia Technologies, 2002

[12] M.J. Gidley, and J.K. Sanders*, Biochemical Journal*, 203, 1982

[13] U.S. Patent 20060247467A1

[14] D. Emeis, W Anker, and K.P. Wittern, *Analytical Chemistry*, 79 (5), 2007

[15] M.G. Laborie and C. E. Frazier, *Journal of Material Science*, 41, 2006

Appendix

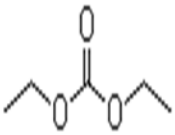

Figure 1. diethyl carbonate (DEC)

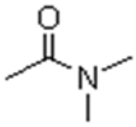

Figure 2. dimethylacetamide (DMAc)

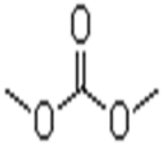

Figure 3. dimethyl carbonate (DMC)

Figure 4. ethylene carbonate (EC)

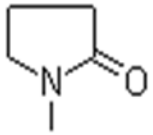

Figure 5. N-methyl pyrrolidone (NMP)

Figure 6. N-methyl pyrrolidone (NMP)

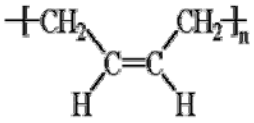

Figure 7. Polybutadiene (PB)

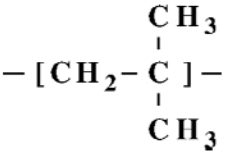

Figure 8. Polyisobutylene (PIB)

Bibliography

[1] Annual Energy Review 2007 “www.eia.doe.gov/aer/pdf/aer.pdf”

[2] Coalition for Affordable and Reliable Energy, Energy and America’s Economy, “www.careerenergy.com/energy/energy-americas-economy.asp,” 2003.

[3] Status of Electrical Energy Storage Systems “www.berr.gov.uk/files/file15189.pdf,” 2004.

[4] M. Wakihara, 0. Yamamoto, *Lithium Ion Batteries Fundamentals and Performance*, Wiley-VCH, 1998

[5] P. Poizot, S. Laruelle, S. Grugeon, L. Dupont, and J. M. Tarascon, Nature 407, 496 (2000)

[6] J. M. Tarascon and M. Armand, Nature 414, 359 (2001)

[7] C.Wanga, Z. X. Guob, S. Fua, W. Wub, and D. Zhub Progress in Polymer Science 29 (2004) 1079–1141

[8] M. L. Shofner, V. N. Khabashesku, and E.V. Barrera Chemical Material 2006, 18, 906-913

[9] I. Hadjipaschalis, A. Poullikkas and V. Efthimiou, Renewable and Sustainable Energy Reviews, 2008

[10] M. S. Halper and J. C. Ellenbogen, *Supercapacitors: A Brief Overview*, Mitre, 2006

[11] E. Frackowiak, and F. Beguin , Carbon 39(6) 2001

[12] J. Gamby, P. L. Taberna, et al., Journal of Power Sources 101(1), 2001

[13] D.Y. Qu, and H. Shi Journal of Power Sources 74(1), 1998

[14] K.H. An, W. S. Kim, et al., Advanced Materials 13(7) 2001

[15] K.H An, W. S. Kim, et al Advanced Functional Materials 11(5) 2001

[16] C.S. Du, J. Yeh, et al. Nanotechnology 16 (4) 2005

[17] P.V. Wright, Materials Research Societ Bulletin, (8), 2002

[18] C.P. Slichter, *Principles of Magnetic Resonance* 3ed. Springer-Verlag 1990

[19] M. Levitt, *Spin Dynamics: Basics of Nuclear Magnetic Resonance*, John Wiley & Sons, 2001

[20] D. J. Griffiths, *Introduction to Quantum Mechanics* 2ed. Benjamin Cummings, 2004

[21] O. Zerbe , NMR Spectroscopy Lecture Course, "http://www.oci.uzh.ch/group.pages/zerbe/" 2005

[22] G. Moyna, *Background Concepts*

"http://tonga.usip.edu/gmoyna/NMR_lectures/NMR_lectures.html"

[23] C. Kittel, *Introduction to Solid State Physics* 8ed., John Wiley & Sons, 2004

[24] J.W. Emsley, J. Feeney, *Progress in Nuclear Magnetic Resonance Spectroscopy* 50 (2007) 179.

[25] Eds. L. D. Field, S. Sternhell, *Analytical NMR*, 1ed., John Wiley & Sons, New York, 1989.

[26] U. Oehler, "http://www.chembio.uoguelph.ca/DrIguana/NMR/TOC.HTM", 2007

[27] Magnetic Resonance, "http://physchem.ox.ac.uk/~hill/tutorials/nm3_tutorial/nucspin/index.html" Oxford University, 2008

[28] A. Abragam *Principles of Nuclear Magnetism*, Oxford University Press 1999

[29] V.J. McBrierty and K.J. Packer, *Nuclear Magnetic Resonance in Solid Polymers*, Cambridge University Press, 1993

[30] J. L. G. Fierro *Spectroscopic Characterization of Heterogeneous Catalysts*, Elsevier Science Ltd, 1990

[31] I. Hung, A. Wong et al., Journal of Magnetic Resonance 188 2007

[32] R. Liboff, *Introductory Quantum Mechanics* 4ed., Addison Wesley, 2002

[33] S.K. Strauss, *NMR Interactionns*, "www.chem.ubc.ca/faculty/straus/c518_08.html" 2007

[34] A. Godec and U Maver, *Solid State NMR theory and pharmaceutical applications*, National Institute of Chemistry Solvenia, 2008

[35] R.W. Schurko, I. Hung, C. L. B. Macdonald, and A. H. Cowley, Journal of American . Chemical Society , 124 (44) , 2002

[36] Z. Fang, *Accomplishment of VACSY experimental set-up and Its Application to Investigate Molecular Orientation Distribution of Solid-State Polymers* "http://sundoc.bibliothek.uni-halle.de/diss-online/99/99H200/t3.pdf", 1999

[37] R. Schurko, *Introduction to Solid State NMR*, "http://mutuslab.cs.uwindsor.ca/schurko/ssnmr/ssnmr_schurko.pdf" 2007

[38] M. Levitt, *Spin Dynamics: Basics of Nuclear Magnetic Resonance*, John Wiley & Sons, 2001

[39] M.J. Duer, *Introduction to Solid-State NMR* , Wiley-Blackwell, 2005

[40] G. Gauglitz, and T. Vo-Dinh, *Handbook of Spectroscopy*, (2 Vol. Set), Wiley-VCH, 2003

[41] L.J. Mathias, *Solid State NMR of Polymers*, 1ed, Springer, 1991

[42] C.P. Slichter, *Principles of Magnetic Resonance* 3ed. Springer-Verlag 1990

[43]] R. Liboff, *Introductory Quantum Mechanics* 4ed., Addison Wesley, 2002

[44] S.K. Strauss, *NMR Interactionns*, "www.chem.ubc.ca/faculty/straus/c518_08.html"

[45] D. J. Griffiths, *Introduction to Quantum Mechanics* 2ed. Benjamin Cummings, 2004

[46] T.L. James, *Fundamentals of NMR*, Department of Pharmaceutical Chemistry University of California, 2008

[47] G. Moyna, *NMR lectures in Advanced Spectroscopy*, "http://tonga.usip.edu/gmoyna/NMR_lectures/NMR_lectures.html", 2008

[148] A. Godec and U Maver, *Solid State NMR theory and pharmaceutical applications*, National Institute of Chemistry Solvenia, 2008

[49] O. Zerbe , NMR Spectroscopy Lecture Course, "http://www.oci.uzh.ch/group.pages/zerbe/" 2005

[50] S. Strauss, Solid State NMR: Cross Polarization,

"http://www.chem.ubc.ca/faculty/straus/Nlecture17.pdf" 2007

[51] *Basic Cross Polarisation* "http://www.dur.ac.uk/resources/SSNMR/three5.pdf" Durham University, Solid-state NMR Service 2002

[52] S. Hafner and H.W. Spiess, Concepts in Magnetic Resonance, 10 (1), John Wiley & Sons, 1998

[53] B.M. Meyer, S.G. Greenbaum, and C.P. Grey, *Electrochemical and Solid-State Letters*, 8 (3) 2005

[56] Y. Wang, X. Guo, S.G. Greenbaum, J. Liu and K Amipe, Electrochemical and Solid-State Letters, 4 (6) 2001

[57] Y. Wang, S. Nakamura, K. Tasaki, and P.B. Balbuena, *Journal of American Chemical Society*, 124, 2002

[58] M.C. Smart, B.V Ratnakumar, X. Zhang, S.G. Greenbaum, C.C. Ahna, and B Futz, *Journal of The Electrochemical Society*, 146 (11), 1999

[59] G. Chen, G.V. Zhuang, T.J. Richardson, G. Liu and P.N. Ross Jr., *Electrochemical and Solid-State Letters*, 8 (7), 2005

[60] Y. Matsuda, T. Fukushima, H. Hashimoto, and R. R Arakawa, Journal of The Electrochemical Society, 149 (8), 2002

[61] S. Gautier, E. Frackowiak, J. Conard, J.N. Rouzaud, F Beguin, "http://acs.omnibooksonline.com/data/papers/1997_ii148.pdf" 1997

[62] J.R. Dahn, A.K. Sleigh, S. Hang, B.M Way, Q. Zhang, and U. von Sacken, *Elsevier*, Amsterdam, 1994

[63] C. Delmas, I Saadoune and A. Rougier, *Journal of Power Sources*, 43, 1993

[64] W. Li, and C. Curie, *Journal of The Electrochemical Society*, (144), 1997

[65] J. Cho, G. Kim, and H.S. Lim, Journal of The Electrochemical Society, (146), 1999

[66] M. Carewska, S. Scaccia, S. Arumugan, Y. Wang, and S. G. Greenbaum. Solid State Ionics, (93), 1997

[67] S. Castro-Gracia, and C. Julien, *Ionics*, (4), 1998

[68] D. Kim, J. Sohn, C. Lee, J. Lee, K. Han, and Y. Lee, Journal of Power Sources, (132), 2004

[69] R. Sott, J. Granander, and G. Hilmersson, Journal of The American Chemical Society, (125) 2004

[70] D. Carlier, M. Menetrier, C.P. Grey, C Delmas, and G. Ceder, Physical Review B, (67), 2003

[71] M.S. Ding and T.R. Jow Journal of The Electrochemical Society, (151), 2004

[72] H, Ora, Y. Sakata, A. Inoue and S. Yamaguchi, Journal of The Electrochemical Society, (151), 2004

[73] D. Carlier, M. Menetrier, and C. Delmas. *Journal of Materials Chemistry*, (11), 2001

[75] I. Saadoune, and C. Delmas, Journal of Solid State chemistry, (136) 1998

[76] I. Saadoune, M. menetrier, and C. Delmas, Journal of Material Chemistry, (7) 1997

[77] C. Julien, ans S.S. Michael, Ionics, (4), 1998

[78] P.J. Harris " Cabon Nanotubes and Related Structures" Cambridge University Press, 1999

[79] Q. Chen, R. Xu, and D. Yu, *Polymer*, 47, 2006

[80] S. Kumar, *Polymer/ Carbon Nanotube Composites: Challenges and Opportunities*, Georgia Institute of Technology, 2004

[81] S..J. Frankland, A. Caglar, and D.W. Brenner, *Reinforcing Polymers with Carbon Nanotubes*, Foresight Nanotech Institute

[82] L. Peng, *European Polymer Journal*, 2005

[83] P.M. Ajayan, L.S. Schadler, C Giannaris, A. Rubio, *Advanced Materials*, 12, 2000

[84] M. L. Shofner, V. N. Khabasheskau, and E. N. Barrera, *Chemical Material*, 18 2006

[85] M. J. Connell,P. J. Boul, L. M. Ericson, C. B. Huffman, Y. Wang, E. Haroz, C. Kuper, J. M. Tour, K. Ausman, and R. E. Smalley, *Chemical Physics Letters*. 2001

[86] J. Zhu, J.D. Kim, H. Peng, J.L.Margrave, V.N. Khabashesku, E.V.Barrera, *Nano Letters*, 3, 2003

[87] H.Geng, R. Rosen, B. Zheng, H. Shimoda, L.Fleming, J. Liu, O. Zhou, "*AdVance. Materials*.14, 2002

[88] M. L. Shofner, V. N. Khabasheskau, E.N. Barrera, *Chemical Material*, 18, 2006,

[89] G.G Amatucci, F. Badway, A. Du Pasquier, and T. Zheng, *Journal of The Electrochemical Society*, (148), 2001

[90] J.S. Reed, Introduction to the principles of ceramic processing, p. 140 John Wiley & sons, Inc New York (1988)**]**

[91] G.G Amatucci, F. Badway, A. Du Pasquier, and T. Zheng, *Journal of The Electrochemical Society*, (148), 2001

[92] Advance Electrochemical Capacitor,*Technology and Applied R&D Needs for Electrical*

Energy Storage, Department of Energy, 2007

[93] "www.ornl.gov/sci/sp/Pres/Duong.ppt"

[94] Journal of The Electrochemical Society 150 (4) A484-A492 (2003)]

[95] J.P. Zheng, *Journal of The Electrochemical Society*, 148 (8), 2001

[96] A. Du Pasquier, I. Plitz, S. Menocal, and, G. Amatucci, *Journal of Power Sources*, (115) 2001

[97] M.S. Halper, and J.C. Ellenbogen, "www.mitre.org/tech/nanotech" , Mitre 2006

[98] A. Du Pasquier, A. Laforgue, P. Simon. G. Amatucci, and J.F. Fauvarque, Journal of The Electrochemical Society, (149) 2002

[99] Energy Storage Group, "http://www.argreenhouse.com/ESR/ah-main.html", Telecordia Technologies, 2002

[100] M.J. Gidley, and J.K. Sanders*, Biochemical Journal*, 203, 1982

[101] U.S. Patent 20060247467A1

[102] D. Emeis, W Anker, and K.P. Wittern, *Analytical Chemistry*, 79 (5), 2007

[103] M.G. Laborie and C. E. Frazier, *Journal of Material Science*, 41, 2006